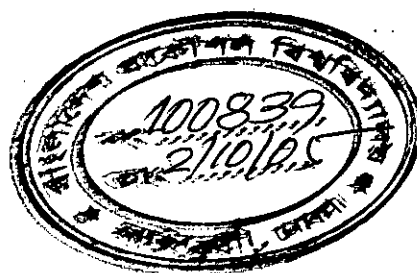
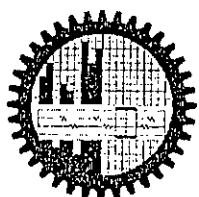
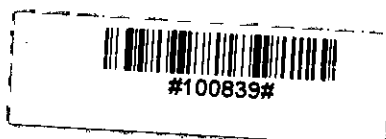


FLOW FIELD BEHIND A FINITE-THICKNESS BASE IN TWO
NON-PARALLEL STREAMS



By
T. M. SHAIFUL ISLAM



DEPARTMENT OF MECHANICAL ENGINEERING
BANGLADESH UNIVERSITY OF ENGINEERING
AND TECHNOLOGY, DHAKA, BANGLADESH .

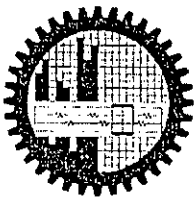
APRIL 2005

FLOW FIELD BEHIND A FINITE-THICKNESS BASE IN TWO
NON-PARALLEL STREAMS

BY
T. M. SHAIFUL ISLAM

A Thesis

Submitted to the Department of Mechanical Engineering in partial
fulfillment of the requirements
for
the degree of Master of Engineering in Mechanical Engineering.

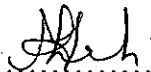


DEPARTMENT OF MECHANICAL ENGINEERING
BANGLADESH UNIVERSITY OF ENGINEERING
AND TECHNOLOGY, DHAKA, BANGLADESH
APRIL 2005

RECOMMENDATION OF THE BOARD OF EXAMINERS

The board of examiners hereby recommends to the Department of Mechanical Engineering, BUET, Dhaka, the acceptance of this thesis, "FLOW FIELD BEHIND A FINITE-THICKNESS BASE IN TWO NON-PARALLEL STREAMS", submitted by T. M. Shaiful Islam, in partial fulfillment of the requirements for the degree of Master of Engineering in Mechanical Engineering.

Chairman (supervisor):



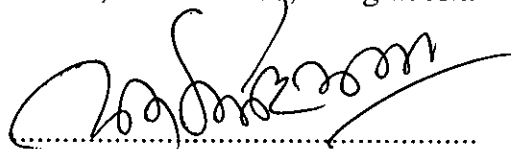
.....
Dr. Mohammad Ali
Associate professor
Department of Mechanical Engineering
BUET, Dhaka-1000, Bangladesh.

Member (Ex-officio):



.....
Dr. Md. Quamrul Islam
Professor & Head
Department of Mechanical Engineering
BUET, Dhaka-1000, Bangladesh.

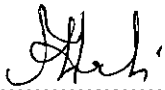
Member :



.....
Dr. A. K. M. Sadrul Islam
Professor
Department of Mechanical Engineering
BUET, Dhaka-1000, Bangladesh

CERTIFICATE OF RESEARCH

This is to certify that the work presented in this dissertation is the outcome of the investigation carried out by the author under the supervision of Dr. Mohammad Ali, Associate professor, Department of Mechanical Engineering, Bangladesh University of Engineering and Technology (BUET), Dhaka, Bangladesh and that it has not been submitted anywhere for the award of any degree or diploma.



.....
Dr. Mohammad Ali
Supervisor



.....
T. M. Shaiful Islam
Author

ACKNOWLEDGEMENT

At First, author wishes to express his deepest gratefulness and infinite thanks to the almighty “Allah” for the successful completion of project and thesis work. The author express his indebtedness and heartiest gratitude and rejoicingly express heartiest acclamation to his thesis supervisor Mohammad Ali, Associate professor, Department of Mechanical Engineering, Bangladesh University of Engineering and Technology, (BUET), Dhaka, for his cardiac guidance, patiently care and attention, help and encouragement, valuable suggestions which enable his to overcame the various problems related to this project work.

The author also expresses his gratitude to Dr. Md. Quamrul Islam, Professor and Head of the Department of Mechanical Engineering (BUET), Dhaka, Bangladesh for his valuable suggestion.

The author is very much grateful to honorable Dr. A. K. M. Sadrul Islam, Professor of the Department of Mechanical Engineering (BUET), Dhaka, Bangladesh for his valuable suggestion and kind help.

The author also extend his thanks and gratitude to teachers of Mechanical Engineering Department, Who cooperate by giving permission to use the computers of teacher’s Computer room.

Authors gratefully remember his beloved parents, friends and well wishers.

Finally, the author offers his sincere thanks to all those who help him either directly or indirectly in various stages to computer his thesis.

ABSTRACT

A numerical study on mixing and characteristic phenomena of subsonic hydrogen flow with a supersonic airflow behind a finite-thickness base has been performed by solving Two-Dimensional Navier-Stokes equations. An explicit Harten-Yee Non-MUSCL Modified-Flux-Type TVD (Total Variational Diminishing) scheme has been used to solve the system of equations, and a zero-equation algebraic turbulence model proposed by Baldwin and Lomax has been used to calculate the eddy viscosity coefficient. To delineate the purely fluid dynamic effects, the flow has been treated as non-reacting.

The objectives of this research are to observe the mixing of hydrogen with air, characteristic phenomena of the flowfield, mixing efficiency and flame holding capability of a supersonic combustor. Two non-parallel streams are considered for this study. The merging angle and base thickness between air and hydrogen streams are taken as variable parameters. The merging angles are varied as 10° , 20° , 30° , 40° and 50° for base thickness 0.01 m and base thickness is increased to 0.015 m for merging angles 10° , 20° and 40° to study the physics of the flowfield. Two large recirculations behind the base can be found which can enhance mixing. With the increase of merging angle, the recirculation region decreases but mixing efficiency increases up to 40° merging angle. On the other hand the flame holding capability has been better for small merging angle (10°) due to the relatively large and elongated recirculation, which is an important factor for flame holding capability. Secondly, the base thickness is 0.015 m and then merging angle are 10° , 20° and 40° . For higher base height, the recirculation regions become large and elongated. The mixing efficiency is higher than that of 0.01 m base thickness. Higher base thickness enhances both the mixing efficiency and flame holding capability. The recirculation regions and several shocks such as expansion shock, recompression shock and reattachment shock in the flowfield are evident.

CONTENTS

	<u>Page</u>
Title	I
Certificate of Approval	II
Certificate of Research	III
Acknowledgement	IV
Abstract	V
Contents	VI
List of Figures	VIII
List of Tables	IX
Nomenclature	X

CHAPTER-I

INTRODUCTION

1.1 General	1
1.2 Background	2
1.3 Objective	6

CHAPTER-II

MATHEMATICAL MODEL

2.1 Governing Equations	7
2.2 Calculation of Temperature	11
2.3 Transport Coefficients	12
2.4 Numerical Scheme	14
2.5 Boundary Conditions and Convergence Criterion	17
2.6 Use of Turbulence Model	17

CHAPTER-III

RESULTS AND DISCUSSION

3.1 Introduction	21
3.2 Flow Field Description and Numerical Parameter	21
3.3 Effect of Merging Angle	22
3.4 Effect of Base Thickness	30

CHAPTER-IV

CONCLUSION

4.1 Summary of the Study	36
4.2 Recommendation for Future Study	37

BIBLIOGRAPHY	38
---------------------	-----------

LIST OF FIGURES

	<u>Page</u>
Fig. 3.1 (a) Schematic of the physical model	41
Fig. 3.1 (b) Flowfield characteristics of the physical model	41
Fig. 3.1 (c) Grid System of the Calculation domain	42
Fig. 3.2 (a) Velocity vector (case-1)	42
Fig. 3.2 (b~c) Velocity vector (case-2 & 3)	43
Fig. 3.2 (d~e) Velocity vector (case-4 & 5)	44
Fig. 3.3 (a~b) Velocity profiles at 0.005 & 0.015 m (cases 1~5)	45
Fig. 3.3 (c~d) Velocity profiles at 0.03 & 0.05 m (cases 1~5)	46
Fig. 3.4 (a) Lengthwise velocity profiles (case-1 & 4)	47
Fig. 3.4 (b) Transverse velocity profiles (case-1 & 4)	47
Fig. 3.5 (a~b) Mole fraction contour (case-1 & 2)	48
Fig. 3.5 (c~d) Mole fraction contour (case-3 & 4)	49
Fig. 3.5 (e) Mole fraction contour (case-5)	50
Fig. 3.6 (a) Mixing efficiency (cases 1~5)	50
Fig. 3.6 (b) Mixing efficiency vs. merging angle (cases 1~5)	51
Fig. 3.7 (a) pressure (Pa) contour (case-1)	51
Fig. 3.7 (b~c) pressure (Pa) contour (case-2 & 3)	52
Fig. 3.7 (d~e) pressure (Pa) contour (case-4 & 5)	53
Fig. 3.8 (a~b) Pressure distribution at 0.005 & 0.015 m (cases 1~5)	54
Fig. 3.8 (c~d) Pressure distribution at 0.03 & 0.05 m (cases 1~5)	55
Fig. 3.9 centerline pressure profiles (cases 1~5)	56
Fig. 3.10 (a) Temperature (K) contour (case-1)	56
Fig. 3.10 (b~c) Temperature (K) contour (case-2 & 3)	57
Fig. 3.10 (d~e) Temperature (K) contour (case-4 & 5)	58
Fig. 3.11 (a~b) Velocity vector (case-6 & 7)	59
Fig. 3.11 (c) Velocity vector (case-8)	60
Fig. 3.12 (a) Velocity profiles at 0.005 m (cases 6~8)	60

Fig. 3.12 (b~c) Velocity profiles at 0.019 m & 0.03 m (cases 6~8)	61
Fig. 3.12 (d) Velocity distribution at 0.05 m (case 6~8)	62
Fig. 3.13 (a) Lengthwise velocity profiles (case-6& 8)	62
Fig. 3.13 (b) Transverse velocity profiles (case-6& 8)	63
Fig. 3.14 (a) Mole fraction contour (case-6)	63
Fig. 3.14 (b~c) Mole fraction contour (case-7 & 8)	64
Fig. 3.15 (a) Mixing efficiency (cases 6~8)	65
Fig. 3.15 (b) Mixing efficiency vs. merging angle (cases 6~8)	65
Fig. 3.15 (c) Comparison of mixing efficiency	66
Fig. 3.16 (a) pressure (Pa) contour (case-6)	66
Fig. 3.16 (b~c) pressure (Pa) contour (case-7 & 8)	67
Fig. 3.17 (a~b) Pressure distribution at 0.005 & 0.019 m (cases 6~8)	68
Fig. 3.17 (c~d) Pressure distribution at 0.03 & 0.05 m (cases 6~8)	69
Fig. 3.18 centerline pressure profiles (cases 6~8)	70
Fig. 3.19 (a) Temperature (K) contour (case-6)	70
Fig. 3.19 (b~c) Temperature (K) contour (case-7 & 8)	71

LIST OF TABLES

Table 2.1 Coefficients of Thermodynamic Polynomials	72
Table 2.2 Constants used in Transport Equations	72
Table 3.1 Calculation Summaries	73

NOMENCLATURE

<u>Symbol</u>	<u>Meaning</u>	<u>Unit</u>
h	finite-thickness base width	m
b	inlet height of the streams	m
C	molar concentration	Mole/m ³
c	sound speed	m/s
C_p	specific heat at constant pressure	J/(kg. K)
D_{iml}	molecular diffusion coefficient of i -th species	m ² /s
D_{it}	turbulent diffusion coefficient of i -th species	m ² /s
D_{ij}	binary-diffusion coefficient for species i and j	m ² /s
E	total energy	J/m ³
F	flux vector in x -direction	
\hat{F}	transformed flux vector in ξ -direction	
f_H	Local mass fraction of hydrogen	
G	flux vector in y -direction	
\hat{G}	transformed flux vector in η -direction	
h	enthalpy	J/kg
J	transformation Jacobian	
J	number of grid points in x -direction	
JJ	maximum number of grid points in x -direction	
K	number of grid points in y -direction	
KK	maximum number of grid points in y -direction	
M	Mach number	
\dot{m}	mass flux of species	kg/s
p	pressure	Pa
q_c	energy flux by conduction	W/m ²
q_D	energy flux by diffusion	W/m ²
R	universal gas constant	J/(kg.mol.K)
S	Sutherland constant for viscosity	K

S'	Sutherland constant for thermal conductivity	K
T	temperature	K
T_e	effective temperature	K
t	physical time	second
u	horizontal velocity	m/s
u_e	Velocity at the edge of boundary layer	m/s
U	vector of conservative variables	
\hat{U}	transformed vector of conservative variables	
U	contravariant velocity in ξ -direction	
V	vertical velocity	m/s
V	contravariant velocity in η -direction	
W	molecular weight of species	gm/mol
x	horizontal Cartesian coordinate	m
Y	mass fraction of species	
y	vertical Cartesian coordinate	m
Z	mole fraction of species	
α	merging angle	degree
ξ	transformed coordinate in horizontal direction	
η	transformed coordinate in vertical direction	
ρ	mass density	kg/m ³
σ	normal stress	Pa
τ	shear stress	Pa
μ	coefficient of dynamic viscosity	kg/(m.s)
κ	thermal conductivity	W/(m.K)
δ	boundary layer thickness	m
δ^*	Kinematics displacement thickness	m
ϕ'	local equivalence ratio of hydrogen and oxygen	
Φ	global equivalence ratio of hydrogen and oxygen	
φ	contour level	

Superscripts

ns number of species

Subscripts

i, j index for species

l laminar case

m mixture

t index for turbulence

v viscosity term

x horizontal direction

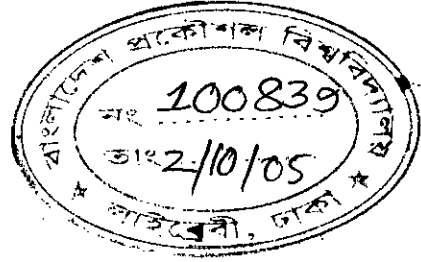
y vertical direction

xy reference plane

0 reference value, stagnation condition

CHAPTER-I

INTRODUCTION



1.1 General

Mixing process plays a vital role in the operation of combustor in many engineering application e.g. combustion chambers, pre-mixers for gas turbine combustors, chemical lasers, propulsion systems and flow reactors. In the supersonic combustion system, the flow speeds are so high that the fuel and oxidizer have very little time to mix i.e. high penetration and mixing of injectant with main stream is difficult due to their short residence time in combustor. The developing shear layer generated by turbulent mixing of two coflowing fluid streams has been one of the most active areas of research in fluid mechanics. In recent development of efficient supersonic combustion ramjet (scramjet) engines and advanced airspace propulsion system, there is renewed interest in the study of turbulent mixing layer. The turbulent mixing layer, which forms at the interface between two uniform streams of different velocity, develops through two successively distinct regions, namely the near-field regions. Unfortunately, the growth rate of mixing layer in two supersonic streams is considerably smaller than that of two subsonic streams. Brown [1] showed that the spreading rate of supersonic mixing layer decreased dramatically with increasing of free stream Mach number. Though a considerable number of researches have been carried out on mixing and combustion of fuel with supersonic air stream, still it faces many unsolved problems. The main problems that arise in this regard concern mixing of reactants, ignition, flame holding and completion of combustion. To overcome these problems many efforts have been expended for past three decades.

There exist several methods of injection in the supersonic air stream. Perpendicular injection causes rapid fuel-air mixing and used to some degree of

all flight Mach numbers to promote mixing. On the other hand, parallel injection is used when slow process is desired, especially at lower speed of space vehicles. When operating a lower Mach number, parallel injection must be used extensively to slow the mixing process and prevent thermal choking. In parallel or non-parallel (if small injection angle) injection or inlet streams, very weak interaction occurs between two flows. Weak interaction means weak penetration as well as low mixing. The mixing layers from non-parallel merging streams were found to have higher growth in the near field than those from parallel merging streams [2]. In this time, recirculation region and mixing region can enhance mixing. If the recirculation is large, elongated and good, the mixing is improved. Then the flame holding capability is also better, which is very important in combustor.

Hydrogen is well known as the most suitable fuel for such propulsion systems because of its high potential of heat release and rapid mixing with air. Because of the high speed of the airstream, a reasonable length is needed for the combustor. So it is difficult to perform the experimental study under the supersonic combustion because of high cost. Therefore, the numerical research is quite important. In this research, it is numerically simulated two-dimensional mixing flowfield with non-parallel two streams. The effect of merging angle of two streams and the effect of base thickness between two streams have been studied to observe the flow field characteristics phenomena and mixing of air-hydrogen.

1.2 Background

Many studies, such as theoretical and numerical have been performed to analyze the mixing, combustion characteristics and mixing efficiency in supersonic or subsonic flows. Azim et al. [2] showed that the mixing layers decreased in growth with increasing velocity ratio, though the streams spreaded more at the high-speed side. With increasing velocity ratio the development distance was increasing and splitter wake played a dominant role in the development of the

mixing layers. The mixing layers from non-parallel merging streams (18°) were found to have higher growth in the near field than those from parallel merging streams. In an experimental investigation of the complex interaction region behind a finite thickness base Amatucci et al. [3] showed the mixing process in recirculating and shear-layer region, and characteristic of the flowfield. They showed that strong mixing and diffusion occurred in the recirculation region due to strong interactions with the low velocity regions of both shear layers and due to low pressure behind the base. The shear-layer mixing region spreaded with streamwise distance. The turbulent mixing also occurred at far downstream region. To compare the numerical results with previous experimental results for non-reacting wake flow behind the base Tabejamaat et al. [4] showed that the recirculation was very important for mixing. That numerical result predicted expansion at the separation points, formation of a recirculation region bounded by two shear layer mixing regions, recompression and reattachment of the shear layers and downstream wake redevelopment. In a numerical study on backward facing geometric configuration, Ahmed [5] found that the upstream recirculation played an important role to enhance mixing. He showed that the configuration for small distance of injection position had high mixing efficiency but the flame holding capability was not good. By varying injection angle and Mach number, the investigation showed that perpendicular injection and higher mach number ($M=1.3$) increased both mixing efficiency and flame holding capability. In a transverse injection in a supersonic air stream Ali [6] showed the pattern of upstream recirculating region with changing the step height. He showed that the upstream recirculation was larger and elongated for high step height. But either mixing or flame holding capability is not good for the high step height. The elongated upstream recirculation in configuration $h/b=5$ provided longer residence of flow with good proportion of fuel and oxidizer. Berman et al [7] reported the computation results for the supersonic flow over a rearward-facing step with transverse injection. They showed that the recirculating region formed behind the step and that recirculating region was fuel rich due to the combined effects of convection and mass diffusion. The pressure in recirculating region

was nearly constant. For the flow through a plane duct with a symmetric sudden expansion Durst et al. [8] studied the separation and recirculation regions in various Reynolds number, Re . (from 70 to 610). They observed that for Re . above 400, a third separation region appeared on the short separated sidewall, growing in length with increasing Re . They also observed the detachment and reattachment points as function of Re . Fearn et al. [9] and Alleborn et al. [10] also studied the recirculation, separation and reattachment points on the two-dimensional flow in a sudden expansion.

In a study on turbulent mixing layers, Brown et al. [1] showed that the spreading rate of supersonic mixing layer decreased drastically with increasing of free stream Mach number. They also concluded that the strong effects on mixing-layer spreading rate were due to compressibility effects, not density effects. Umeda et al. [11] performed a numerical analysis of two flows moving from a periodic boundary to the opposite direction. They showed that the upper right-going layer and the lower left-going layer interacted and mixed due to vertical entrainment and molecular diffusion. Takahashi et al. [12] found that the use of the turbulence model improved the interpretation of the experimental data, but showed the insufficient effects of turbulence model at the separation regions and near the injector because of a complex flow. They also suggested that a two-equation model was necessary to improve the simulation. Yokota et al. [13] numerically investigated the effects of injection method on supersonic mixing. They showed that the area of the mixing region was very important for the mixing enhancement. For parallel injection, when the distance from the wall to the injection slit was not zero, mixing efficiency was twice as larger as than ones in other injection methods. Two streamwise injections with swept ramps were studied by Lee [14] to enhance fuel-air mixing. They showed that the streamwise vorticity generated by the swept ramp caused the injected fuel stream to be lifted from the floor and roll into itself, developing a butterfly-like shape. That led to rapid mixing of the injected air with the freestream air. They also observed some flowfield features included separation and shock wave interaction effects.

A numerically simulation of mixing has been performed by Gerlinger et al. [15]. In parallel slot injection, they found that at the corner of the wall step an expansion fan was formed that was followed by a shock wave and the supersonic mixing was dominated by turbulent diffusion. To study the effect of the parameters on the twinjets, Moustafa [16] showed that the maximum velocity or total pressure decreased and the jet width increased with the increase of streamwise distance from the nozzle exit. For lower value of the nozzle spacing, the two jets mixed and combined to form like a single jet. In the case of higher nozzle spacing, the bending of the jet axis is larger than that of the smaller spacing. A numerical experiment of turbulent free mixing layer consisting of two coflowing fluid stream has been performed by Liou et al. [17]. They found that the vortex roll-up in the shear layer appeared to be delayed and the shear-scale structures were more flattered, elongated, and less mixed as convective Mach number (M_c) gone up. For the case of supersonic/subsonic velocity regimes, a lower development of the shear layers was observed with increasing M_c . To examine the streamwise pressure gradient effect on the mixing layer at the interface between the parallel supersonic flow, Abe et al. [18] showed that the mixing layer grown along the flow direction. They also showed that the growth rate of the mixing layer was enhanced when a streamwise pressure gradient existed.

In detailed study, several parameters were adopted to study the mixing of hydrogen with air. Recirculation, which formed behind the base or backward/rearward facing steps, had an important role to enhance mixing. Larger and elongated recirculation was important for good flame holding capability. The flows expanded sharply around the corner of geometric configuration and some cases caused a strong interaction. But interaction of air and hydrogen flows was weak in parallel streams or long distance injection. The mixing shear layer spreaded downstream. Throughout the mixing shear layer, mixing was occurred by diffusion due to density gradient at the interface of two flows. Mixing decreased with the increase of Mach number.

1.3 Objectives

The primary objective of this numerical study of air and hydrogen streams is to investigate the physics of fluid dynamic existing in the near-wake flowfield behind the base and how they interact, and mixing. Near-wake flowfield has been studied in order to investigate such features as change of velocity profiles due to the corner expansion process, strength and mixing in recirculation region, and shear layer regions. In this research, attention has been made on flowfield characteristic and mixing efficiency by using air and hydrogen flow inlet parameters as (i) merging angle of two streams and (ii) height of base thickness. Many researchers paid their attention to the injection methods on mixing of parallel supersonic air stream in different velocity and on geometric configuration to get better mixing. But there is no available information about the effect of air-hydrogen non-parallel streams behind a base, which I have done here. To delineate the purely fluid dynamic effects and mixing efficiency, the flow is treated as non-reacting because most of investigations on mixing of supersonic air stream with hydrogen have been conducted for mixing in non-reacting flowfield.

CHAPTER-II

MATHEMATICAL MODEL

2.1 Governing Equations:

The flowfield is to be analyzed governed by the unsteady, Two-Dimensional Navier-Stokes equations neglecting body forces and heat source terms, along with species continuity equations and an energy equation.

With the conservation-law form, the governing equations can be expressed by

$$\frac{\partial U}{\partial t} + \frac{\partial F}{\partial x} + \frac{\partial G}{\partial y} = \frac{\partial F_v}{\partial x} + \frac{\partial G_v}{\partial y} \quad (2.1)$$

Where

$$U = \begin{pmatrix} \rho \\ \rho u \\ \rho v \\ E \\ \rho Y_i \end{pmatrix}, \quad F = \begin{pmatrix} \rho u \\ \rho u^2 + p \\ \rho uv \\ (E + p)u \\ \rho Y_i u \end{pmatrix}, \quad G = \begin{pmatrix} \rho v \\ \rho uv \\ \rho v^2 + p \\ (E + p)v \\ \rho Y_i v \end{pmatrix}$$

$$F_v = \begin{pmatrix} 0 \\ \sigma_x \\ \tau_{xy} \\ \sigma_x u + \tau_{xy} v - q_x \\ -m_x \end{pmatrix}, \quad G_v = \begin{pmatrix} 0 \\ \tau_{yx} \\ \sigma_y \\ \tau_{yx} u + \sigma_y v - q_y \\ -m_y \end{pmatrix}$$

$$\begin{aligned}
\rho &= \sum_{i=1}^{ns} \rho_i R_i T \\
&= \sum_{i=1}^{ns} \rho_i \frac{R}{W_i} T
\end{aligned} \tag{2.2}$$

$$\begin{aligned}
E &= \sum_{i=1}^{ns} \rho_i h_i - \sum_{i=1}^{ns} \rho_i \frac{R}{W_i} T + \frac{\rho}{2} (u^2 + v^2) \\
&= \sum_{i=1}^{ns} \rho_i C_{pi} T - \sum_{i=1}^{ns} \rho_i \frac{R}{W_i} T + \frac{\rho}{2} (u^2 + v^2)
\end{aligned} \tag{2.3}$$

$$\begin{aligned}
\sigma_x &= \lambda \left(\frac{\partial u}{\partial x} + \frac{\partial v}{\partial y} \right) + 2\mu \left(\frac{\partial u}{\partial x} \right) \\
\sigma_y &= \lambda \left(\frac{\partial u}{\partial x} + \frac{\partial v}{\partial y} \right) + 2\mu \left(\frac{\partial v}{\partial y} \right) \\
\tau_{xy} = \tau_{yx} &= \mu \left(\frac{\partial u}{\partial y} + \frac{\partial v}{\partial x} \right)
\end{aligned} \tag{2.4}$$

$$\lambda = \frac{2}{3} \mu$$

Mass diffusion occurs whenever there exists a gradient in the proportions of the mixture, i.e. a concentration gradient. Because of this gradient, there is a mass motion species i in the opposite direction. If the velocity of this mass motion is U_i , called the diffusion velocity, the mass flux of species i is $\rho_i U_i$. This mass flux is given approximately by Fick's [19] law as

$$m = \rho_i U_i = -\rho D_{iml} \nabla Y_i \tag{2.5}$$

Where ρ is the mixture density and D_{iml} is the molecular diffusion coefficient of species i for diffusion into the mixture. The density of the mixture is determined from

$$\rho = \sum_{i=1}^{ns} \rho_i \tag{2.6}$$

Due to heat conduction, the flux of energy

$$q_c = -k\nabla T \quad (2.7)$$

And due to diffusion, energy flux of all species

$$q_D = \sum_{i=1}^{ns} \rho_i U_i h_i \quad (2.8)$$

Therefore, the total energy flux (radiation is neglected)

$$q = -k\nabla T + \sum_{i=1}^{ns} \rho_i U_i h_i \quad (2.9)$$

Considering the flowfield with gradients of temperature and mass fractions in x - and y -directions, the total energy flux in x -direction can be obtained by Eq. (2.9) as

$$q_x = -k \frac{\partial T}{\partial x} + \sum_{i=1}^{ns} \rho_i U_{ix} h_i \quad (2.10)$$

Where U_{ix} is the component of diffusion velocity of species i in x -direction. From Eq. (2.5), we can write

$$\rho_i U_{ix} = -\rho D_{iml} \frac{\partial Y_i}{\partial x} \quad (2.11)$$

Combining Eq. (2.10) and Eq. (2.11), we get

$$q_x = -k \frac{\partial T}{\partial x} - \sum_{i=1}^{ns} D_{iml} h_i \frac{\partial Y_i}{\partial x} \quad (2.12)$$

Similarly, the total energy flux in y -direction

$$q_y = -k \frac{\partial T}{\partial y} - \sum_{i=1}^{ns} D_{iml} h_i \frac{\partial Y_i}{\partial y} \quad (2.13)$$

Moreover, from Eq. (2.5), we can write the mass flux of species i in x -direction caused by diffusion as

$$m_x = -\rho D_{iml} \frac{\partial Y_i}{\partial x} \quad (2.14)$$

and in y -direction

$$m_y = -\rho D_{iml} \frac{\partial Y_i}{\partial y} \quad (2.15)$$

The specific heat and enthalpy of the mixture are determined from the following expressions.

$$C_p = \sum_{i=1}^{ns} Y_i C_{pi} \quad (2.16)$$

$$C = \sum_{i=1}^{ns} Y_i h_i \quad (2.17)$$

Where C_{pi} and h_i are the specific heat and enthalpy of the i -th species.

The value of C_{pi} and h_i are considered as functions of temperature and determined from the polynomial curve fitting developed by Moss [20]. They are as follows:

$$\frac{C_{pi}}{R_i} = a_{1i} + a_{2i}T + a_{3i}T^2 + a_{4i}T^3 + a_{5i}T^4 \quad (2.18)$$

$$\frac{h_i}{R_i T} = a_{1i} + \frac{a_{2i}T}{2} + \frac{a_{3i}T^2}{3} + \frac{a_{4i}T^3}{4} + \frac{a_{5i}T^4}{5} + \frac{a_{6i}}{T} \quad (2.19)$$

Where a_{1i} , a_{2i} , a_{3i} , a_{4i} , a_{5i} & a_{6i} are constants for different species. The coefficients for these curve fits are found in Table 2.1. Two sets of coefficients are available in Table 2.1 of which one for temperature range 0~1000K, the other set for 1000~5000K.

2.2 Calculation of Temperature

Temperature at various grid points is calculated by Newton-Raphson method. By rearranging Eq. (2.3), a relation for temperature can be expressed as

$$F(T) = \sum_{i=1}^{ns} \rho_i h_i - \sum_{i=1}^{ns} \rho_i \frac{R}{W_i} T + \frac{\rho}{2} (u^2 + v^2) - E \quad (2.20)$$

Substituting the value of h_i from Eq. (2.19), Eq. (2.20) can be written as

$$F(T) = b_0 + b_1 T + b_2 T^2 + b_3 T^3 + b_4 T^4 + b_5 T^5 \quad (2.21)$$

Where the coefficients are

$$\begin{aligned} b_0 &= \sum_{i=1}^{ns} \rho_i R_i a_{\delta i} + \frac{\rho}{2} (u^2 + v^2) - E, & b_1 &= \sum_{i=1}^{ns} \rho_i R_i a_{1i} - \sum_{i=1}^{ns} \rho_i R_i \\ b_2 &= \frac{1}{2} \sum_{i=1}^{ns} \rho_i R_i a_{2i} & b_3 &= \frac{1}{3} \sum_{i=1}^{ns} \rho_i R_i a_{3i} \\ b_4 &= \frac{1}{4} \sum_{i=1}^{ns} \rho_i R_i a_{4i} & b_5 &= \frac{1}{5} \sum_{i=1}^{ns} \rho_i R_i a_{5i} \end{aligned} \quad (2.22)$$

Differentiating Eq. (2.20) with respect to T, we get

$$F'(T) = b_1 + 2b_2 T + 3b_3 T^2 + 4b_4 T^3 + 5b_5 T^4 \quad (2.23)$$

Then the temperature is calculated by the following equation:

$$T_{new} = T_{old} - \frac{F(T_{old})}{F'(T_{old})} \quad (2.24)$$

The calculation of Eq. (2.24) is repeated until it fulfils the criterion for the temperature T_{new} . The criterion for this calculation is $|(T_{new} - T_{old})| < 1.0$.

2.3 Transport Coefficients

Molecular Viscosity Calculation

The molecular viscosity coefficient, μ_i is calculated using Sutherland's law [21] as

$$\frac{\mu_i}{\mu_0} = \left(\frac{T}{T_0} \right)^{1.5} \frac{T_0 + S}{T + S} \quad (2.25)$$

This formula is applicable for single component gas only. For the cases of interest in which hydrogen and air are present, Wilke's formulation [22] was used to calculate the mixture viscosities.

The molecular viscosity of multi-component gases mixture evaluated by the Wilke's law as

$$\mu_l = \frac{\sum_{i=1}^{ns} Z_i \mu_i}{\sum_{j=1}^{ns} Z_j \phi_{ij}} \quad (2.26)$$

Where $\phi_{ij} = \frac{[1.0 + (\mu_i / \mu_j)^{0.5} (W_j / W_i)^{0.25}]^2}{(8 + 8 W_i / W_j)^{0.5}}$, Z_i and Z_j are the mole fractions of i -th

and j -th species, respectively. S is the Sutherland constant, while μ_0 , and T_0 are the reference values taking from reference [5], are also tabulated in Table 2.2.

Molecular Thermal Conductivity

The molecular thermal conductivity κ_i is calculated using Sutherland's law as

$$\frac{\kappa_i}{\kappa_0} = \left(\frac{T}{T_0} \right)^{1.5} \frac{T_0 + S}{T + S} \quad (2.27)$$

When multi-component gases are present, Wassiljewa's equation for the thermal conductivity is used as

$$K_I = \sum_{i=1}^{nS} \frac{K_i}{1 + \frac{1}{Z_i} \sum_{\substack{j=1 \\ j \neq i}}^{nS-1} A_{ij} Z_j} \quad (2.28)$$

Where $A_{ij} = 1.065 \phi_{ij}$, Z_i and Z_j are the mole fractions, while K_0 is the reference value tabulated in Table 2.2. This formula differs from Wilke's formula for mixture viscosities only a constant.

Molecular Diffusion

Diffusion is treated by means of Fick's law [19]

$$\rho_i U_i = -\rho D_{iml} \nabla Y_i \quad (2.29)$$

The molecular binary-diffusion coefficient for each species, D_{ij} is determined from the empirical formula given by Chapman-Cowling [21] as

$$D_{ij} = \frac{0.001858 T^{1.5} \left(\frac{W_i + W_j}{W_i W_j} \right)^{0.5} \times 10^{-4}}{p \sigma_{ij}^2 \Omega_D} \quad (2.30)$$

Where

$$\Omega_D = \left(\frac{T}{T_{\epsilon i}} \right)^{-0.145} + \left(\frac{T}{T_{\epsilon j}} + 0.5 \right)^{-2.0} \quad (2.31)$$

$$T_{\epsilon ij} = (T_{\epsilon i} T_{\epsilon j})^{0.5} \quad (2.32)$$

$$\sigma_{ij} = \frac{1}{2} (\sigma_i + \sigma_j) \quad (2.33)$$

T = absolute temperature (K)

$T_{\epsilon i}, T_{\epsilon j}$ = the effective temperatures of each species respectively

p = pressure (atm)

Value of the effective temperature T_{ei} and effective collision diameter; σ_i of i -th species are taken from references [23], and [24] are also tabulated in Table 2.2.

Using the value of binary diffusion coefficient, the effective molecular diffusion coefficient for each species is determined by the following formula [23]

$$D_{int} = \frac{1 - Z_i}{\sum_{\substack{j=1 \\ j \neq i}}^{ns-1} Z_j / D_{ij}} \quad (3.34)$$

3.4 Numerical Scheme

The system of governing equation is solved, using an explicit Harten-Yee Non-MUSCL Modified-flux-type TVD (Total Variational Diminishing) scheme [25]. The scheme is second order accurate in time and space. Sutherland formula, Wilke's formula, Chapman-Cowling formula are used to calculate the transport coefficients. The Two-Dimensional, rectangular physical coordinate system (x, y) is transformed into the computational coordinate system (ξ, η) in order to solve the problem on uniform grids. After applying the transformation, Eq. (2.1) can be expressed as:

$$\frac{\partial \hat{U}}{\partial t} + \frac{\partial \hat{F}}{\partial \xi} + \frac{\partial \hat{G}}{\partial \eta} = \frac{\partial \hat{F}_v}{\partial \xi} + \frac{\partial \hat{G}_v}{\partial \eta} \quad (2.35)$$

Where

$$\begin{aligned} \hat{U} &= J^{-1}U, \quad \hat{F} = J^{-1}(\xi_x F + \xi_y G), \quad \hat{G} = J^{-1}(\eta_x F + \eta_y G) \\ \hat{F}_v &= J^{-1}(\xi_x F_v + \xi_y G_v), \quad \hat{G}_v = J^{-1}(\eta_x F_v + \eta_y G_v). \end{aligned} \quad (2.36)$$

The transformation Jacobian J and grid metric terms are.

$$J^{-1} = x_{\xi} y_{\eta} - x_{\eta} y_{\xi}.$$

$$\xi_x = Jy_\eta, \quad \xi_y = -Jx_\eta, \quad \eta_x = -Jy_\xi, \quad \eta_y = J\xi. \quad (2.37)$$

For the left hand side of Eq. (2.35), the explicit Non-MUSCL TVD scheme can be written as

$$\hat{U}_{i,j}^{n+1} = \hat{U}_{i,j}^n - J_{i,j} \frac{\Delta t}{\Delta \xi} \left(\hat{F}_{i+1/2,j}^n - \hat{F}_{i-1/2,j}^n \right) - J_{i,j} \frac{\Delta t}{\Delta \eta} \left(\hat{G}_{i,j+1/2}^n - \hat{G}_{i,j-1/2}^n \right) \quad (2.38)$$

Where J is the Jacobian in transforming the coordinations from a physical domain (x, y) to a computational domain (ξ, η) .

The variables \hat{F} and \hat{G} are described using an artificial viscosity $\hat{\Phi}$.

$$\hat{F}_{i+1/2,j}^n = \frac{1}{2} \left(\hat{F}_{i,j}^n + \hat{F}_{i+1,j}^n + \hat{R}_{i+1/2} \hat{\Phi}_{i+1/2} \right) \quad (2.39)$$

The $\hat{R}_{i+1/2}$ is an eigen vector matrix and $\hat{\Phi}_{i+1/2}$ is a vector with the elements $\hat{\Phi}_{i+1/2}^l$ ($l = 1, 2, 3, 4, 5$). The variables used in the above equations are

$$\hat{\Phi}_{i+1/2} = \left\{ \hat{\Phi}_{i+1/2}^l \right\} = \left\{ \sigma \left(a_{i+1/2}^l \right) \left(g_{i+1}^l + g_i^l \right) - \psi \left(a_{i+1/2}^l + \gamma_{i+1/2}^l \right) \alpha_{i+1/2}^l \right\}; \quad l = 1 \sim 5. \quad (2.40)$$

$$\sigma(z) = \frac{1}{2} \left\{ \psi(z) - \frac{\Delta t}{\Delta \xi} z^2 \right\} \quad (2.41)$$

$$\psi(z) = \begin{cases} z & ; |z| \geq \delta_l \\ (z^2 + \delta_l^2) / 2\delta_l & ; |z| < \delta_l \end{cases} \quad (2.42)$$

δ_l is a function that defines the range of entropy correction, and should be a function of the contravariant velocity and the corresponding sound speed for the computations. The form of the function used here is

$$\delta_l = \bar{\delta} \left(|U| + |V| + c \sqrt{\xi_x^2 + \xi_y^2 + \eta_x^2 + \eta_y^2} \right) \quad (2.43)$$

With a constant $\bar{\delta}$ set to 0.15. More details about the scheme can be found in Yee [25].

The minmod limiter, simplified form of which can be found in Yee [25], was used to avoid the numerical oscillations at the discontinuity. Among the various approximate Riemann solvers, we used the Roe's average, which is the most common one due to its simplicity and ability to return to the exact solution whenever the variables lie on a shock or contact discontinuity.

The time step for calculation is determined by

$$\Delta t = \frac{CFL}{\max \left\{ |U| + |V| + a \left(\xi_x^2 + \xi_y^2 \right)^{\frac{1}{2}} + c \left(\eta_x^2 + \eta_y^2 \right)^{\frac{1}{2}} \right\}} \quad (2.44)$$

The contravariant velocities are

$$U = \xi_x u + \xi_y v, \quad V = \eta_x u + \eta_y v \quad (2.45)$$

The courant-friedrichs-lewy, CFL number is kept as high as possible toward unity for the near steady flow, but is set to as low as 0.01 at the beginning of calculation because of unsteadiness. Here the CFL number is chosen as 0.9 to obtain rapid convergence and avoid unsteadiness in calculation.

3.5 Boundary Conditions and Convergence Criterion

A stream of air enters in the calculation domain from the left-bottom boundary and a stream of hydrogen enters from the left-upper boundary. The resultant velocities of hydrogen (u_1) and air (u_2) are shown in Fig. 3.1 (a). For hydrogen flow, the velocity, $u_1 \cos(\alpha/2)$ is set for x-direction and velocity $u_1 \sin(\alpha/2)$ is set for reverse of y-direction. Similarly for air flow, the velocity, $u_2 \cos(\alpha/2)$ is set for x-direction and velocity, $u_2 \sin(\alpha/2)$ is set for y-direction. Between two inlet streams there is a finite-thickness base. The flow domain is assumed to be open in the right side. The Navier-Stokes analysis imposes that the normal and tangential velocity component are zero on the walls. The upper and lower walls, and base wall are assumed to be thermally adiabatic so that the normal derivation of temperature must vanish giving $(\partial T / \partial n)_w = 0$. The normal derivation of species mass fraction must also vanish, and consequently the gradient of total density becomes zero along the adiabatic wall. The pressure is calculated from the equation of state. The temperature, pressure and density at inflow boundary are assured steady. At the outflow boundary the variable are determined by first-order extrapolation. Throughout the present study, the following convergence criterion has been set on the variation of density:

$$\sqrt{\frac{\sum_{J=1}^{JJ} \sum_{K=1}^{KK} \left(\frac{\rho_{new} - \rho_{old}}{\rho_{old}} \right)^2}{JJ.KK}} \leq 10^{-5} \quad (2.46)$$

Where JJ and KK are the total numbers of nodes in the horizontal and vertical directions respectively

2.6 Use of Turbulence Model

A zero-equation algebraic turbulence model developed by Baldwin and Lomax [26] is used to simulate boundary layer separation, recirculation and shock-expansion regions near the injector. The model is patterned with modifications

that avoid the necessity for finding the edge of the boundary layer. This has been very helpful because at the injection port and adjacent region it is difficult to define boundary layer thickness. According to the model the eddy viscosity μ_t is defined as

$$\mu_t = \begin{cases} (\mu_t)_{inner} & y \leq y_{crossover} \\ (\mu_t)_{outer} & y > y_{crossover} \end{cases} \quad (2.47)$$

Where y is the normal distance from the wall and $y_{crossover}$ is the smallest value of y at which the value of viscosity in the outer region becomes less than or equal to the value of viscosity in the inner region.

The viscosity in the inner region is given by

$$(\mu_t)_{inner} = \rho \cdot l^2 |\omega| \quad (2.48)$$

The mixing length in the inner region l is expressed as

$$l = ky \left[1 - \exp(-y^+ / A^+) \right] \quad (2.49)$$

Where

$$y^+ = \frac{\rho_w \mu_t y}{\mu_w} = \frac{\sqrt{\rho_w \tau_w} y}{\mu_w} \quad (2.50)$$

For two-dimensional flow, the magnitude of the vorticity is given by

$$|\omega| = \sqrt{\left(\frac{\partial u}{\partial y} - \frac{\partial v}{\partial x} \right)^2} \quad (2.51)$$

For the outer region,

$$(\mu_t)_{outer} = K C_{CP} \rho F_{WAKE} F_{KLEB}(y) \quad (2.52)$$

Where K is the Clauser constant, C_{CP} an additional constant, and

$$F_{WAKE} = \min\left\{ (y_{max} F_{max}), (C_{wk} y_{max} U_{dif}^2 / F_{max}) \right\} \quad (2.53)$$

Here F_{max} is the maximum value of the function

$$F(y) = y|\omega| \left[1 - \exp(-y^+ / A^+) \right] \quad (2.54)$$

at each y station in the flow domain, and y_{max} is the y coordinate at which this maximum occurs. The function $F_{KLEB}(y)$ is the Klebanoff intermittency factor given by

$$F_{KLEB}(y) = \left[1 + 5.5 \left(\frac{C_{KLEB} y}{y_{max}} \right)^6 \right]^{-1} \quad (2.55)$$

U_{dif} is the difference between the magnitude of the maximum and minimum total velocity in the profile at a fixed x station, expressed as

$$U_{dif} = \left(\sqrt{u^2 + v^2} \right)_{max} - \left(\sqrt{u^2 + v^2} \right)_{min} \quad (2.56)$$

Where $\left(\sqrt{u^2 + v^2} \right)$ is taken to be zero along all x station.

The outer formulation (Eqs. 2.52 and 2.53) can be used in wakes as well as in attached and separated boundary layer. The product $y_{max} F_{max}$ replaces $\delta^* u_c$ in the Clauser formulation and the combination $y_{max} U_{dif}^2 / F_{max}$ replaces δU_{dif} in a wake formulation. In effect, the distribution of vorticity is used to determine length scales so that the necessity for finding the outer edge of the boundary layer is removed.

The following are the constants used for this model and are directly taken from Baldwin and Lomax [26]:

$$\begin{array}{lll} A^+ & = 26, & C_{CP} = 1.6, & C_{KLEB} = 0.3, \\ C_{wk} & = 0.25, & k & = 0.4, & K & = 0.0168 \end{array}$$

The values of the turbulent thermal conductivity of the mixture κ_t and turbulent diffusion coefficient of i -th species D_{it} are obtained from eddy viscosity

coefficient μ_t by assuming a constant turbulent Prandtl and Lewis number equal to 0.91 and 1.0, respectively. They can be expressed as

$$\frac{\mu_t C_p}{k_t} = 0.91 \quad (2.57)$$

$$\frac{\rho D_{it} C_p}{k_t} = 1.0 \quad (2.58)$$

The final values of μ , κ and D_{im} used in the governing equations are

$$\mu = \mu_l + \mu_t \quad (2.59)$$

$$\kappa = \kappa_l + \kappa_t \quad (2.60)$$

$$D_{im} = D_{iml} + D_{it} \quad (2.61)$$

CHAPTER-III

RESULT AND DISCUSSION

3.1 Introduction

A numerical study on flow field behind a finite-thickness base in two non-parallel streams of hydrogen and air stream has been performed by solving Two-Dimensional Navier-Stokes equations. An explicit Harten-Yee Non-MUSCL Modified-flux-type TVD scheme has been used to solve the system of equations, and a zero-equation algebraic turbulence model to calculate the eddy viscosity coefficient. The object of this investigation is to study the characteristics of the flowfield, mixing efficiency and flame holding capability of a supersonic combustor. The performance of combustor has been evaluated by varying (i) merging angle of two streams (ii) height of the base thickness between two streams.

3.2 Flow Field Description and Numerical Parameter

The geometric configuration of the calculation domain and the inlet condition of two non-parallel streams is shown in Fig. 3.1 (a). The calculation domain is 0.1 m long and 0.04 m wide. The inlet stream widths used here are 0.015 and 0.0125 m. When the width of the stream is 0.015 m, the height of the base thickness is 0.01 m and when the width of the stream is 0.0125 m, the height of the base thickness is 0.015 m. The lower part of the left wall is allowed to enter air in the domain, having a Mach number of 2.5 and the upper part of the left wall is allowed to enter hydrogen in the domain, having a Mach number 0.9. The flow domain is assumed to be open in the right. The upper and lower boundaries are confined by adiabatic walls. In the present study, the variable parameters are merging angle of the streams and height of the base. All the numerical values of the variable parameters are shown in the Table 3.1. The Mach numbers are used supersonic for air and subsonic for hydrogen stream.

The Mach number 2.5 is chosen for the air stream as the computational simulation have been performed over the Mach number range [17] from 0.5 to 4.5 and 0.9 for hydrogen stream it is as the Mach number range from 0.14 to 1.28. Some features of this kind of flowfield are shown in Fig. 3.1 (b). It predicts the expansion at the separation points, formation of a recirculating regions bounded by two shear-layer mixing regions, recompression and reattachment shock, and boundary layer and shear layer. The grid system consists of 142 nodes in the longitudinal direction and 101 nodes in the transverse direction. The grid system of the solution domain is shown in Fig. 3.1 (c). The grid points around the left wall and behind the base are clustered. Results of these varying parameters are to be analyzed and discussed under the following contexts (i) the physics of fluid dynamics in two streams (ii) mixing of hydrogen and (iii) the characteristics of the flowfield.

3.3 Effect of Merging Angle

3.3.1 The Physics Of Fluid Dynamics

Figs. 3.2 (a-e) show the velocity vectors of the physical model. Direction of arrow indicates the flow direction and arrow length indicates the magnitude of velocity. The expansion, separation, recompression and reattachment region can be observed by these figures. The velocity vectors indicate that the flows expand sharply at base corner. Due to the base, hydrogen and air flows expand behind the base and forms a separation region. Both hydrogen and air flows move to each other and strike behind base at about 0.02 m from the bottom wall. After striking hydrogen flow deflects upward and airflow deflects downward sharply. Again these flows strike the upper and lower walls and then reflect. There is a pair of recirculation region moving in opposite direction behind the base. The upper recirculation rotates clockwise while the lower recirculation rotates counterclockwise. The maximum negative velocity in recirculations is lower than the inlet velocity of hydrogen or air. The flows expand sharply around the base and higher interaction occurs with the low velocity regions of both shear layers [3]. The strength of the interaction can be

understood from the slope of vectors at expansion region. For the two recirculations moving in opposite directions, hydrogen mixes with air and provides a mixing region [4]. The recirculations increase the mixing shear layer and cause penetration of hydrogen in air, resulting in higher mixing. Due to interaction between two streams, the velocity of the stream is slowed down and both hydrogen and air enter in recirculating region. Again by diffusion and convection, hydrogen enters into the recirculation region and mixes with air [5]. So recirculation plays a vital role on the mixing. Individually, in Fig. 3.2 (a) for case-1, the velocity vectors clearly show that hydrogen and air expand behind the base creating a separation flow region. The hydrogen stream has a freestream velocity of 1530 m/s before separation and expands sharply downward around the corner of the base to flow angle of approximate -31.5° (relative to the freestream). The air stream moves at a velocity of 1121 m/s before separation and then expands upward around the corner of the base at an angle of approximately 14° (relative to the freestream). The shear layer mixing regions spread with longitudinal distance until impingement occurs approximately 1.8 base height downstream of separation at $x = 0.018$ m, where the recirculation region ends (no negative streamwise velocity) and recovery of the wake deficit begins. The turbulent mixing, which occurs throughout the recompression and reattachment region quickly effects elimination of the velocity deficit. Figs. 3.2 (a) shows that due to the small merging angle, very weak interaction as well as penetration is occurred and consequently mixing is low. In Fig. 3.2 (a~e), merging angle affects the expanded angle both air and hydrogen at the base corner, shear-layer mixing and length of the recirculation regions. For cases (1~5), the downward and upward relative expanded angles at the base corner decrease with the increase of merging angle. The impingement point distance from the left wall decreases with the increase of merging angle, which indicates smaller recirculation zones. For example, in Fig. 3.2 (b) for case-2 the upper and lower expanded angle (relatively) at base corner are approximately -20.5° and 10° (respectively), which are smaller than case-1. The shear layer mixing regions spread with longitudinal distance until impingement occurs at

approximately $x = 0.013$ m, which is shorter than case-1. So the area of recirculating zones in case-2 are smaller than case-1.

Figs. 3.3 (a~d) show the velocity (magnitude) profiles at different x -location along the vertical axis. The resultant velocity is calculated by using u - and v -velocities. These figures only indicate the magnitude of velocity in various location along the vertical axis, y . These profiles are obtained at four x -locations chosen to examine distinctly different regions of the flowfield: $x = 0.005$ m where separated shear layers and recirculations are present, $x = 0.015$ m near the impingement region and interaction region, $x = 0.03$ and $x = 0.05$ m at far downstream region. These Figures show the patent of the velocity profiles and magnitude of velocities in the flowfield. Fig. 3.3 (a) shows that the velocity in recirculating regions is lower. The velocity at impingement point is almost zero as shown in Fig. 3.3 (b). Figs. 3.3 (c~d) show the velocity profile of the shear layer region and wall boundary layers. The boundary layers of lower wall are thicker than that of upper wall. These Figures also show that the velocity of hydrogen is very high due to the pressure gradient along the flow [18]. In Fig 3.3 (c), the bottom wall boundary layer rapidly becomes thick due to very small separated region. To see the strength of recirculation and magnitude of the negative velocity, lengthwise velocity profiles, non-dimensionalized by the freestream velocity ($u_1=1530$ m/s) of hydrogen are shown in Fig. 3.4 (a). Only case-1 and case-2 are discussed for these type of profiles. The dashed line at x value represents the streamwise location of the traverse and the $u/u_1 = 0$ plane for that set of data. The series of profiles indicate the large negative velocities occurring in recirculating region and the recovery of the velocity defect with downstream distance. The spreading of velocity profiles in each shear layers are very sharp at the $x = 0.0025$ m. The transverse velocity profiles, non-dimensionalized by the freestream velocity ($u_1=1530$ m/s) of hydrogen, are shown in Fig. 3.4 (b). The large values of v/u_1 occurring for the upper stream indicate the strong expansion.

3.3.2 Mixing of Hydrogen

Figs. 3.5 (a~e) show the penetration and mass concentration of hydrogen in the flow field. The concentration ratio contour allows the growth of the mixing layer clearly. As can be seen Figs. 3.5 (a~e), the mixing layers grow along the flow direction. Penetration and mixing of hydrogen in air can occur by means of (i) weak interaction between two steams (ii) turbulence and convection due to recirculation and velocity of the flow and (iii) molecular diffusion [5]. The downward hydrogen flow and upward airflow interact and mix due to vertical entrainment and molecular diffusion. Due to weak interaction, low gradient of hydrogen mass concentration exists causing weak penetration of hydrogen. For all cases (1~5), the mole fraction contours of hydrogen are concentrated in narrow region. Mole fraction contours show that the mixing shear-layer is relatively narrow in width at interaction region of hydrogen and air. The width of the mixing layer is defined as the length from the location of 5% to that of 100% concentration ratio of hydrogen. The mixing shear-layer width increases almost monotonously with the x -direction. The width of mixing layer at far downstream increases with merging angle. As the lower flow is air and upper flow is hydrogen, the significant density gradient (the density of air and hydrogen is 1.05 and 0.194 Kg/m³, respectively) exists at the interface and hydrogen mixes with air in one region at the upper flow of air. In this work, there is a pair of recirculation regions behind the base discussed separately. Out of two recirculation regions, the upper recirculation contains high concentration of hydrogen (mole fraction is about 0.85~0.95) due to the convection and strong expanded flow of hydrogen. On the other hand, in lower recirculation region hydrogen mixes with air by convection and diffusion process. This region contains better proportion of hydrogen and air (mole fraction is about 0.65 ~ 0.85), which is capable of burning. Throughout the mixing shear-layer, most of the mixing occurs by diffusion due to density gradient between air and hydrogen flows.

To clarify the concept of the flame holding, the effects of recirculation zone are discussed. A good understanding of flame holding is obtained basically

through the Damkohler number, which is defined as the ratio of residence time to the flow to the reaction time needed for complete combustion. Flame holding requires that throughout the whole burning range of the flame the residence time must always be larger than the reaction time. The residence time strongly depends on the geometric expansion of the recirculation zone. A longer recirculation zone results in a larger residence time and leads to a more stable flame [4]. Due to higher interaction for large merging angle, higher gradient of hydrogen mass concentration exists causing higher penetration of hydrogen, and due to small merging angle, large and elongated downstream recirculations cause better penetration dominated by convection and diffusion. Most of the recirculations contain hydrogen. For large merging angle, most of the recirculations contain high concentration of hydrogen. It can be pointed out that the equivalence ratio of fuel and oxidizer in mixture is an important factor for burning because along the mixture, the stoichiometric mixture strength is good for combustion. Therefore, longer recirculation zone containing good stoichiometric mixture strength results in a longer residence time and leads to a more stable flame. Case-1 having merging angle 10^0 can produce larger and elongated recirculations, where the lower recirculation contains better proportion of hydrogen and oxygen (mole fraction of hydrogen is about 0.65 ~ 0.85). Therefore, flame holding capability is better than other cases.

However, The larger recirculating region does not mean higher mixing efficiency. The performance of different cases is evaluated by calculating mixing efficiency. Fig. 3.6 (a) shows mixing efficiency along the length of physical model for different cases.

Mathematically, the mixing efficiency is defined by

$$\eta_m = \frac{\int_A \left(\int_H \rho \vec{u} \cdot d\vec{A} \right) / \phi}{m_H / \Phi}$$

Where,

A = arbitrary section plane

\int_H = local mass fraction of hydrogen

ρ = total density

\vec{u} = velocity vector

$d\vec{A}$ = small area normal to velocity vector

m_H = total mass flux of hydrogen

$$\phi = \text{local equivalence ratio} = \begin{cases} 0.25 & \phi < 0.25 \\ \phi & \phi \geq 0.25 \end{cases}$$

$$\Phi = \text{global equivalence ratio} = \begin{cases} 0.25 & \Phi < 0.25 \\ \Phi & \Phi \geq 0.25 \end{cases}$$

In the flow field where large amount of hydrogen is present with negligible amount of oxygen, the calculation of mixing efficiency is avoided by dividing the large value of ϕ . On the other hand, where a very small amount of hydrogen is present, an error in calculation of mixing efficiency can be occurred by the small value of ϕ . This error has been eliminated by setting the minimum value of $\phi = 0.25$ which corresponds to the lower flammability limit. It can be pointed out that similar expression for mixing efficiency was used by Yokota et al. [27~28]. In this investigation the global equivalence ratio for all cases is $\Phi=8.75$. Fig. 3.6 (a) shows that for all cases the mixing efficiency increases sharply just behind the base due to strong expansion of the flows around the base corner and recirculations. Generally, in recirculation region, the increment of mixing is high and then it is slow. The increasing rate of mixing is very slow at far downstream because of the supersonic nature of flow [1, 17]. Individually, case-1 starts with the lowest mixing efficiency and has the highest increment of mixing efficiency near the base. The overall mixing efficiency at the outflow boundary is lowest among the cases considered. By comparing all the cases, it can be observed that the mixing efficiency in recirculation regions as well as the overall mixing efficiency at the outflow boundary increases with increasing merging angle up to 40° and then decreases. The effect of merging angle on overall mixing efficiency is shown Fig. 3.6 (b) for cases (1~5). In this figure mixing efficiency is plotted

against the merging angle. The mixing efficiency sharply increases to 40° . But the figure shows that the increasing rate of mixing efficiency with the merging angle up to 40° is slower than the decreasing rate after 40° .

3.3.3 Characteristics of the Flow Field

The characteristics of the flow field are shown in Figs. 3.7 (a~e), 3.8 (a~d), 3.9 and 3.10 (a~e). Pressure contour is useful for visualizing expansion, recompression and reattachment shocks and waves in the flowfield. Figs. 3.7 (a~e) show pressure contours by which the pressure distribution and different shocks in whole domain can be understood. The expansion shock from the base corner, and the recompression shock forming downstream of expansion shock are clearly seen. Entering into the flowfield, the hydrogen and airflows interact after recirculation region, hydrogen flow is deflected upward, and airflow is deflected downward. These deflections indicate the recompression shock and redevelopment zones, which are clearly seen in these figures. This recompression shock strikes the wall and reflects. These deflections form a number of reattachment and recompression shock in far downstream. The deflection angles of upper shocks are larger than lower shocks. The recompression zone moves toward the left wall with the increase of merging angle. The recompression shock becomes stronger with the increase of merging angle. Figs. 3.7 (a~e) also show that the recirculation region behind the base is low-pressure region. This low-pressure region tends to be an area of constant pressure with increasing merging angle. The maximum pressure in Fig. 3.7 is about 758.6 kPa and occurs near the exit of the hydrogen stream.

Figs. 3.8 (a~d) show the pressure distribution along the vertical axis at 0.005, 0.015, 0.03 and 0.05 m from the left wall. For all cases (1~5), Fig. 3.8 (a) shows the pressure distributions in the recirculating region. This figure indicates that the pressure in recirculating region is low and this pressure for case-1 is lower than that of other cases. But the pressures in this region for cases (4~5) are high due to early formation of recompression. So it can be foretold that the pressure in recirculating region increases with merging angle.

The strong pressure rise occurs at recompression and impingement region shown in Fig. 3.8 (b). The pressure of that location increases with merging angle. However, the pressure in the flowfield after the redevelopment region decreases with the increase of merging angle shown in Figs. 3.8 (c) and 3.8 (d). The pressure at different region such as the recirculation, recompression, redevelopment and reattachment process can be clearly seen by the profile of static pressure along a centerline extending downstream from the vertical center of the thickness base shown in Fig 3.9. The static pressure is non-dimensionalized by the inlet pressure of air (0.15 MPa) and the streamwise distance is non-dimensionalized by the value of thickness base height ($h=0.001$ m). Fig. 3.9 indicates the lower pressure existing in the recirculating region just downstream of the base and the strong pressure rise which occurs during the recompression and impingement process for the two shear layers. When the merging angle is small, the pressure in recirculating region decreases sharply. However, the pressure in recirculation region tends to become constant with the increase of merging angle. The Fig. 3.8 also shows that the base pressure and the maximum pressure in recompression and redevelopment region increase with merging angle. The maximum pressure in recompression and redevelopment region for cases 1 and 2 are about 274 kPa and 343.5 kPa respectively. The maximum pressure rise of P/P_{ref} indicates the strong mixing and diffusionlike processes occurring in the recirculation regions because the diffusion of hydrogen is inversely proportional with pressure distribution. So low pressure indicates higher diffusion and higher diffusion means better mixing in recirculation region. The distance of the highest value of P/P_{ref} decreases with the increase of merging angle, which indicates that recompression region moves toward the left wall. Far away from the left wall, the centerline pressure profile shows low pressure and wavy nature with small amplitude due to the number of weak recompression and reattachment shock.

Figs. 3.10 (a-e) show temperature contours, which are useful for visualizing shear layer in the flowfield. The mixing shear layer initially is thin and then moderate due to recirculation. The maximum temperature rises about 1160K

at near the walls due to the adiabatic wall. The high pressure and temperature are obtained in recompression and redevelopment region. The maximum temperature in this region for case-1 and 2 are 1062K and 1157K respectively.

3.4 Effect of Base Thickness

3.4.1 The Physics of Fluid Dynamics

Figs. 3.11 (a-c) for cases (6~8) show the velocity vector of the physical model. Direction of arrow indicates the flow direction and arrow length indicates the magnitude of velocity. There is a pair of large and elongated recirculation, just behind of the base. Upper recirculation rotates clockwise and lower recirculation rotates counterclockwise. The vector indicates that the velocity in recirculating region is low and it is also lower than that of cases (1~5). The area of the recirculating zones is larger and elongated than that of cases (1~5). For the higher thickness base, larger and elongated recirculations are formed due to wide space [6]. The flows expand sharply around the base corners to match pressure gradient. Weak interaction occurs between air and hydrogen flows due to expand of the flows significantly and form a larger recirculation region. The interaction between air and hydrogen flows increase with the increase of merging angle. The strength of interaction can be understood from the slope of vectors at interaction region. For long distance between two flows, both air and hydrogen flows lose their strength due to viscous action and recirculation. Due to the interaction, the velocities of air and hydrogen flows are slowed down and both hydrogen and air enter into the recirculations. Again with the two recirculations moving in opposite direction, hydrogen mixes with the air and provides a mixing region. The recirculations increase the mixing shear layer and cause the penetration, resulting in higher mixing. By diffusion and convection process, hydrogen also enters into the recirculating region and mixes. So recirculation plays a vital role on the mixing.

Figs. 3.11 (a~c) also predict expansion, recompression and reattachment of the shear layer. The expansion, recompression, and reattachment are more clearly observed in upper side of the flowfield because of higher velocity vectors of hydrogen. The movement of the velocity vectors is discussed earlier. An additional separation region, small in area, is appeared near the bottom wall at approximately 0.005 m from left wall but it has no contribution on mixing. This separation region increases with merging angle. Individually, Fig. 3.11 (a) for case-6 shows the separation flows from the base, with resulting large separated flow region. The shear-layer mixing regions spread along lengthwise distance until impingement occurs approximately at $x = 0.021$ m, where the recirculation ends. This Figure also shows that the upper stream expands sharply downward around the corner of the base to a flow angle of approximately -23.5° (relative to freestream) and lower stream expands sharply upward at the corner of the base a flow angle of approximately 15° (relative to freestream). The distance of the impingement point for case-7 is 1.8 from the left wall shown in Fig. 3.11 (b). Figs. 3.12 (a~d) show the resultant velocity profiles along the vertical axis at 0.005, 0.019, 0.03 and 0.05 m from left wall. These Figures show the patent of the velocity profiles and magnitude of velocities in the flowfield. The boundary layers of bottom wall are thicker than that of upper wall. These Figures also show that the velocity of hydrogen (downstream of the flowfield) is very high due to the pressure gradient along the flow [18]. Fig. 3.12 (a) shows that the velocity is low in the recirculating region. Fig. 3.12 (b) indicates that the velocity in impingement point is about zero. Figs. 3.12 (c~d) show the velocity profile of the shear layer region and wall boundary layer at far downstream. In Fig 3.12 (d), the boundary layer of bottom wall rapidly become thick due to separated region. In Fig. 3.13 (a) lengthwise velocity profiles, non-dimensionalized by the freestream velocity ($u_1=1530$ m/s) of hydrogen, show strength of recirculation and magnitude of the reverse flow. Only case-6 and case-8 are discussed for these types of profiles. The series of profiles indicate the large negative velocities occurring in recirculating region and the recovery of the velocity defect with downstream distance. The transverse mean velocity profiles, non-dimensionalized by the freestream velocity ($u_1=1530$ m/s) of

hydrogen, are shown in fig. 3.13 (b). The large values of v/u_1 occurring for the upper stream indicate the strong expansion. By comparing between Fig. 3.4 (b) and Fig. 3.13 (b) it can be pointed out that the expansion at $x = 0.0025$ m is stronger when the base thickness is 0.015 m.

3.4.2 Mixing of Hydrogen

Figs. 3.14 (a~c) show the penetration and mass concentration of hydrogen in the flow field. With increase the height of base the recirculation regions behind the base also become large discussed previously. The flows expand sharply due to wide space around the corner of base, which cause the strong interaction. But the interaction between air and hydrogen flows is weak. So it is pointed out that (i) due to weak interaction of the flows, small gradient of hydrogen mass concentration exists causing low penetration of hydrogen and (ii) larger and elongated recirculations cause high penetration dominated by convection and diffusion in recirculation. Figs. 3.14 (a~c), Mole fraction contours of hydrogen show that the mixing shear-layer at interaction region of hydrogen and air is relatively narrow in width. Mole fraction contours of hydrogen are concentrated in this narrow region. Mixing shear-layer width has been discussed earlier. The mass concentration of hydrogen in upper and lower recirculating region can be explained separately. The upper recirculation contains high concentration of hydrogen (mole fraction is about 0.85 ~ 0.95) due to the convection, diffusion and expanded flow of hydrogen. On the other hand, in lower recirculation region, hydrogen mixes with air by convection and diffusion process. This region contains better proportion of hydrogen and air (mole fraction is about 0.6 ~ 0.85), which is capable of burning. Between two recirculations, upper recirculating region contains high concentration of hydrogen for all case (6-8). Again, the flame holding requires longer residence time of flame in the burning range and this residence time strongly depends on the geometric expansion of the recirculation zone [4]. Also the equivalence ration of fuel and oxidizer in mixture is an important factor for burning because among the mixture, the stoichiometric strength is good for combustion. Therefore, longer recirculation zone containing

stoichiometric mixture strength results in a longer residence time and leads to a more stable flame. So cases (6~8) have the better flame holding capability because they can produce larger and elongated recirculation. It can be pointed out that mixing and flame holding capability for cases (6~8) are better than that of cases (1~5) because of larger and elongated recirculation.

Fig. 3.15 (a) shows the mixing efficiency along the length of physical model for cases (6-8). Mathematically, the mixing efficiency is defined earlier. Fig. 3.15 (a) shows that mixing efficiency increases very sharply just behind the base. Generally, in the recirculation region, the increasing rate of mixing is high and then it is slow in downstream because of supersonic nature of flow. By comparing it can be observed that the mixing efficiency in recirculation regions as well as the overall mixing efficiency at the outflow boundary increases with increasing merging angle. For example, the overall mixing efficiency for cases 6, 7 & 8 are 36.92, 38.09 & 40.37% respectively. The effect of merging angle on overall mixing efficiency is shown Fig. 3.15 (b) for cases (6~8). In this figure mixing efficiency is plotted against the merging angle. The figure shows that the mixing efficiency at outflow boundary increases with merging angle. Fig. 3.15 (c) shows the comparison of mixing efficiencies between the base height 0.01 and 0.015 m for merging angles 10° , 20° and 40° . Figure shows that the mixing efficiency at the same merging angle is high when the base height is high.

3.4.3 Characteristics of the Flow Field

The characteristics of the flowfield are shown in Figs. 3.16 (a~c), 3.17 (a~c), 3.18 and 3.19 (a~c). Pressure contour is useful for visualizing expansion, recompression and reattachment shocks and waves in the flowfield. Figs. 3.16 (a~c) show pressure contours, by which the pressure distribution and different shocks in the flowfield can be understood. The expansion shock from the base corner, and the recompression shock forming downstream of expansion shock are clearly seen by these figures. Figs. 3.16 (a~c) also show that the recirculation region behind the base is low pressure region. This low-

pressure region tends to be an area of constant with increasing merging angle. The maximum pressure in fig. 3.16 is about 734 kPa and occurs near the exit of the hydrogen stream.

Figs. 3.17 (a~d) show the pressure distribution along the vertical axis at 0.005, 0.019, 0.03 and 0.05 m from the left wall. In Fig. 3.17 (a), the pressure profile indicates that pressure is low in recirculation region. Figs. 3.17 (b~c) shows that pressure is high in recompression and impingement region. As diffusion of hydrogen is inversely proportional with pressure distribution so diffusion of hydrogen is better in low pressure recirculating region. These figures also indicate that the pressures in downstream region of flowfield are lower than that of the cases (1~5). Fig. 3.18 shows the centerline pressure profiles for the near-wake interaction region along the longitudinal axis at 0.02 m from the bottom wall. The static pressure is non-dimensionalized by the inlet pressure of air and streamwise distance is nondimensionalized by the value of 0.01 ($h = 0.01$ m). This figure indicates relatively low pressure existing in the recirculation region just downstream of the base and the strong pressure rise, which occurs during the recompression and impingement process for the two shear layers. When the merging angle is small, the pressure in recirculating region decreases sharply. However, the pressure in recirculation region tends to become constant with the increase of merging angle. Fig. 3.18 also shows that the base pressure and the maximum pressure in recompression and redevelopment region increase with merging angle. The maximum pressure in recompression and redevelopment region for cases 6 and 7 are about 259 kPa and 270 kPa respectively. This figure also indicates that the pressures in recompression and redevelopment region are lower than that of the cases (1~5). Low pressure indicates higher diffusion and higher diffusion means better mixing in recirculation region. The distance of the highest value of P/P_{ref} decreases with the increase of merging angle, which indicates that recompression region moves toward the left wall. Far away from the left wall, the centerline pressure profile indicates low pressure and wavy nature due to the number of weak recompression and reattachment shock. Figs. 3.19 (a-c) show temperature contours, which are useful for visualizing shear layer in the

flowfield. The mixing shear layer initially is thin and then moderate due to recirculation. The maximum temperature rises about 1160K at near the walls due to the adiabatic wall. The maximum temperature in this region for case-6 and case-8 are about 1050K and 1060K.

CHAPTER-IV

CONCLUSION

4.1 Summary of the Study

The numerical result on mixing of hydrogen in supersonic air stream separated by a thickness base has been studied by solving Two- Dimensional Navier-Stokes equations. A zero-equation turbulence model proposed by Baldwin and Lomax has been used to calculate the eddy viscosity coefficient. The ultimate goal of this study is to observe the characteristics phenomena of the flow field, mixing efficiency and flame holding capability. This study has been completed by varying (i) Merging angle of two streams (ii) height of the thick base between two streams.

In present investigation merging angle and base thickness are varied. For the base thickness 0.01 m, the merging angles 10° , 20° , 30° , 40° and 50° are considered whereas for base thickness 0.015 m, the merging angles 10° , 20° and 40° are taken to study. The region of separated flow existing between two streams in near-wake exhibits vigorous recirculation, reverse low velocity, and strong interaction with the low-velocity regions of both shear layers. Out of two recirculations, the lower recirculation region contains better proportion of hydrogen and air. The flows expand sharply around the base and interactions occur between flows and recirculations. Consequently, strong mixing occurs due to penetration at the base. By varying merging angle. I have found that the interaction between air and hydrogen flows increase with merging angle but the area of recirculation region decreases. The increasing rate of mixing efficiency behind the base is high and then it is very slow. For 40° merging angle, the mixing efficiency is high but the flame holding capability comparatively low. For high merging angle (50°), both the mixing efficiency and flame holding

capability are low. The pressure existing in the recirculation region is low, which indicates that strong mixing and diffusion process occur in this region. The mixing shear-layer width at outflow boundary increases with merging angle. For small merging angle, the pressure in recirculating region initially decreases and then increases. The pressure in this region becomes nearly constant with the increase of merging angle. The base pressure and the maximum pressure in recompression and redevelopment region increase with merging angle.

Investigation shows that the pair of recirculation for 0.015 m base thickness is larger and more elongated than that of 0.01 m due to more wide space behind the base. This larger and elongated recirculating region increases both the mixing efficiency and flame holding capability. At the same merging angle, the mixing shear-layer width at outflow boundary is thicker when the base thickness is high. But the recompression shock is weaker for high base thickness.

4.2 Recommendation for Future Study

The efficient mixing of fuel with oxidizer is very important factor in a supersonic combustor. But supersonic combustor faces many unsolved problems. To overcome these problems, more investigations are required. In shear layer mixing, mixing occurs only at the interface of the two flows. So the area of mixing regions is very important for the mixing enhancement. In this study, hydrogen can mix with airflow in one region (one interface) along the shear layer. The area of the mixing regions can't be increase by increasing either merging angle or base thickness. So a configuration will be found out so that mixing can occur in two or more interfaces. Zero-equation model is mathematically the simplest because it requires no additional field equation and contains only a few modeling constants. The two main limitations are (i) not suitable for complex separated flows and (ii) no account of convection and diffusion of turbulence. So two-equation turbulence model is suggested to overcome these difficulties. This is two-dimensional case. Three-dimensional calculations are required for real flowfield.

BIBLIOGRAPHY

- [1] Brown, G. L., and Roshko, A., "On Density Effects and Large Structure Turbulent Mixing Layers," *Journal of Fluid Mech.* Vol. 64, Part. 4, 1974, pp. 775-816.
- [2] Azim, M. A., and Islam A. K. M. S., "Plane Mixing Layers From Parallel and Non-Parallel Merging of Two Streams," *Experiments in fluids*, Vol. 34, 2003, pp. 220-226.
- [3] Amatucci, V. A., Dutton, J. C., Kuntz, D. W., and Addy, A. L., "Two-Stream, Supersonic, Wake Flowfield Behind a Thick Base, Part1: General Features," *AIAA Journal*, Vol. 30, No. 8, August 1992, pp. 2039-2046.
- [4] Tabejamaat, S., Ju, Y., and Niioka, T., "Numerical Simulation of Secondary Combustion of Hydrogen Injected from Preburner into Supersonic Airflow," *AIAA Journal*, Vol. 35, No. 9, September 1997, pp. 1441-1447.
- [5] Ahmed, S., "A Numerical Study on the Mixing of Hydrogen in Supersonic Air Stream," M. Sc. Dissertation, Department of Mechanical Engineering, Bangladesh University of Engineering and Technology, Bangladesh, December 2000.
- [6] Ali, M., "Physics of Supersonic Mixing and Combustion of a Transverse Jet in Two-Dimensional Finite Stream," Physical Gas Dynamics laboratory Department of Aerospace Engineering, Nagoya University, Japan, March 1998.
- [7] Berman, H. A., "A Numerical Solution of the Supersonic Flow Over a Rearward Facing Step with Transverse Non-Reacting hydrogen," *AIAA/ASME 3rd Joint Thermophysics, Fluid, Plasma and Heat Transfer conference*, St. Louis, Missouri, June 7-11, 1982.
- [8] Durst, F., Pereira, J. C. F., and Tropea. C., "The Plane Symmetric Sudden-Expansion Flow at Low Reynolds Number," *Journal of Fluid Mech.*, Vol. 248, 1993, pp. 567-581.

- [9] Fearn, R. M., Mullin, T. and Dliffe, K. A., "Nonlinear flow Phenomena in a Sudden Expansion," *Journal of Fluid Mech.* Vol. 211, 1990, pp. 595-608
- [10] Alleborn, N., Nandakumar, H., Raszillier, H., and Duret, F., "Further Contributions on the Two-Dimensional Flow in a Sudden Expansion," *Journal of Fluid Mech.*, Vol. 330, 1997, pp. 169-188
- [11] Umeda, Y., and Fujiwara, T., "Physics of Methane Combustion in Mixing Shear Layer," *Trans. Japan Soc. Aero. Space Sci.*, Vol. 38, No. 121, November 1995, pp. 265-281.
- [12] Takahashi, M., and Hayashi, A. K., " Numerical Study on Mixing of Injecting Jet into a Supersonic Flow," 3rd International Symposium Computational Fluid Dynamics, Nagoya, Japan, pp. 454-462.
- [13] Yokota, K., and Kaji, S., "The Injection Methods and Mixing Characteristics in the Two-dimensional Supersonic Free Stream," *Trans. Japan Soc. Aero. Space Sci.*, Vol. 38, No. 122, February 1996, pp. 383-393.
- [14] Lee, J., "A Numerical Study of Mixing in Supersonic Combustion With Hypermixing Injectors," AIAA-93-0215, NASA Contractor 191027, December 1992, pp. 1-25.
- [15] Gerlinger, P., Algermissen, J., and Bruggemann, D., "Numerical Simulation of Mixing for Turbulent Slot Injection," *AIAA Journal*, Vol. 34, No. 1, January 1996, pp. 73-78.
- [16] Moustafa, G. H., "Experimental Investigation of High-Speed Twin Jets", *AIAA Journal*, Vol. 32, No. 11, Technical Notes, pp. 2320-2322.
- [17] Liou, T-. M., Lien, W-. Y., and Hwang, P-. W., "Compressibility Effects and Mixing Enhancement in Turbulent Free Shear Flows," *AIAA Journal*, Vol. 33, No. 12, December 1995, pp. 2332-2338
- [18] Abe, T., Funabiki, K., Ariga, H., and Hiraoka, K., "Effect of Streamwise Pressure Gradient on the Supersonic Mixing Layer," Technical notes, *AIAA Journal*, Vol. 30, No. 10, pp. 2564-2566
- [19] Anderson, Jr. J. D., "Hypersonic and High Temperature Gas Dynamics," McGraw-Hill Book Company, New York, pp. 592-605, 1989.

- [20] Moss, J. N., "Reacting Viscous-Shock-Layer Solutions with Multicomponent Diffusion and Mass Injection," NASA TR-411, June 1974.
- [21] White, F. M., "Viscous Fluid Flow," McGraw-Hill Book Company, New York, pp. 592-605, 1974.
- [22] Wilke, C. R., "A Viscosity Equation for Gas Mixture," Journal of Chemical Physics," Vol. 18, No. 4, April 1950.
- [23] Ried, R. C., and Sherwood, T. K., "The Properties of Gases and Liquids," Second Edition, McGraw-Hill Book Company, New York, pp. 520-543, 1989.
- [24] Brokaw, R. S., "Alignment Charts for Transport Properties Viscosity, Thermal Conductivity, and Diffusion Coefficients for Nonpolar Gases and Gas mixtures at Low Density," NASA TR-81, 1961.
- [25] Yee, H. C., "A Class of High-Resolution Explicit and Implicit Shock Capturing Methods," NASA, TM101088, 1989.
- [26] Baldwin, B. S. and Lomax, H., "Thin Layer Approximation and Algebraic Model for Separated Turbulent Flows," AIAA paper, 1978, pp. 78-257.
- [27] Yokota, K., and Kaji, S., "The Three-dimensional Supersonic Flow and Mixing Fields with a Perpendicular Air Injected from a Finite Length Slit," Trans. Japan Soc. Aero. Space Sci., Vol. 39, No. 124, 1996, pp. 173-183.
- [28] Yokota, K., and Kaji, S., "the Effects of Aspect Ratio of A Finite Length Slit on the Mixing in the Three-dimensional Supersonic Flow," Trans. Japan Soc. Aero. Space Sci., Vol. 39, No. 124, 1996, pp. 199-210.

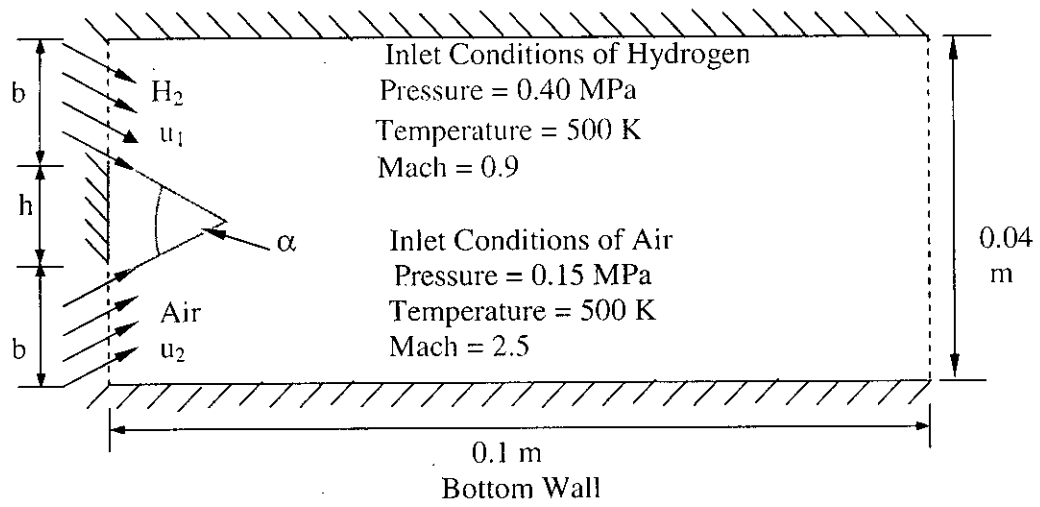


Fig. 3.1(a) Schematic with numerical parameters for varying the merging of air and hydrogen streams (Merging angle, $\alpha=10^\circ, 20^\circ, 30^\circ, 40^\circ$ & 50° ; Base thickness, $h = 0.01$ & 0.015 m; Inlet width, $b = 0.015$ & 0.0125 m)

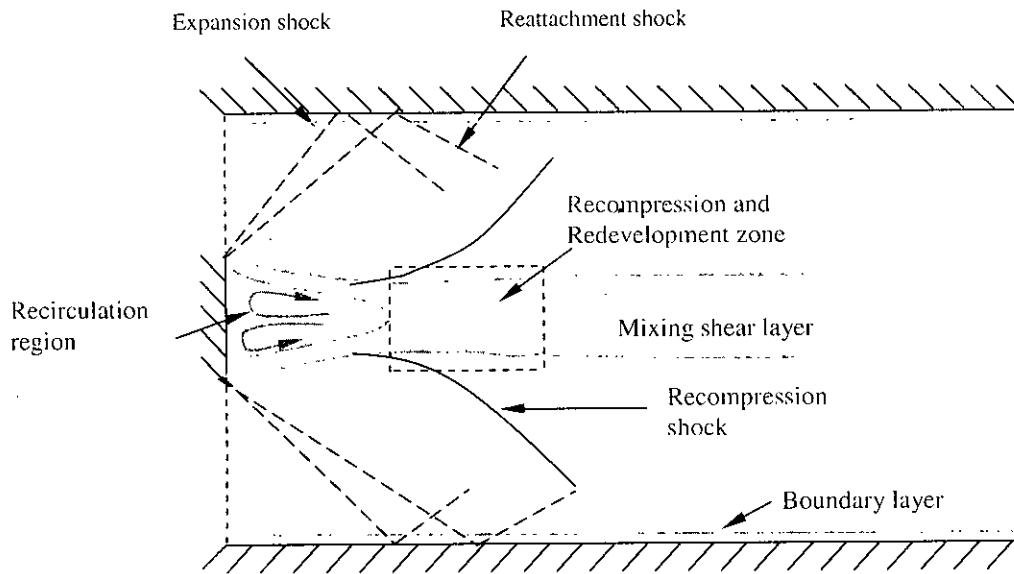


Fig. 3.1 (b) Detailed flowfield characteristics generated by the separation of two streams behind a thickness base.

Grid System of the Calculation Domain

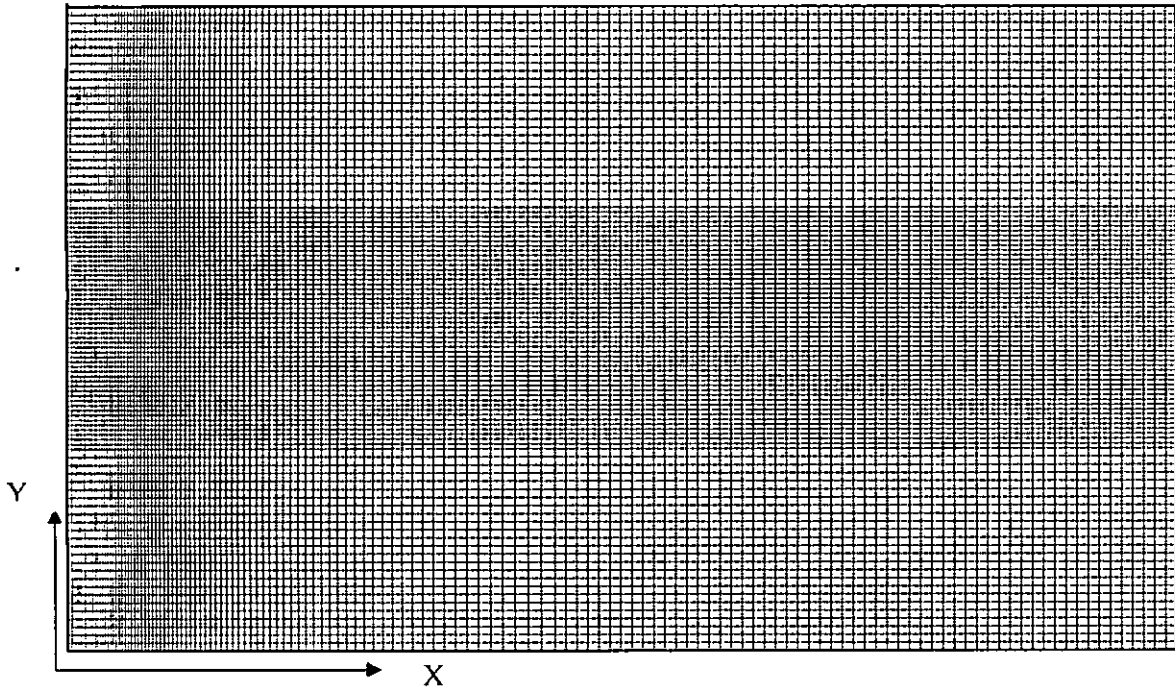


Fig. 3.1 (c) Grid system of the calculation domain.

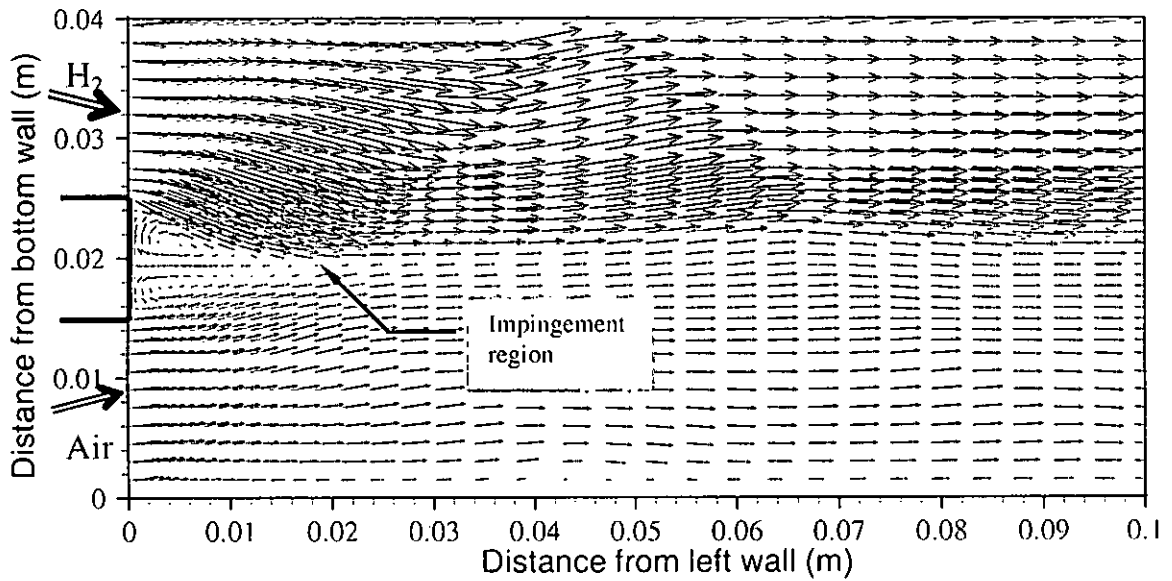


Fig. 3.2 (a) Velocity vector field of two streams; Case-1 ($\alpha = 10^0$).

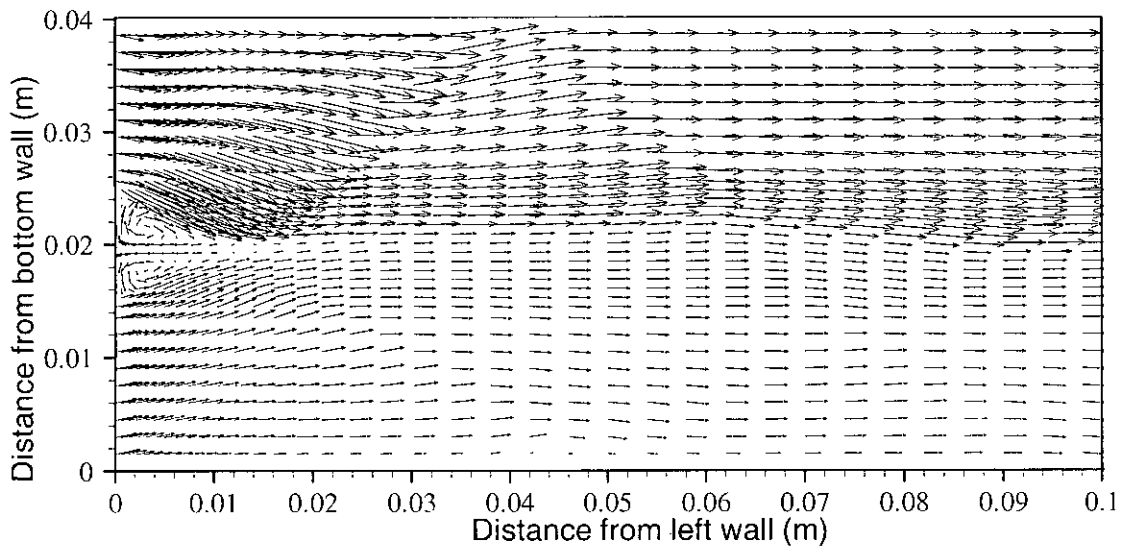


Fig. 3.2 (b) Velocity vector field of two streams; Case-2 ($\alpha = 20^\circ$).

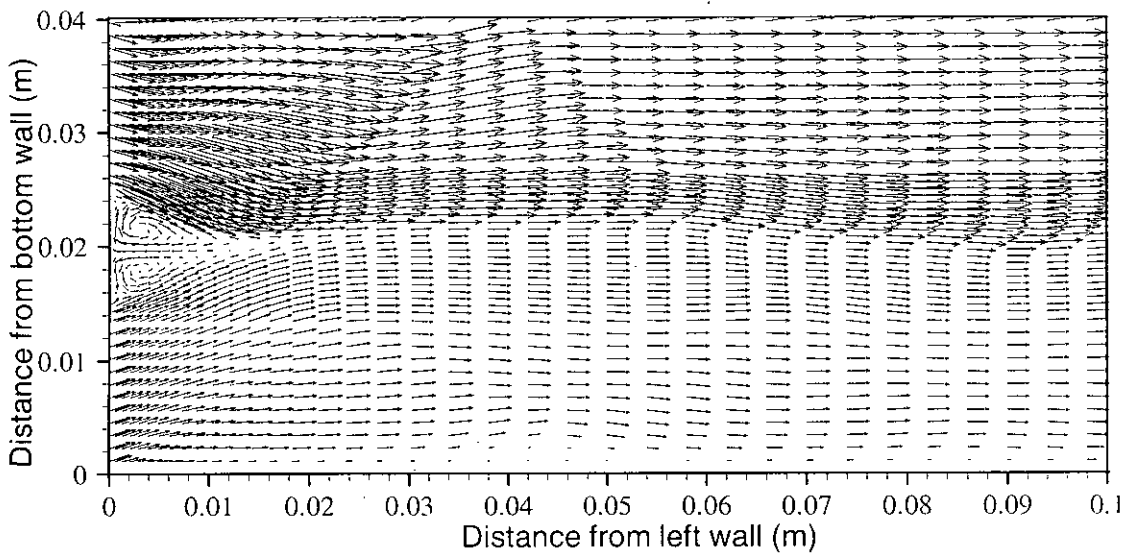


Fig. 3.2 (c) Velocity vector field of two streams; Case-3 ($\alpha = 30^\circ$).

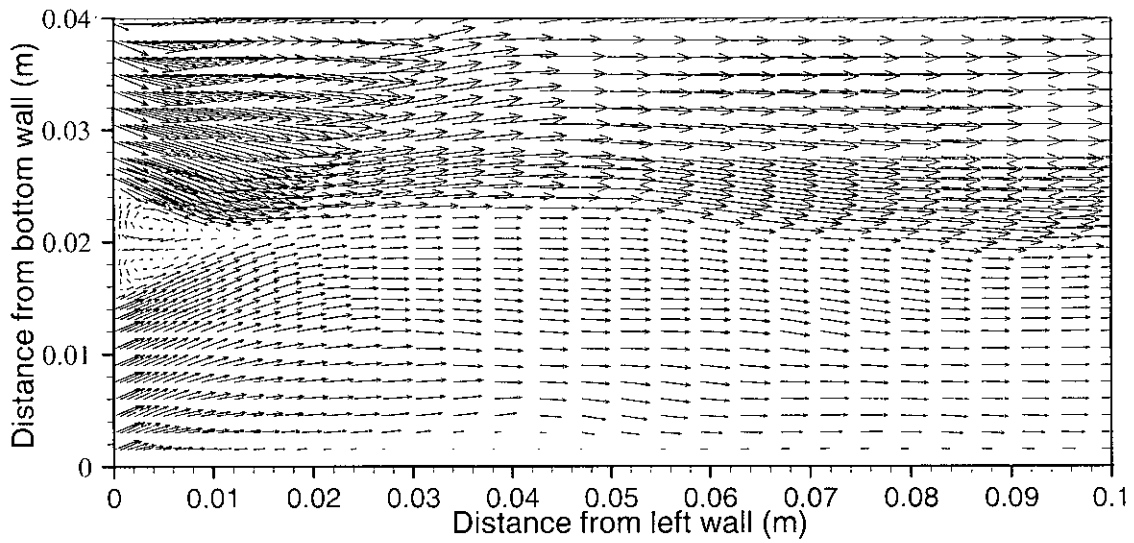


Fig. 3.2 (d) Velocity vector field of two streams; Case-4 ($\alpha = 40^\circ$).

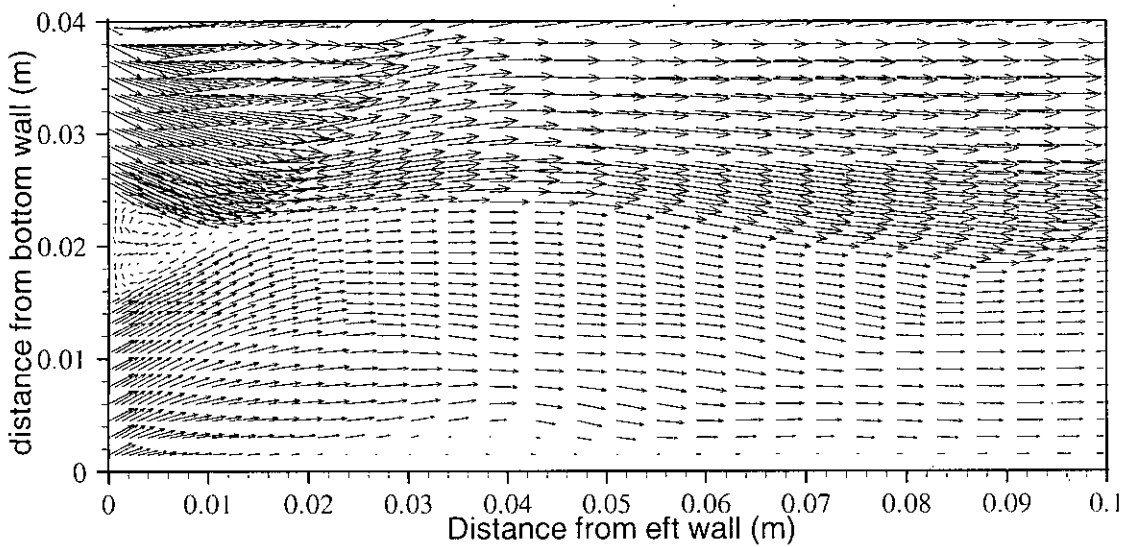


Fig. 3.2 (e) Velocity vector field of two streams; Case-5 ($\alpha = 50^\circ$).

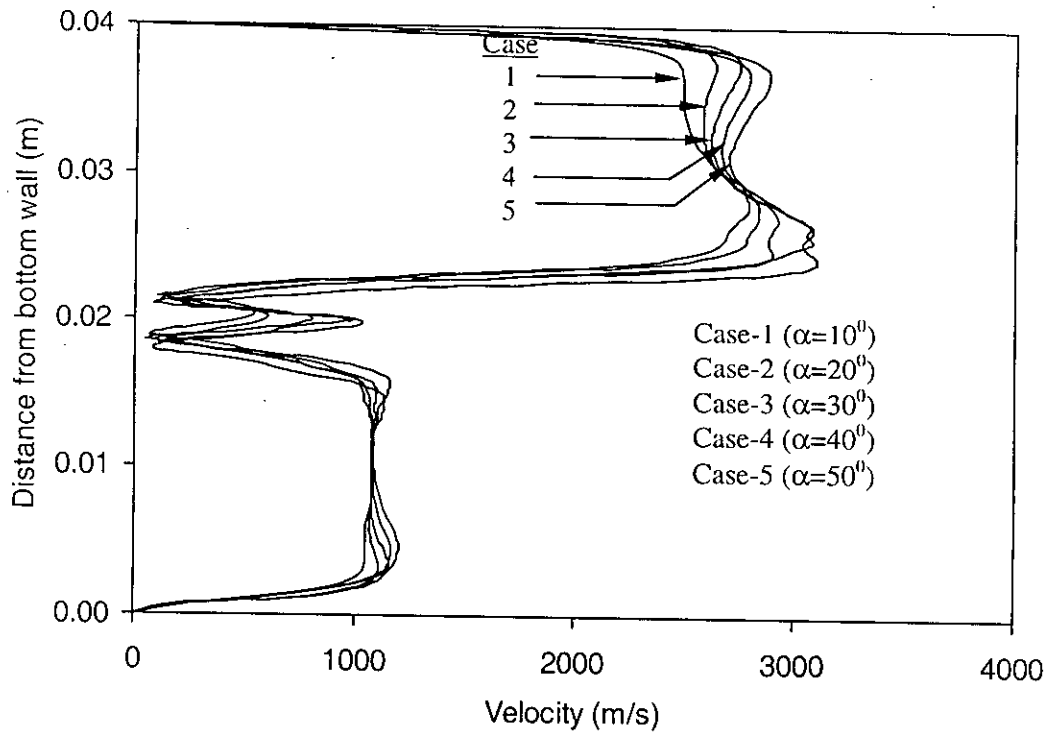


Fig. 3.3 (a) Velocity profiles at 0.005 m from left wall; Case (1~5)

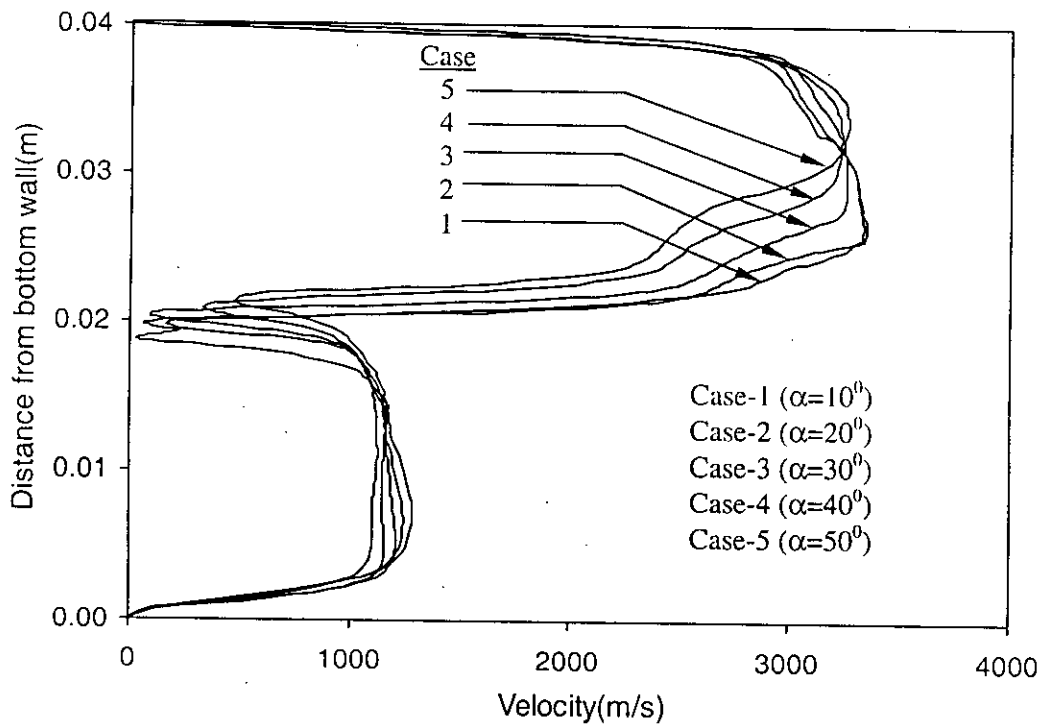


Fig. 3.3 (b) Velocity profiles at 0.015 m from left wall; Case (1~5)

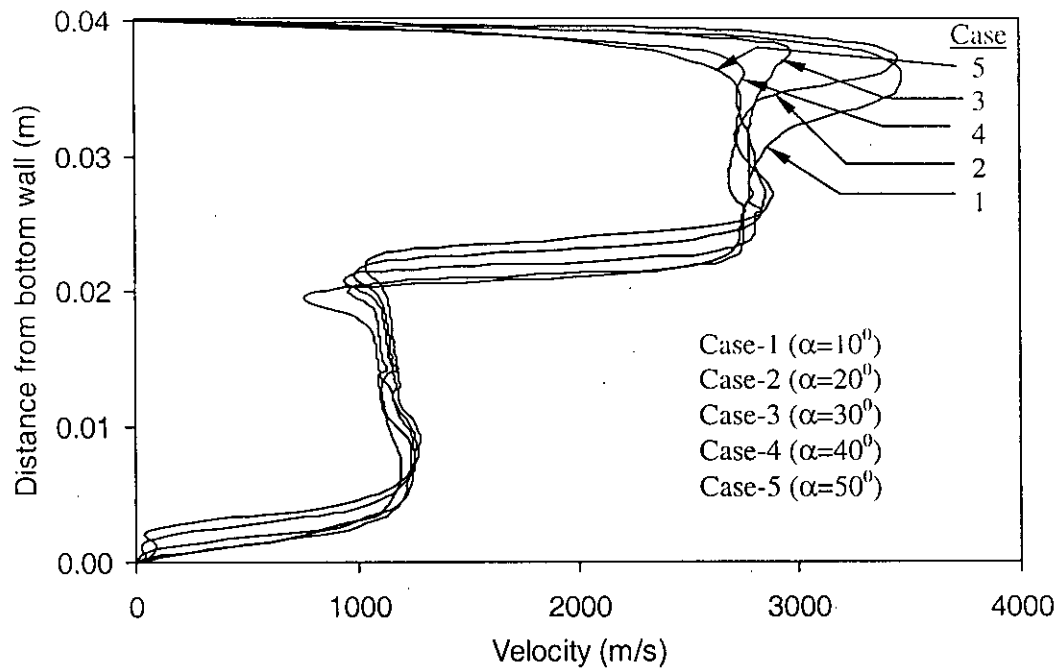


Fig. 3.3 (c) Velocity profiles at 0.03 m from left wall; Case (1~5)

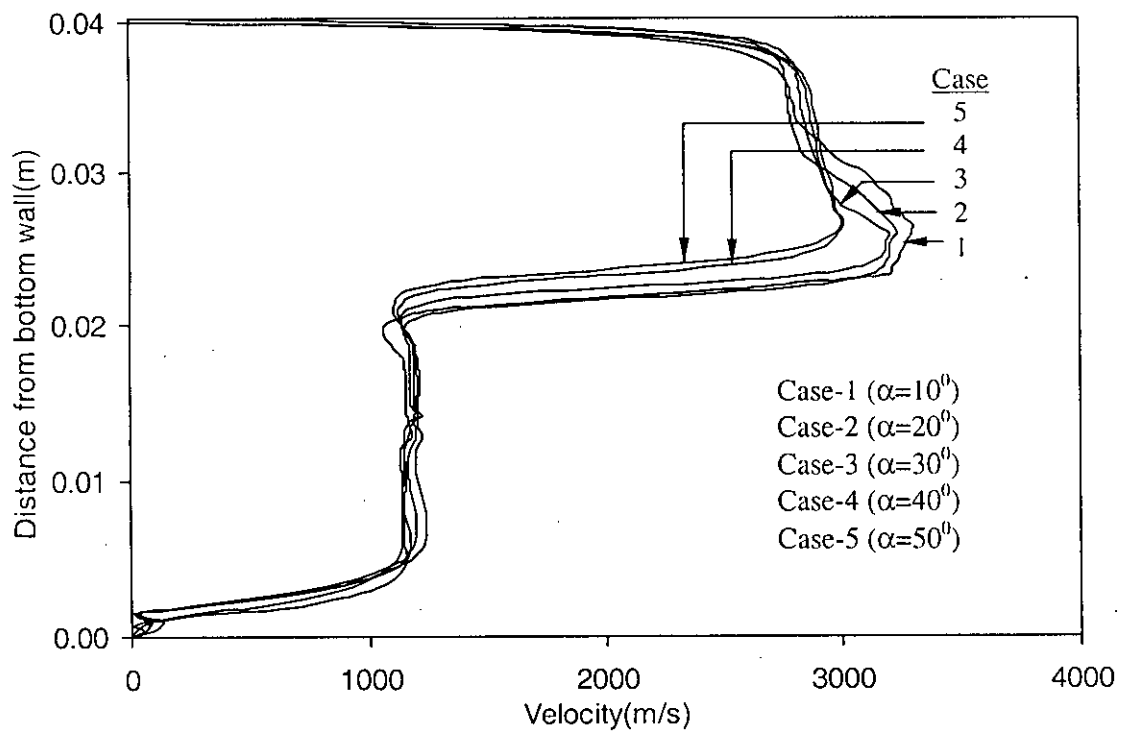


Fig. 3.3 (d) Velocity profiles at 0.05 m from left wall; Case (1~5)

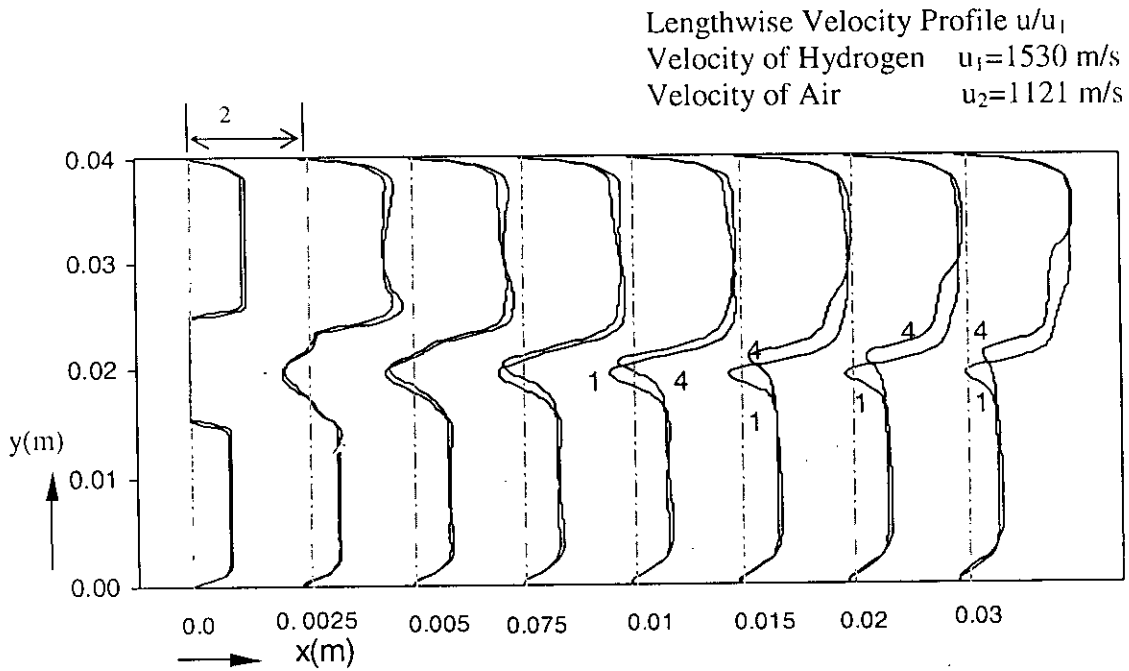


Fig 3.4 (a) Lengthwise velocity profiles for the two-stream interaction flowfield showing the near-wake region; (for Case-1 and case-4).

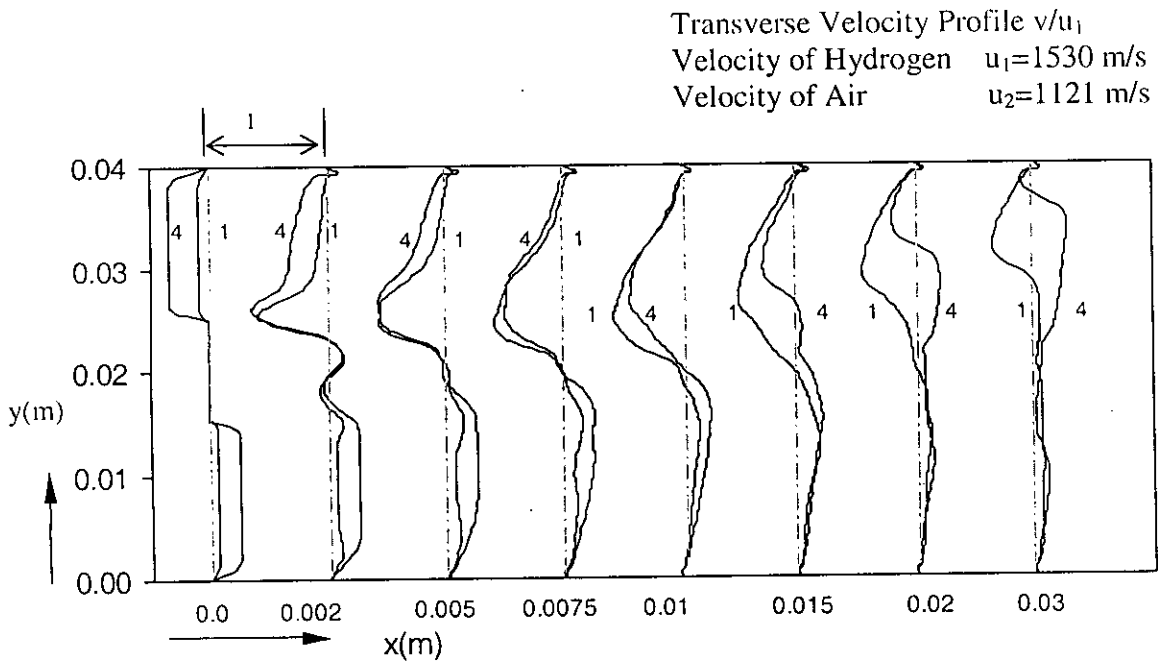


Fig 3.4 (b) Transverse velocity profiles for the two-stream interaction flowfield showing the near-wake region; (for Case-1 and case-4).

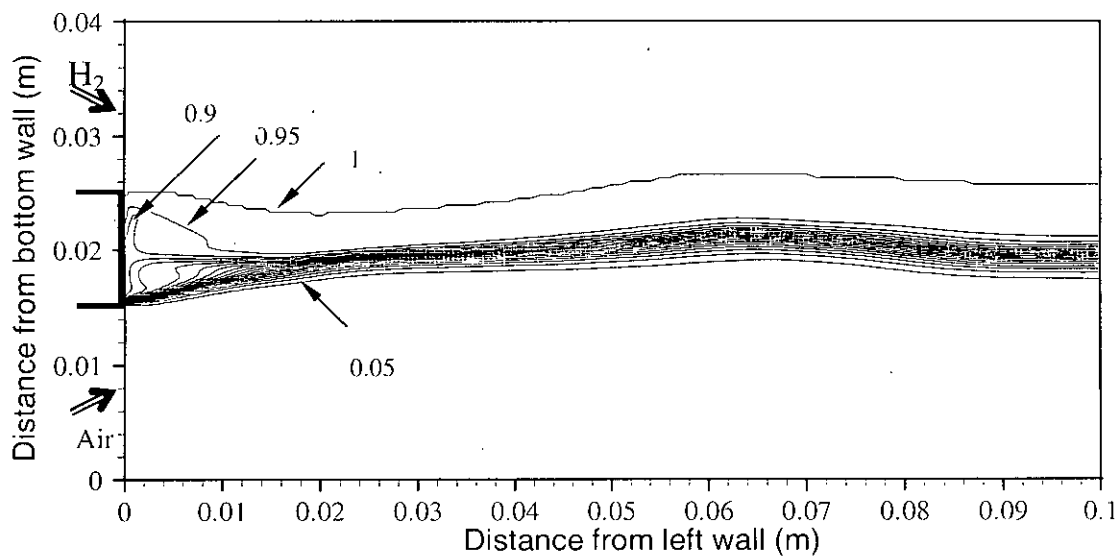


Fig. 3.5 (a) Mole fraction contour of hydrogen, ϕ (0.05,1.0,0.05); Case-1 ($\alpha = 10^0$).

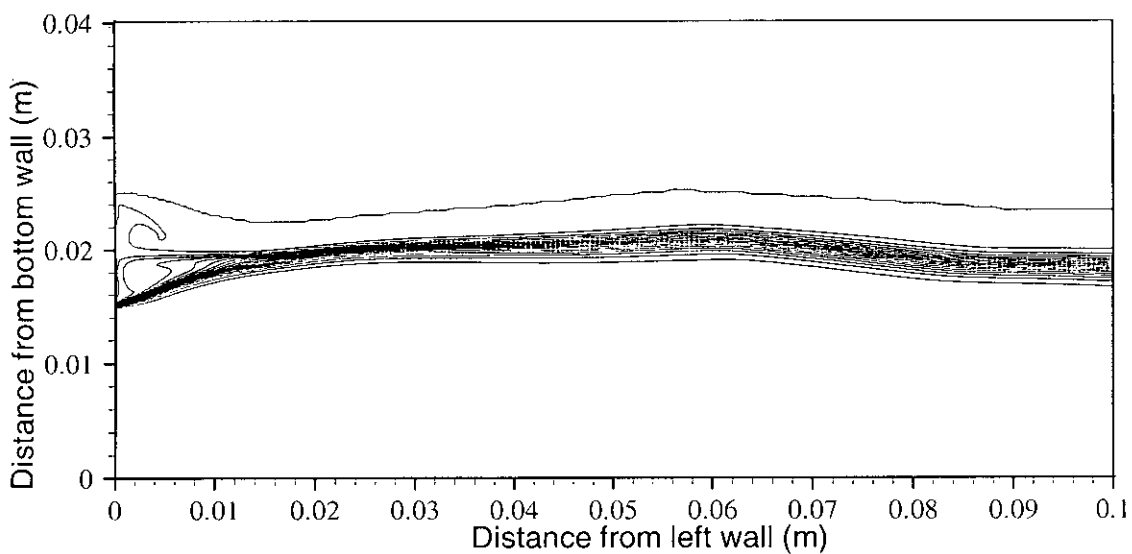


Fig. 3.5 (b) Mole fraction contour of hydrogen, ϕ (0.05,1.0,0.05); Case-2 ($\alpha = 20^0$).

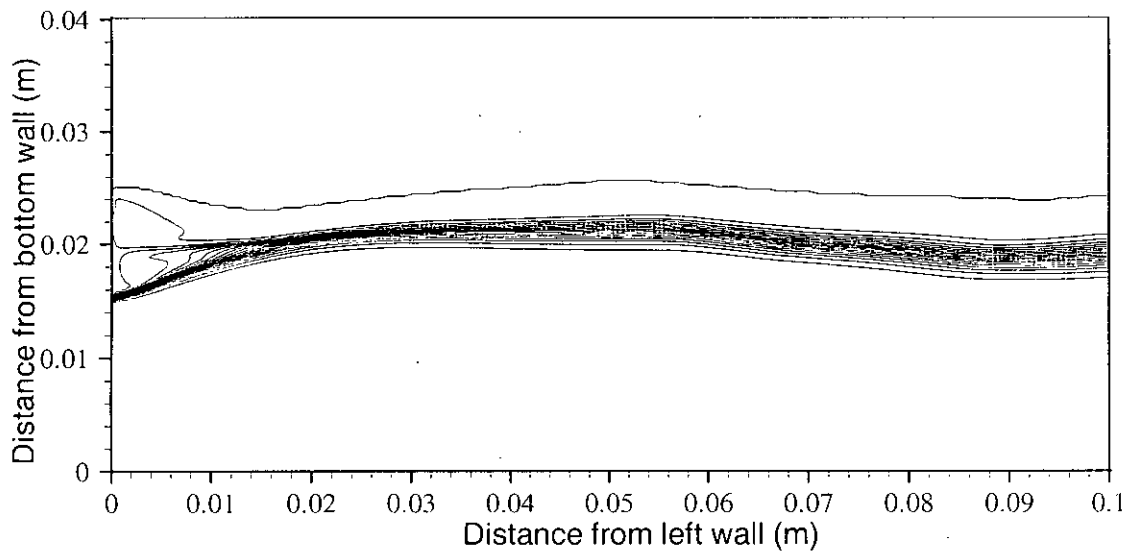


Fig. 3.5 (c) Mole fraction contour of hydrogen, ϕ (0.05,1.0,0.05); Case-3 ($\alpha = 30^\circ$).

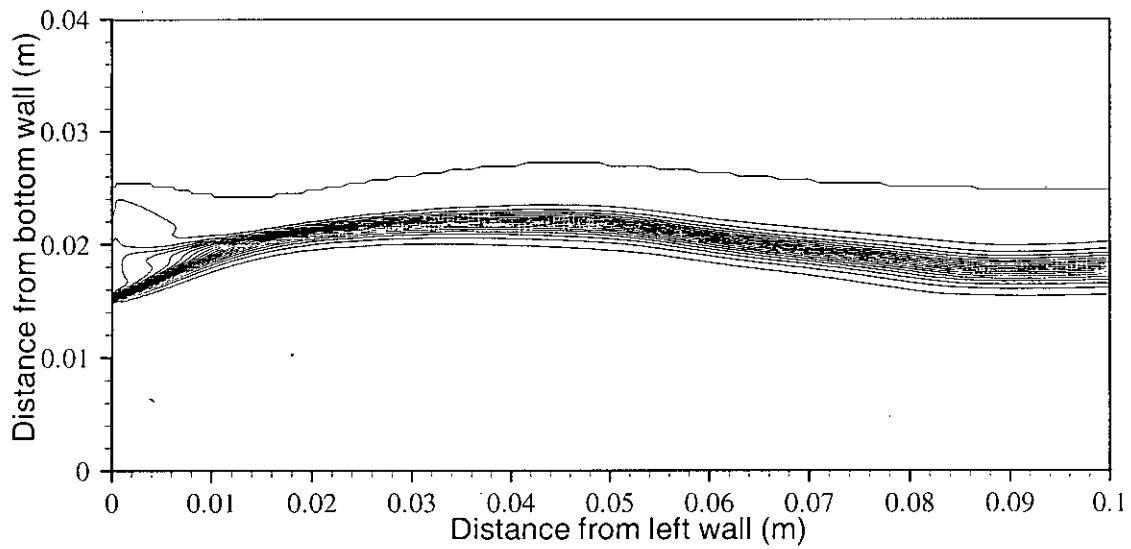


Fig. 3.5 (d) Mole fraction contour of hydrogen, ϕ (0.05,1.0,0.05); Case-4 ($\alpha = 40^\circ$).

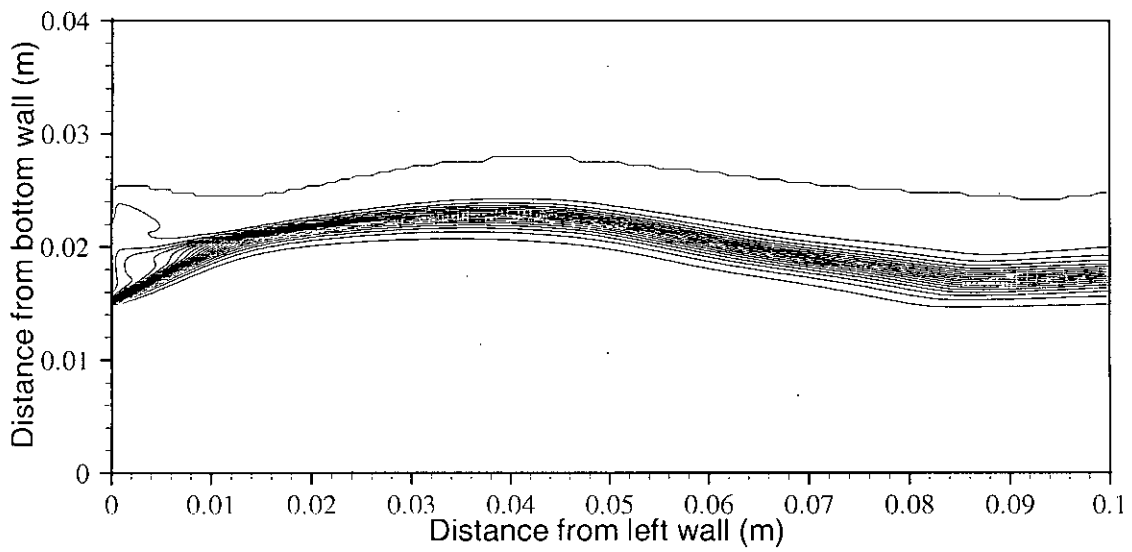


Fig. 3.5 (e) Mole fraction contour of hydrogen, ϕ (0.05,1.0,0.05): Case-5 ($\alpha = 50^\circ$).

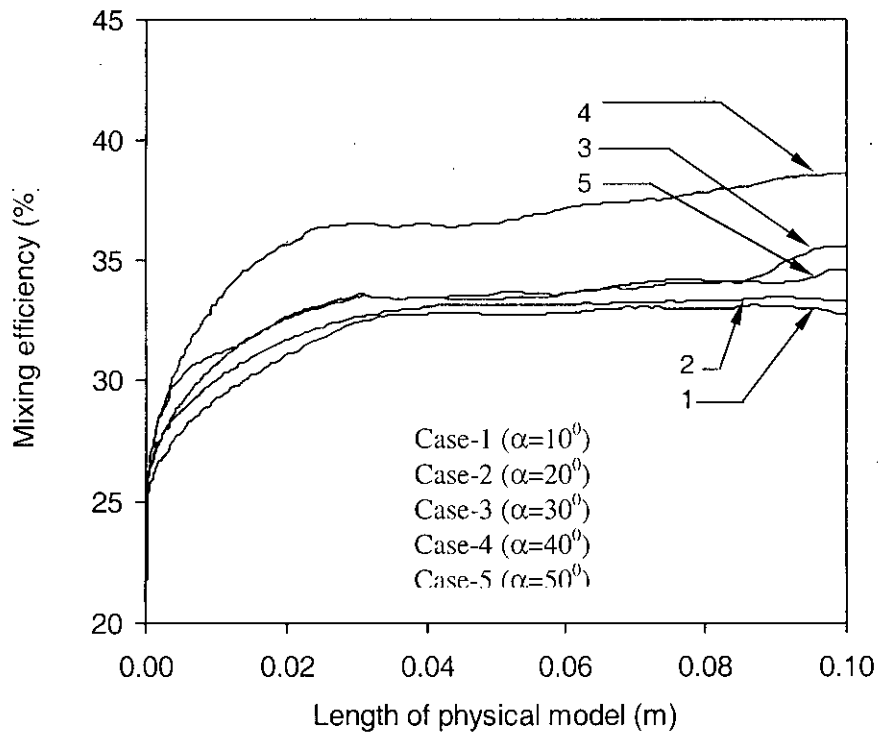


Fig. 3.6 (a) Mixing efficiency along the length of physical model.

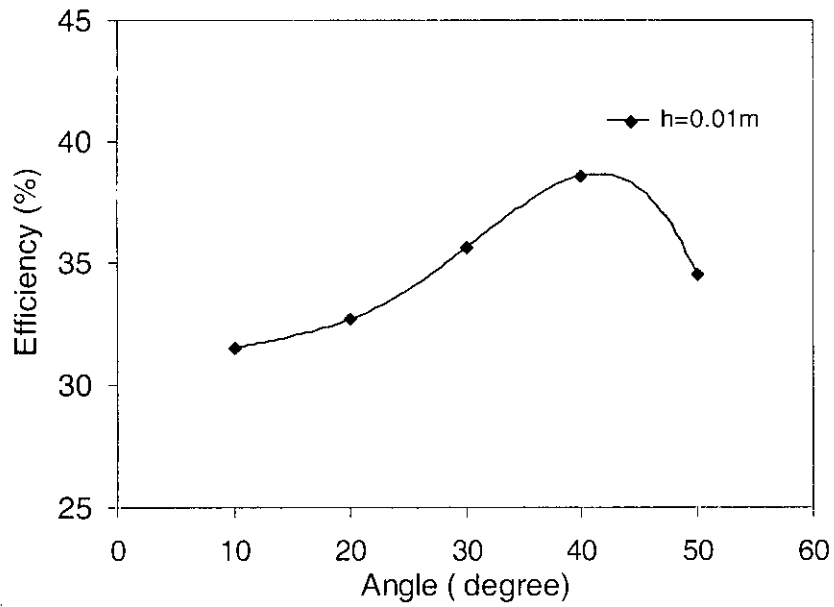


Fig. 3.6 (b) Mixing efficiency vs. merging angle; base thickness, $h=0.01\text{ m}$ ($\alpha=10^0, 20^0, 30^0, 40^0$ & 50^0)

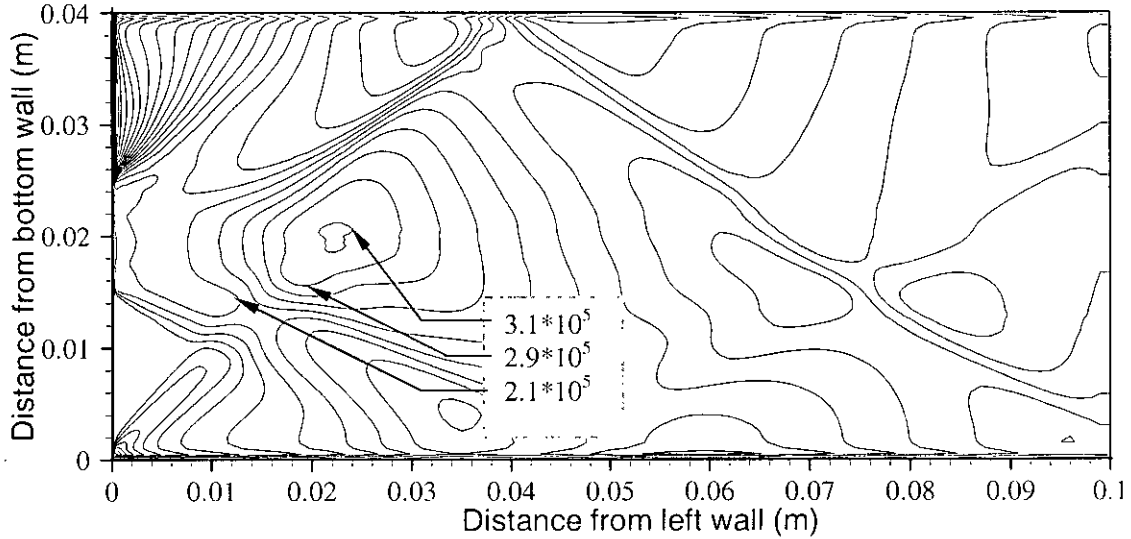


Fig 3.7 (a) Pressure (Pa) contour, $\varphi (5 \times 10^4, 7.9 \times 10^5, 2 \times 10^4)$; Case-1 ($\alpha = 10^0$).

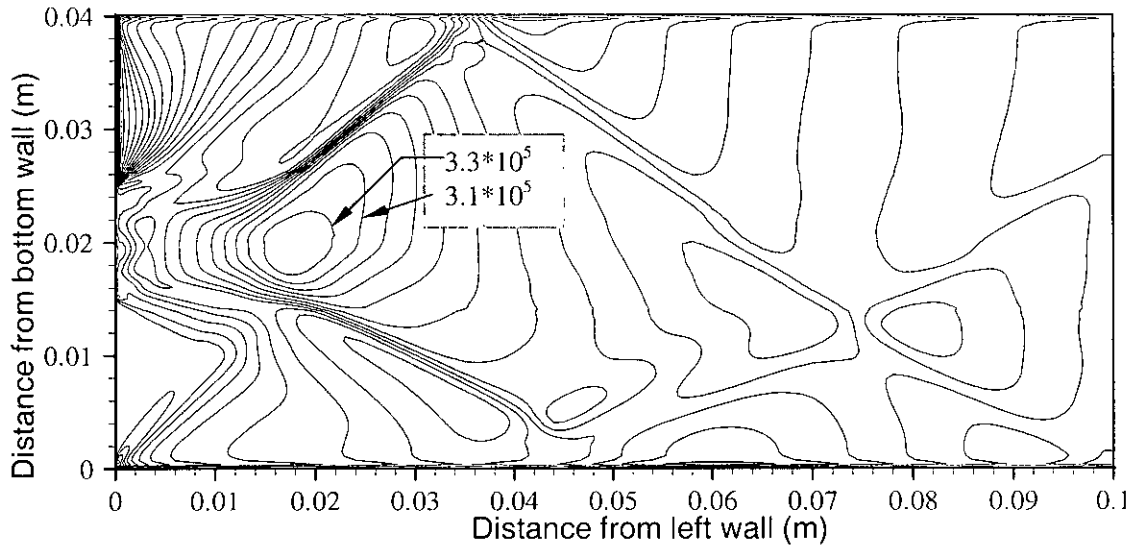


Fig 3.7 (b) Pressure (Pa) contour, $\phi (5*10^4, 7.9*10^5, 2*10^4)$; Case-2 ($\alpha = 20^\circ$).

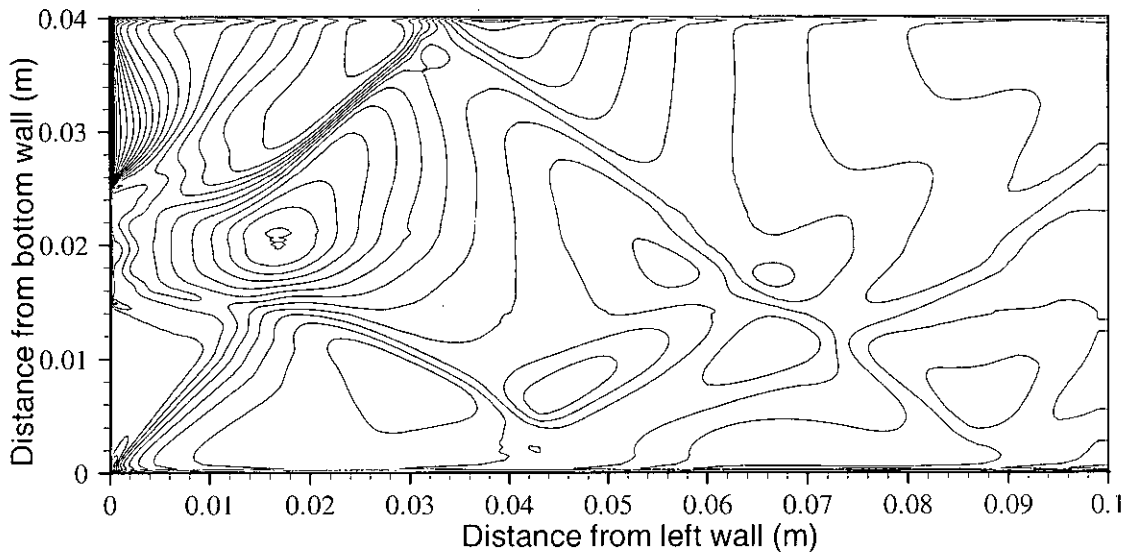


Fig 3.7 (c) Pressure (Pa) contour, $\phi (5*10^4, 7.9*10^5, 2*10^4)$; Case-3 ($\alpha = 30^\circ$).

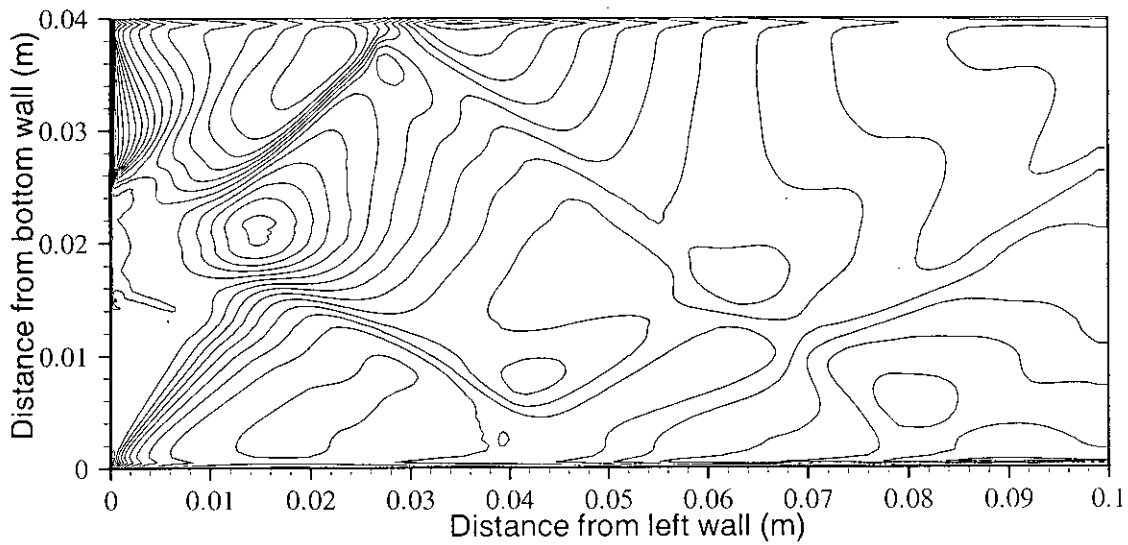


Fig 3.7 (d) Pressure (Pa) contour, $\varphi (5 \cdot 10^4, 7.9 \cdot 10^5, 2 \cdot 10^4)$; Case-4 ($\alpha = 40^\circ$).

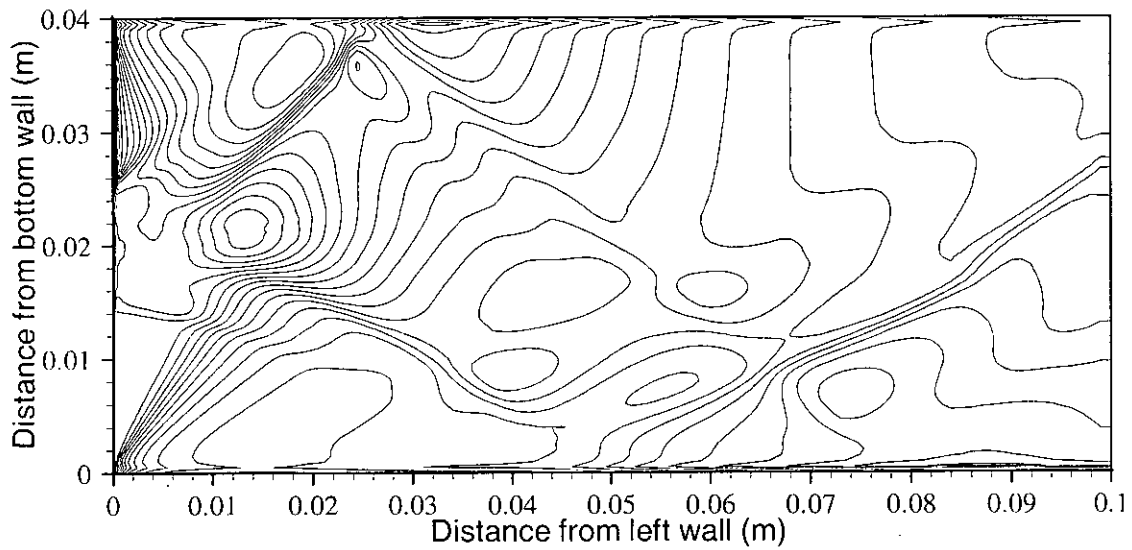


Fig 3.7 (e) Pressure (Pa) contour, $\varphi (5 \cdot 10^4, 7.9 \cdot 10^5, 2 \cdot 10^4)$; Case-5 ($\alpha = 50^\circ$).

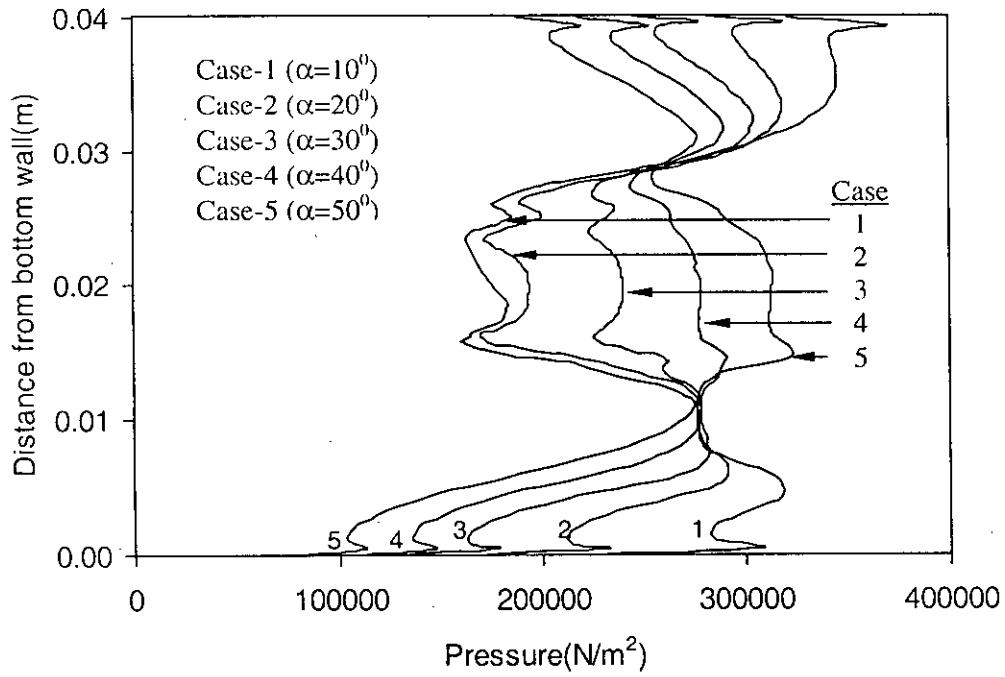


Fig. 3.8 (a) Pressure distribution at 0.005 m from left wall; Cases (1~5).

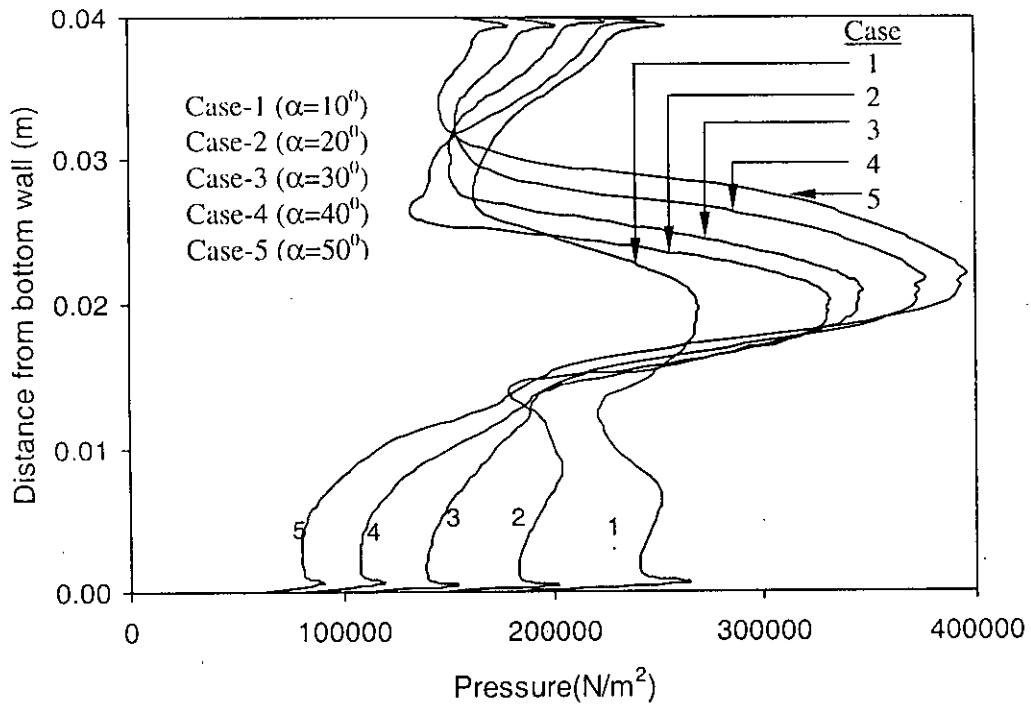


Fig. 3.8 (b) Pressure distribution at 0.015 m from left wall; Cases (1~5).

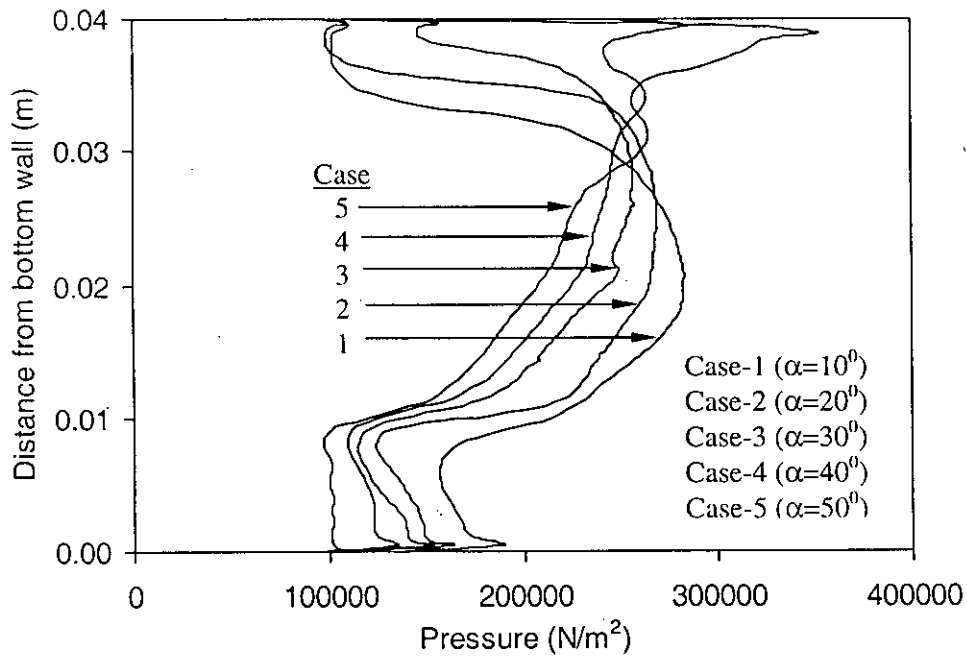


Fig. 3.8 (c) Pressure distribution at 0.03 m from left wall; Cases (1~5).

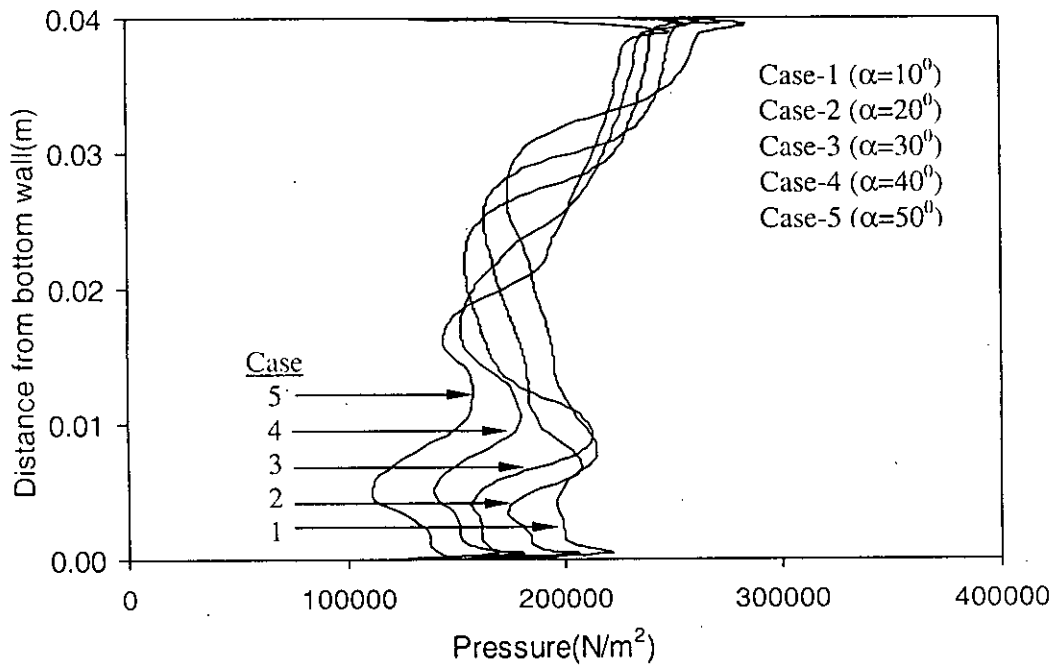


Fig. 3.8 (d) Pressure distribution at 0.05 m from left wall; Cases (1~5).

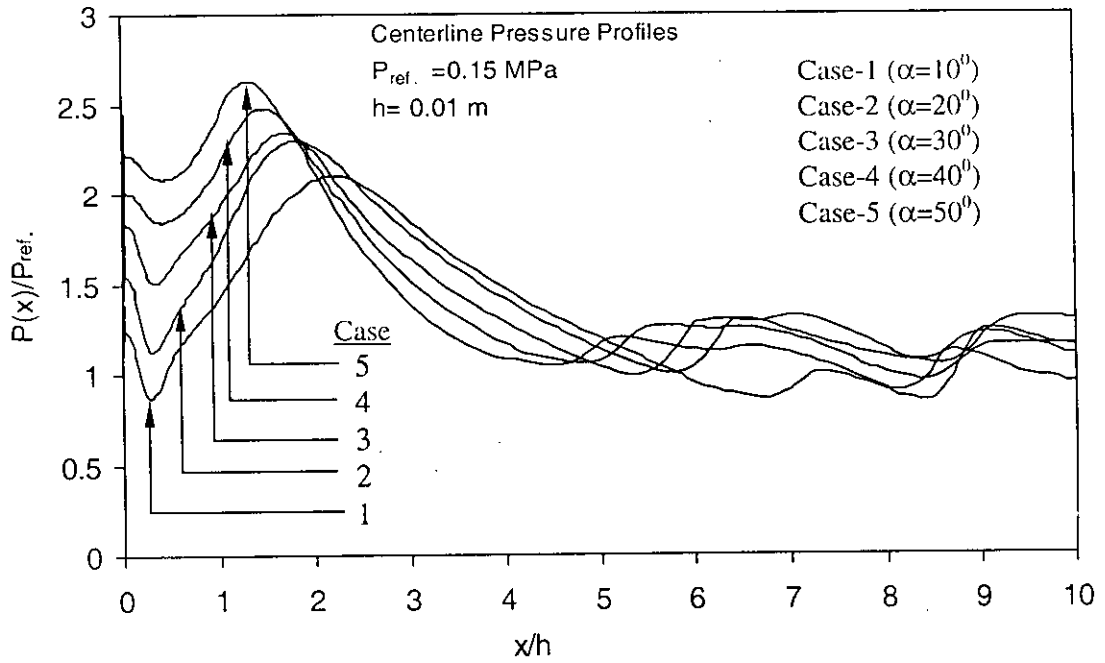


Fig. 3.9 Centerline pressure profiles of the flowfield.

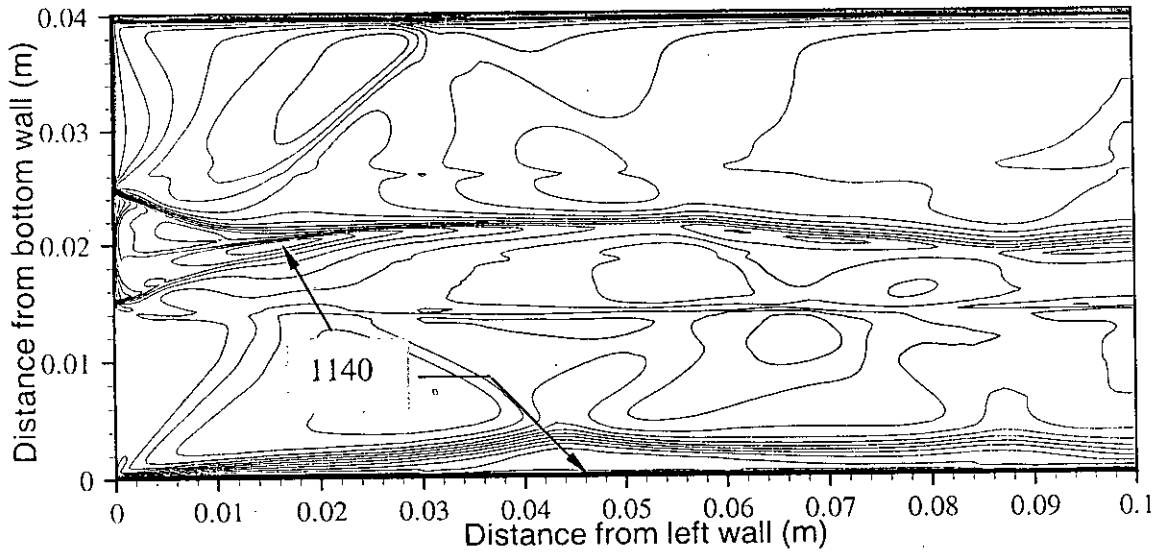


Fig. 3.10 (a) Temperature (K) contour, ϕ (500, 1220, 40); Case-1 ($\alpha = 10^\circ$).

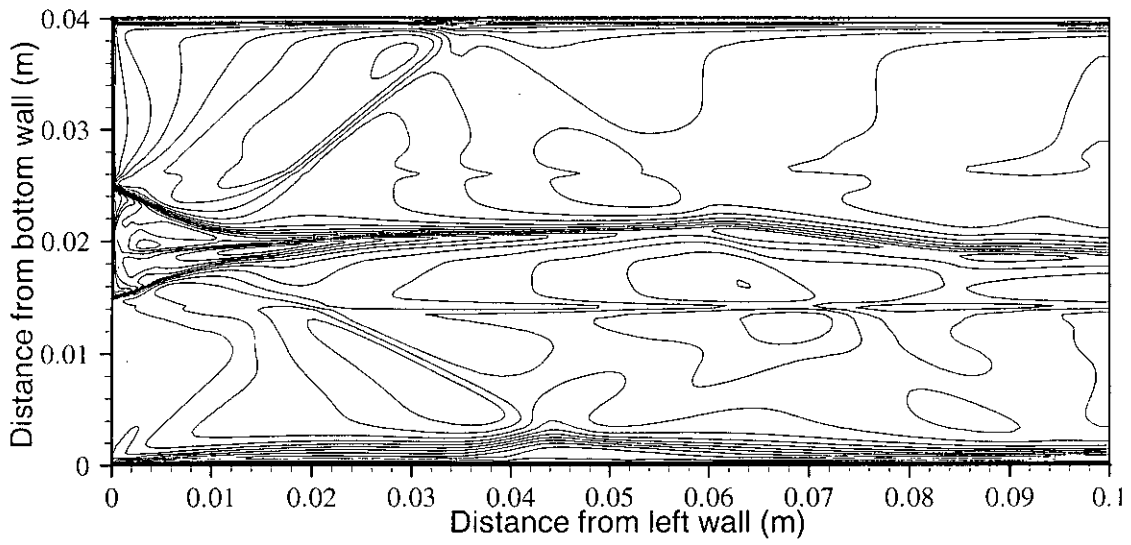


Fig. 3.10 (b) Temperature (K) contour, ϕ (500, 1220, 40); Case-2 ($\alpha = 20^\circ$).

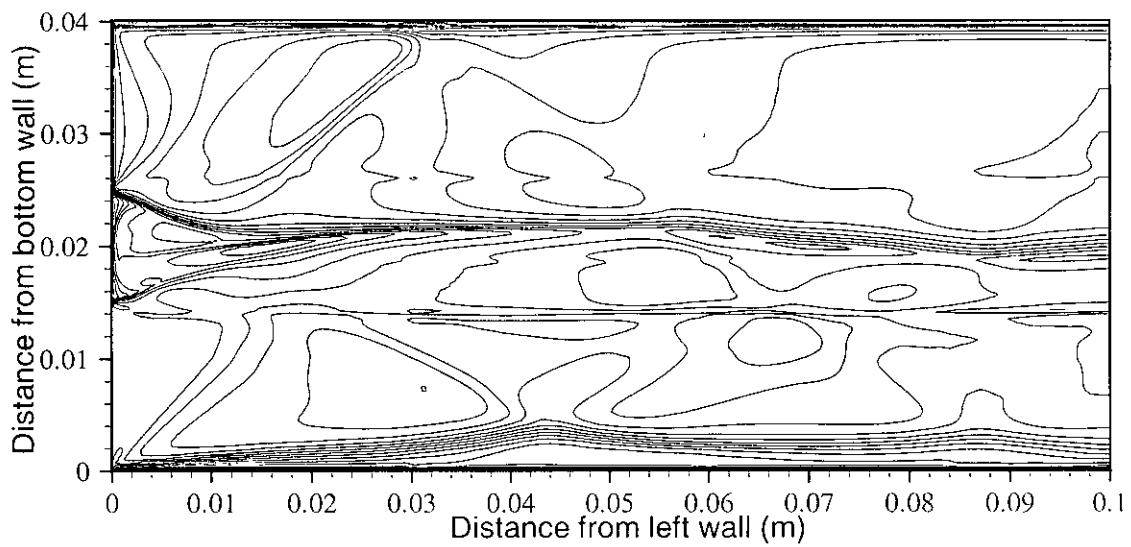


Fig. 3.10 (c) Temperature (K) contour, ϕ (500, 1220, 40); Case-3 ($\alpha = 30^\circ$).

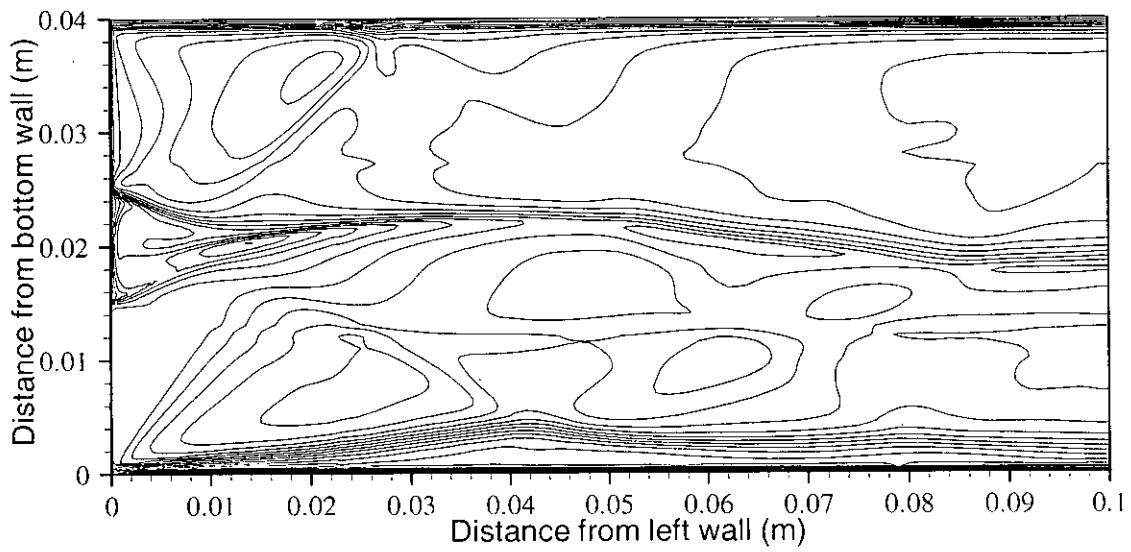


Fig. 3.10 (d) Temperature (K) contour, ϕ (500, 1220, 40); Case-4 ($\alpha = 40^\circ$).

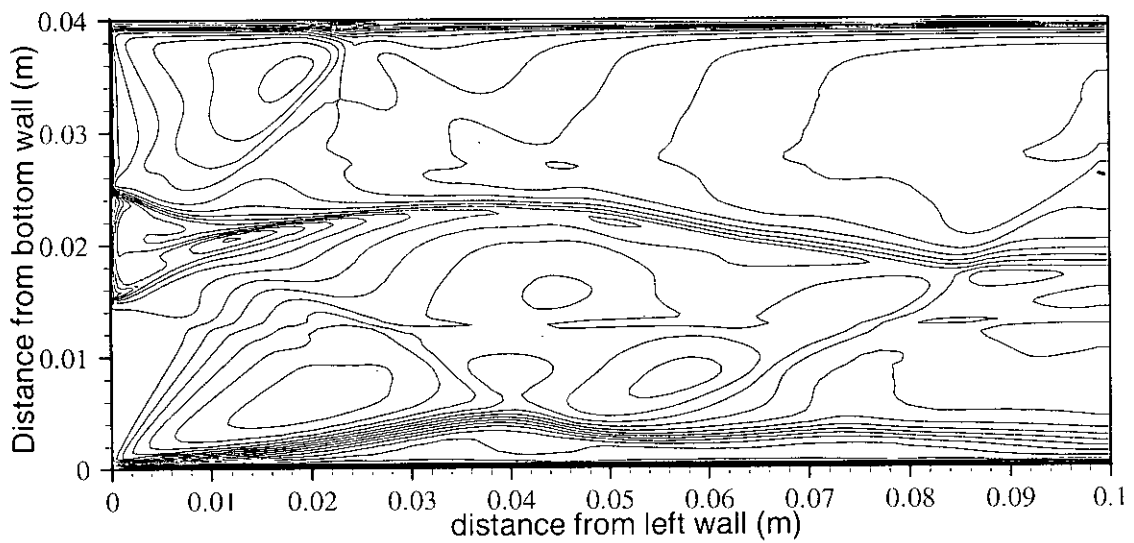


Fig. 3.10 (e) Temperature (K) contour, ϕ (500, 1220, 40); Case-5 ($\alpha = 50^\circ$).

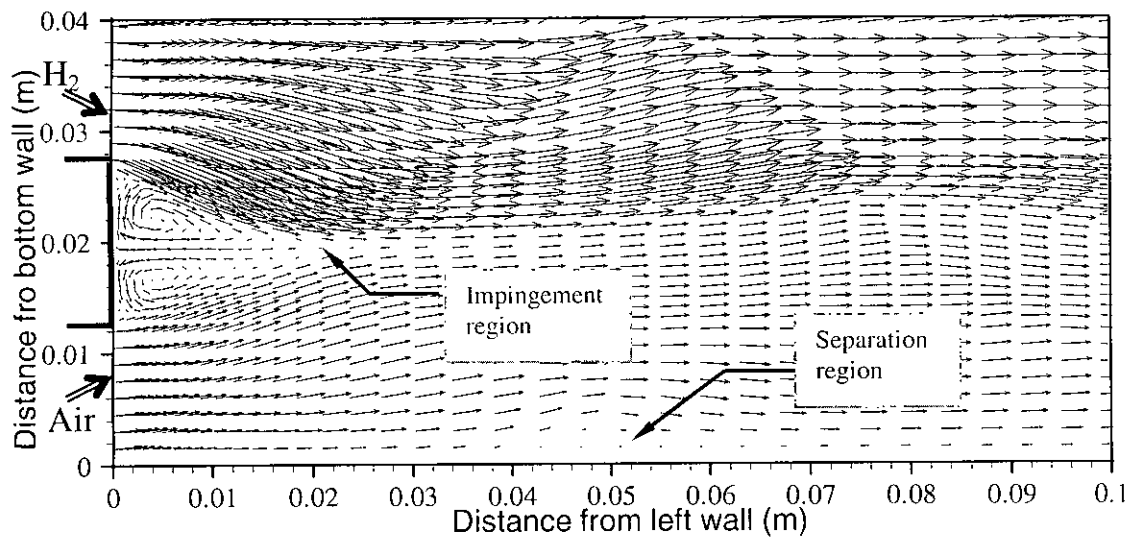


Fig. 3.11 (a) Velocity vector field of two streams; Case-6 ($\alpha = 10^\circ$).

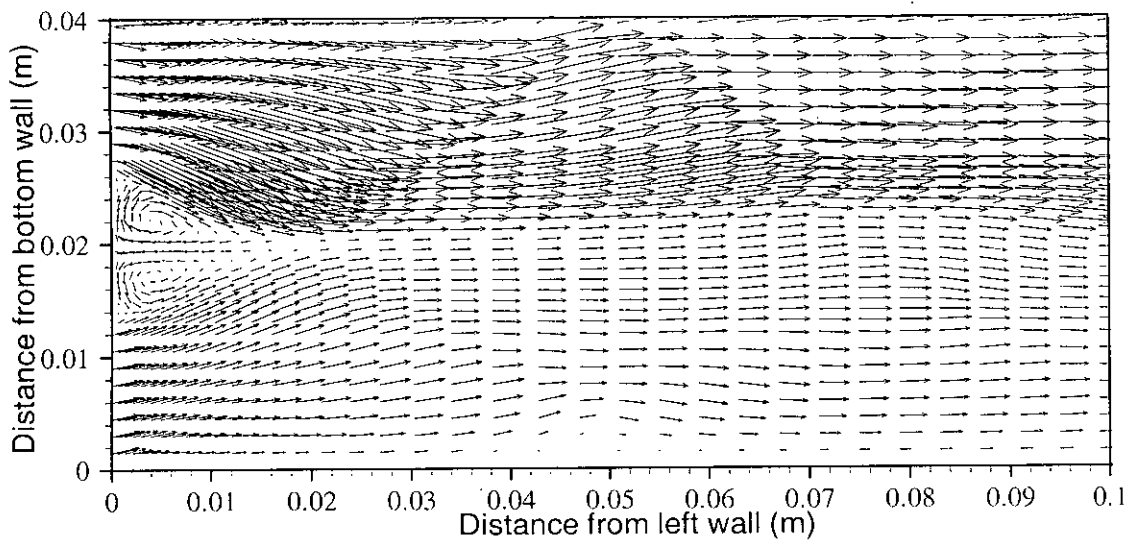


Fig. 3.11 (b) Velocity vector field of two streams; Case-7 ($\alpha = 20^\circ$).

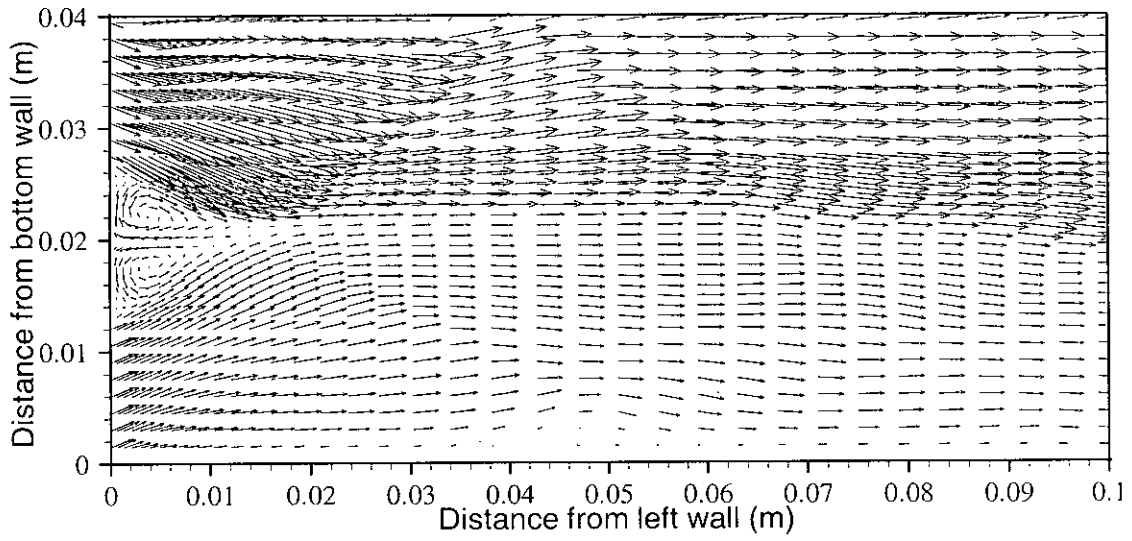


Fig. 3.11 (c) Velocity vector field of two streams; Case-8 ($\alpha = 40^\circ$).

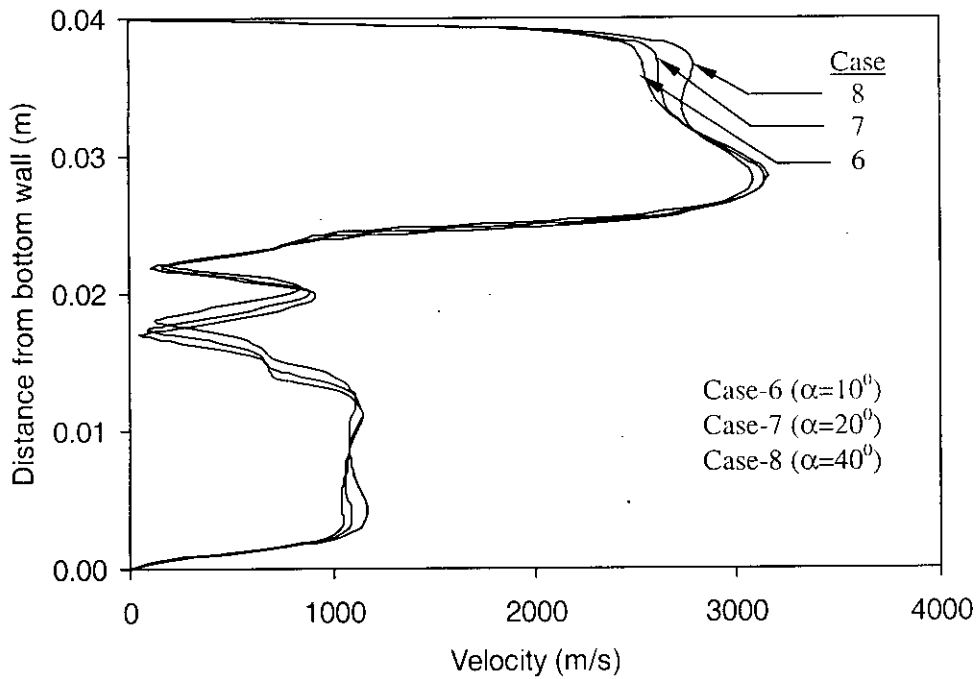


Fig. 3.12 (a) Velocity profiles at 0.005m from left wall; Case (6~8).

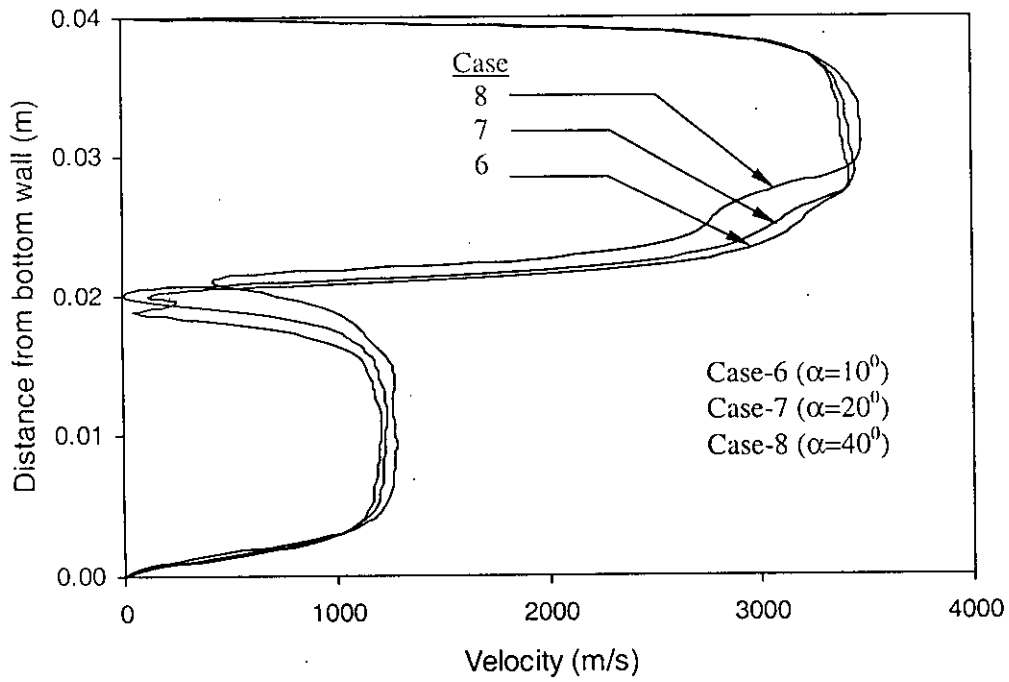


Fig. 3.12 (b) Velocity profiles at 0.019 m from left wall; Case (6~8).

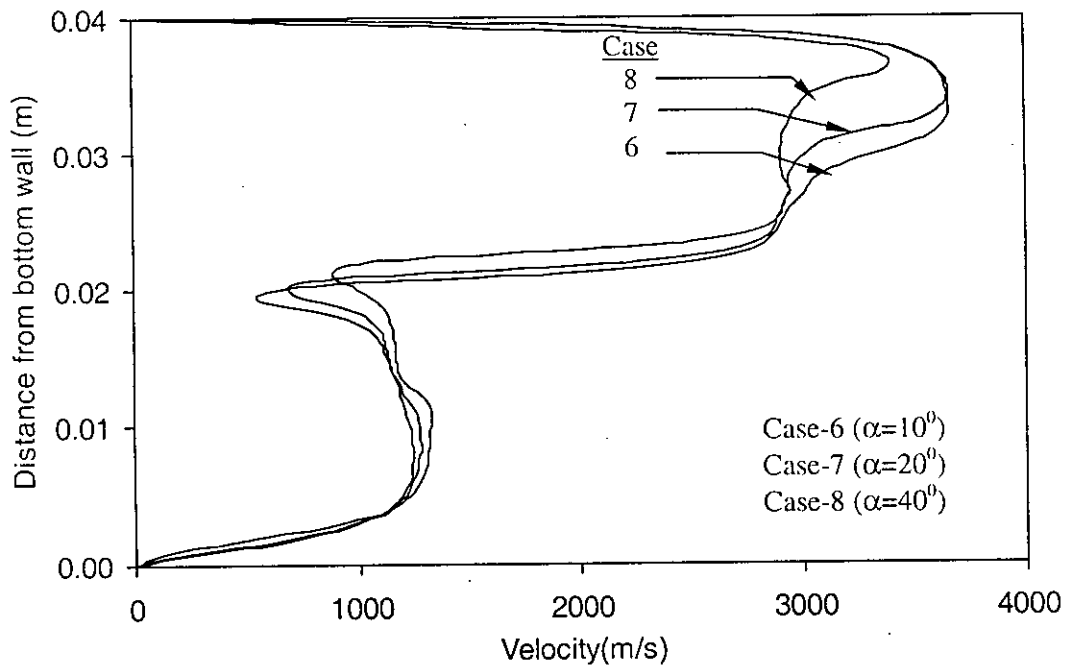


Fig. 3.12 (c) Velocity profiles at 0.03 m from left wall; Case (6~8).

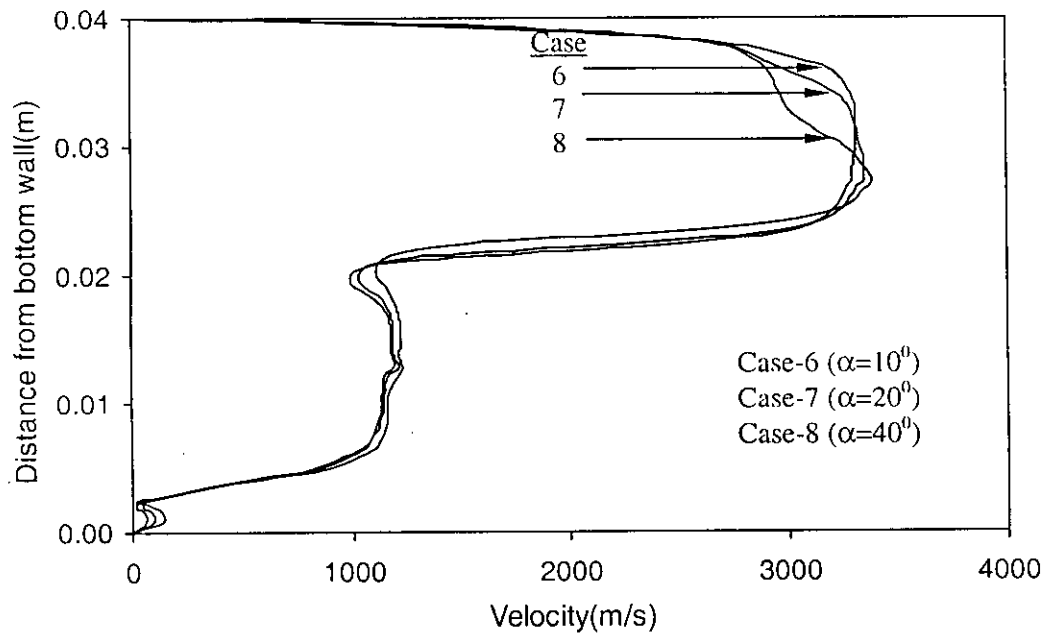


Fig. 3.12 (d) Velocity profiles at 0.05 m from left wall; Case (6~8).

Lengthwise Velocity Profile u/u_1
 Velocity of Hydrogen $u_1=1530$ m/s
 Velocity of Air $u_2=1121$ m/s

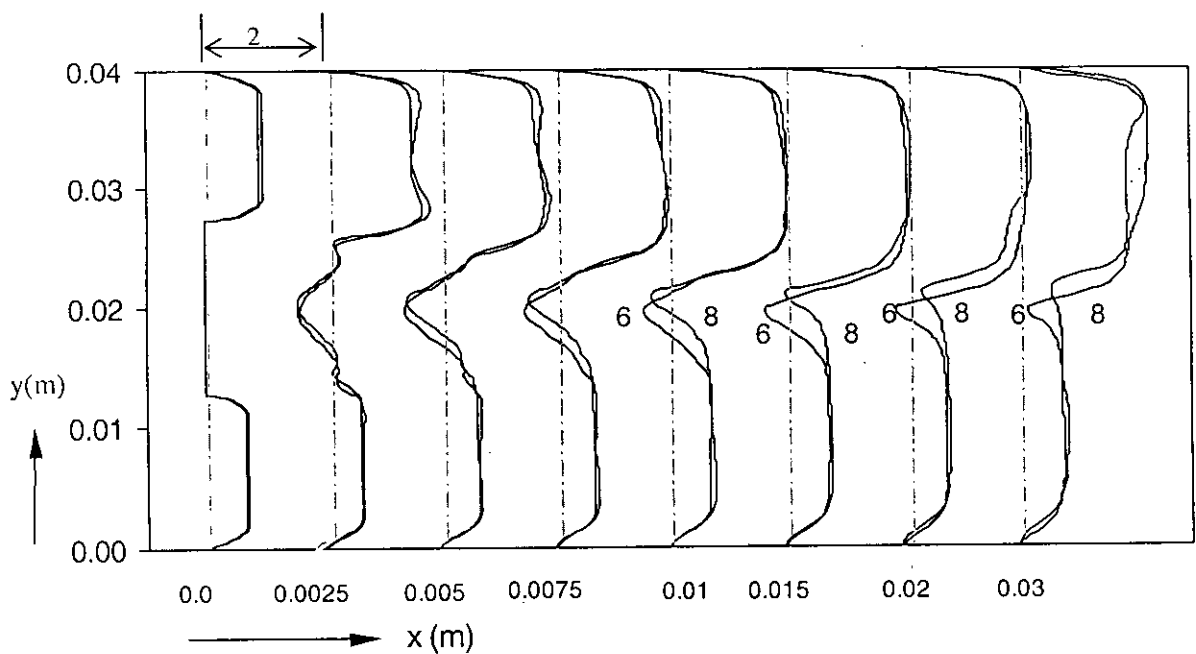


Fig 3.13 (a) Lengthwise velocity profiles for the two-stream interaction flowfield showing the near-wake region;(case-6 & 8).

100839

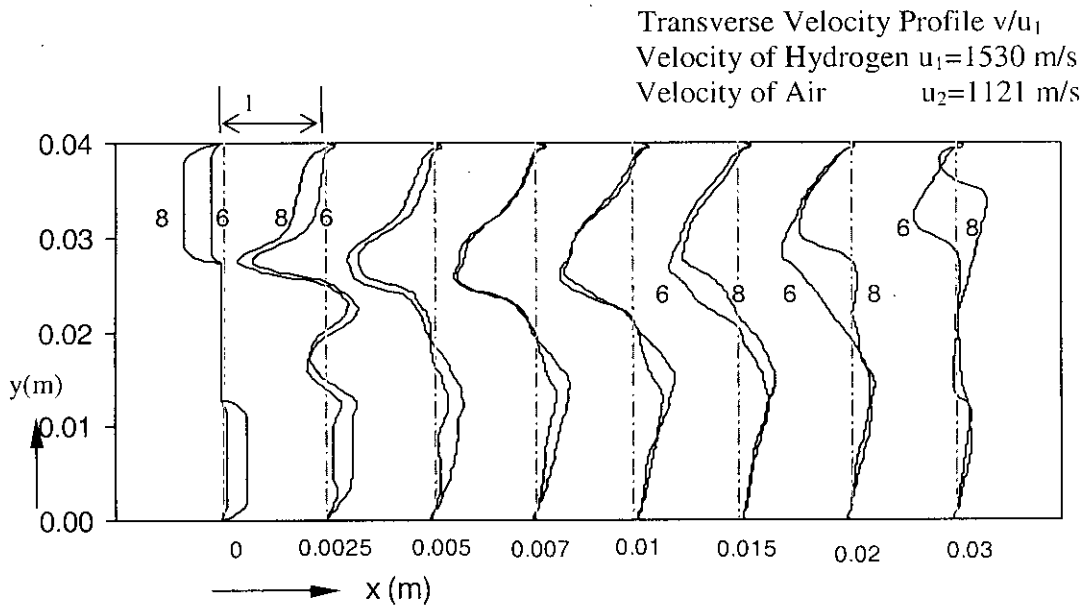


Fig 3.13 (b) Transverse velocity profiles for the two-stream interaction flowfield showing the near-wake region. (Case-6 & 8).

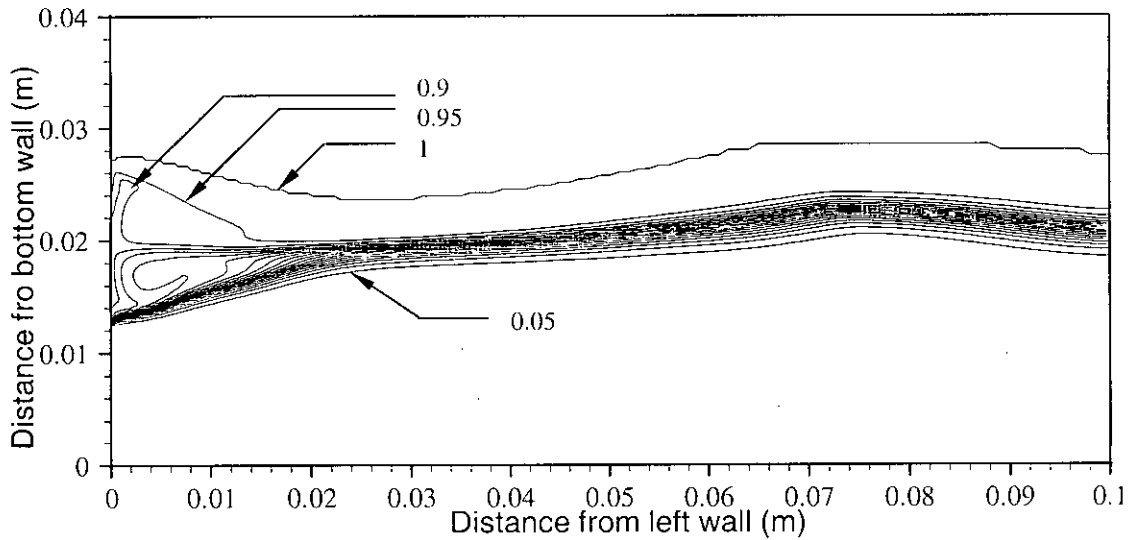


Fig. 3.14 (a) Mole fraction contour of hydrogen, ϕ (0.05,1.0,0.05); Case-6 ($\alpha = 10^0$).

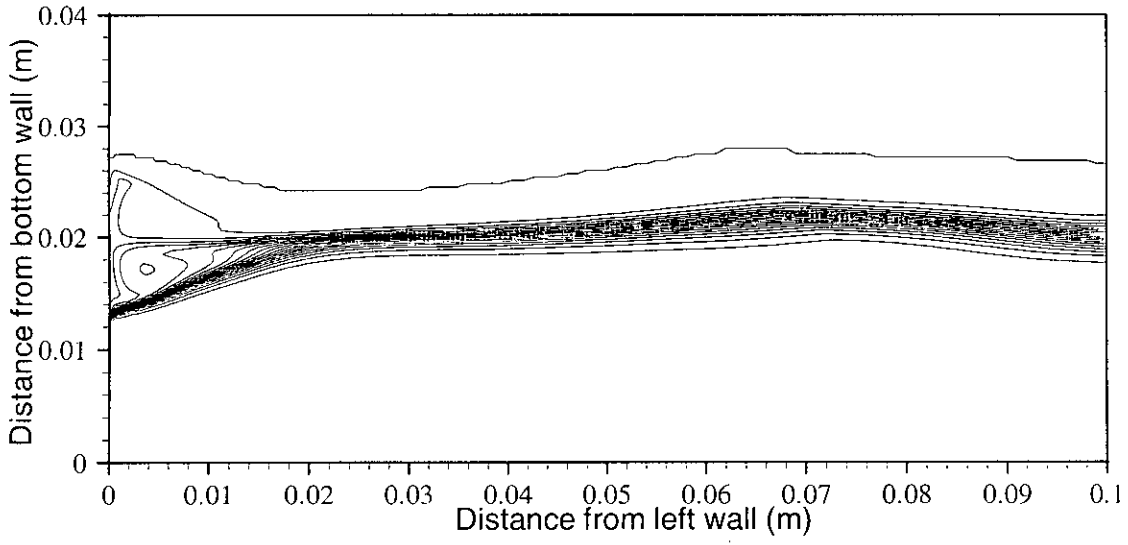


Fig. 3.14 (b) Mole fraction contour of hydrogen, ϕ (0.05,1.0,0.05); Case-7 ($\alpha = 20^\circ$).

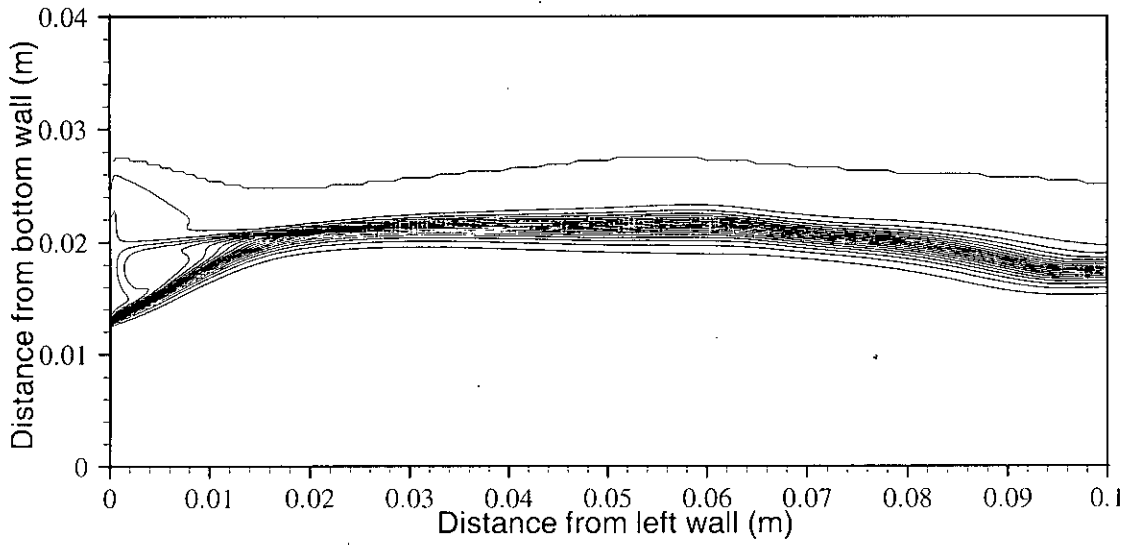


Fig. 3.14 (c) Mole fraction contour of hydrogen, ϕ (0.05,1.0,0.05); Case-8 ($\alpha = 10^\circ$).

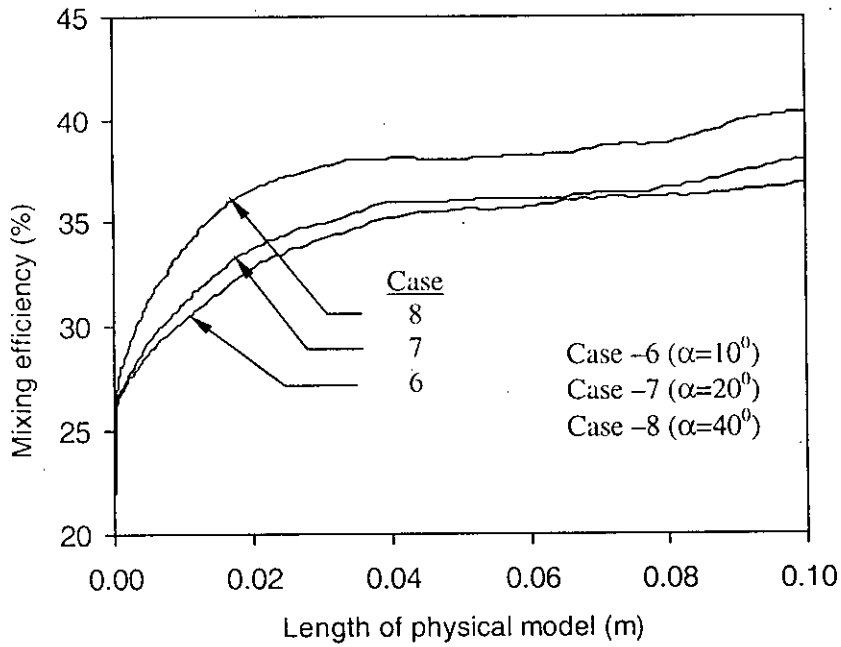


Fig. 3.15 (a) Mixing efficiency along the length of physical model.

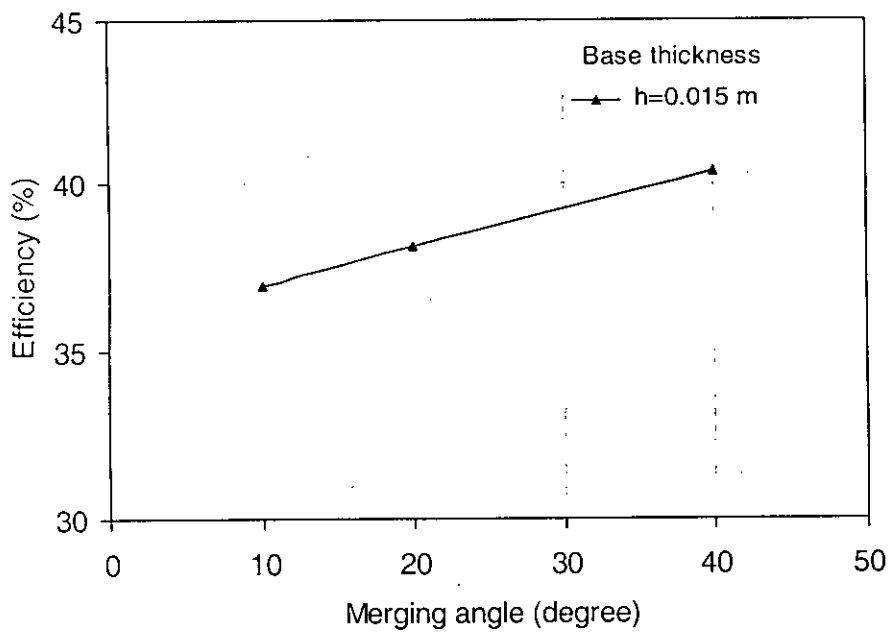


Fig. 3.15 (b) Mixing efficiency vs. Merging angle; base thickness, $h = 0.015$ m ($\alpha = 10^\circ, 20^\circ$ & 40°).

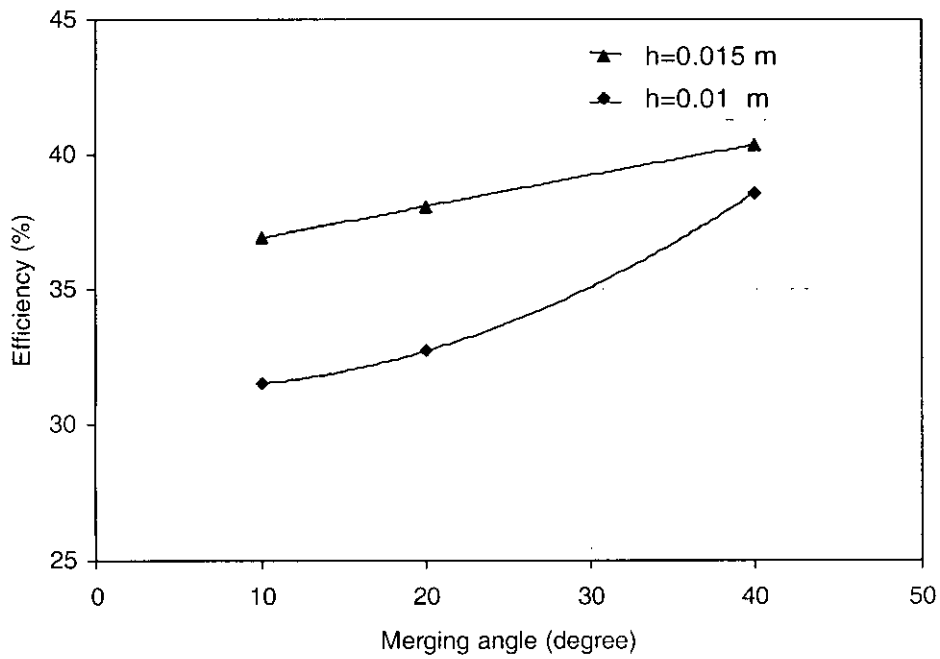


Fig. 3.15 (c) Comparison of mixing efficiency between $h = 0.01$ and $h = 0.015$ m base thickness; (for $\alpha = 10^\circ, 20^\circ$ & 40°).

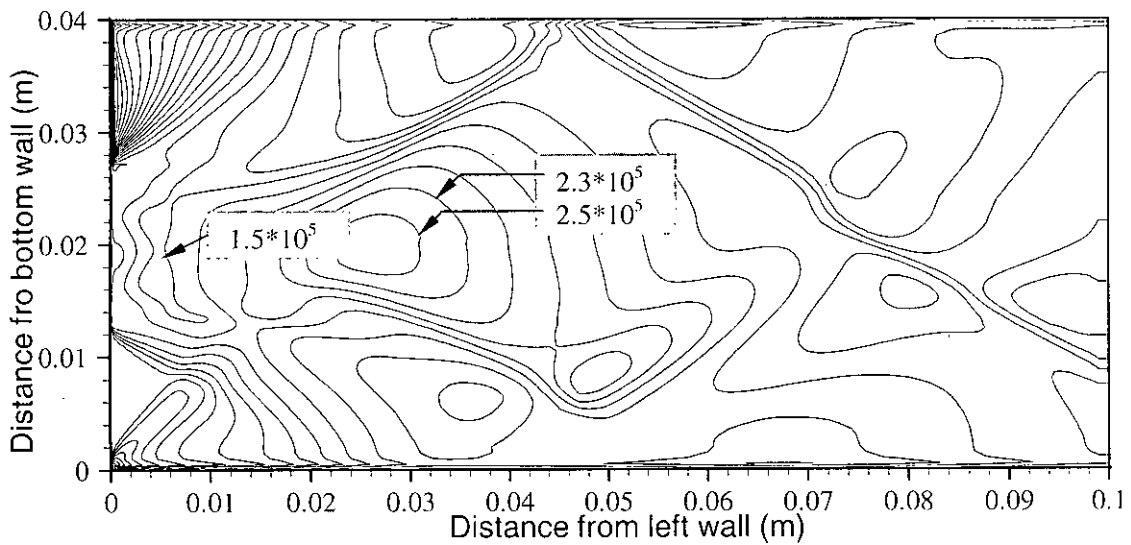


Fig 3.16 (a) Pressure (Pa) contour, $\phi (5 \cdot 10^4, 7.9 \cdot 10^5, 2 \cdot 10^4)$; Case-6 ($\alpha = 10^\circ$).

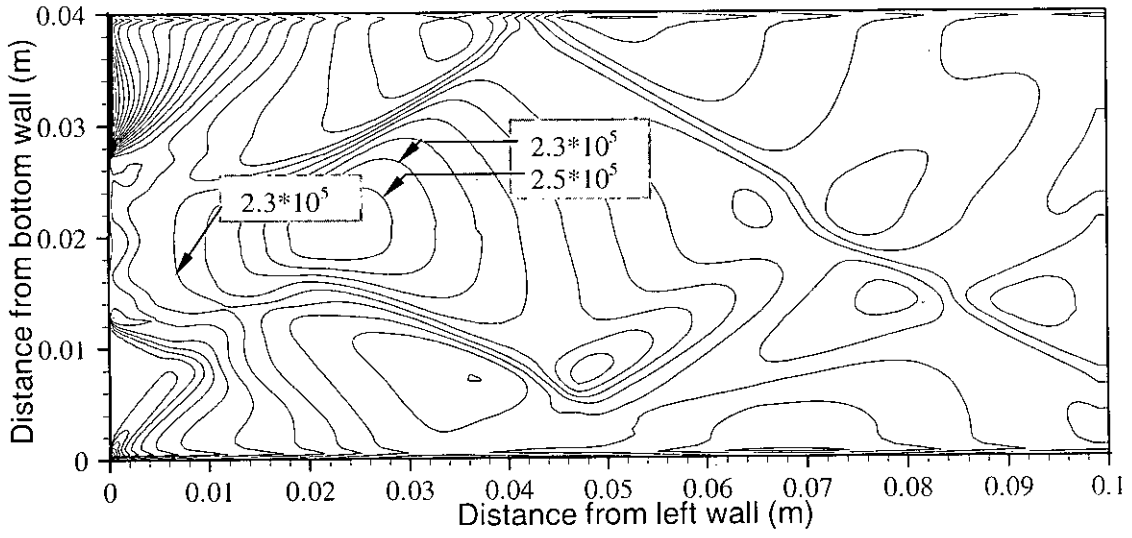


Fig 3.16 (b) Pressure (Pa) contour, $\phi (5 \cdot 10^4, 7.9 \cdot 10^5, 2 \cdot 10^4)$; Case-7 ($\alpha = 20^\circ$).

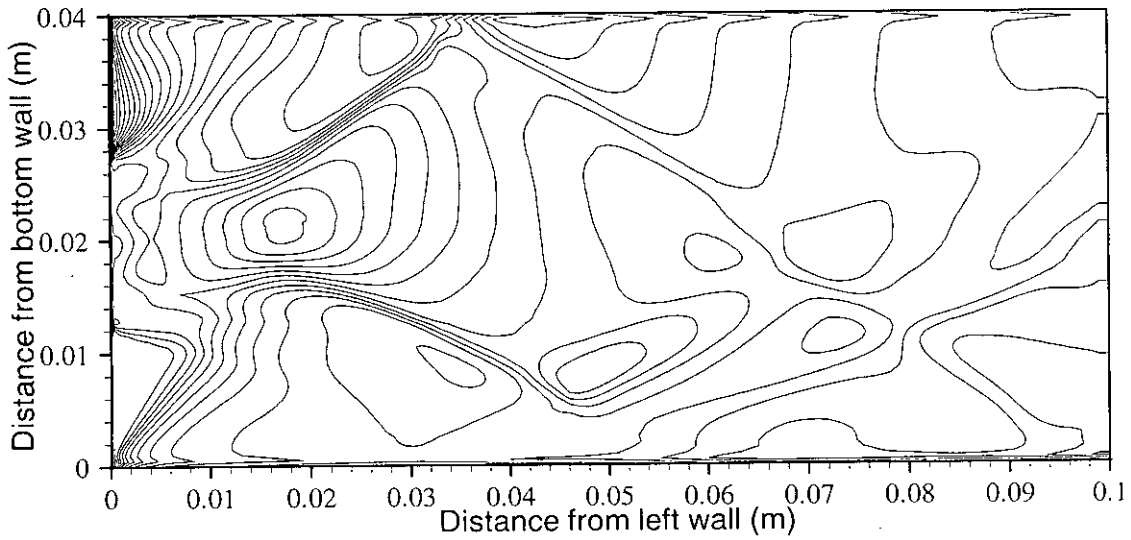


Fig 3.16 (c) Pressure (Pa) contour, $\phi (5 \cdot 10^4, 7.9 \cdot 10^5, 2 \cdot 10^4)$; Case-8 ($\alpha = 40^\circ$).

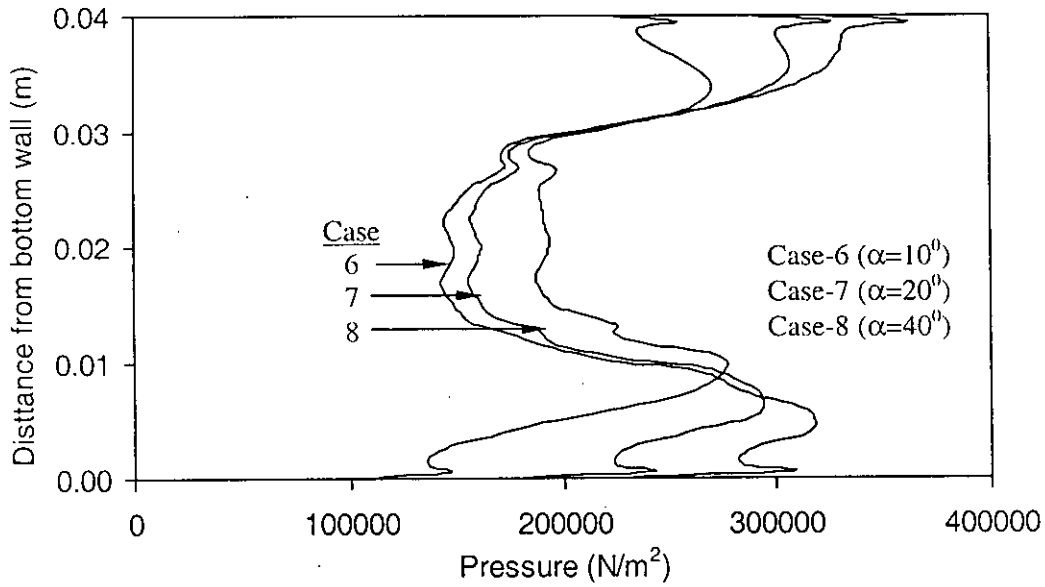


Fig. 3.17 (a) Pressure distribution at 0.005 m from left wall; Cases (6~8).

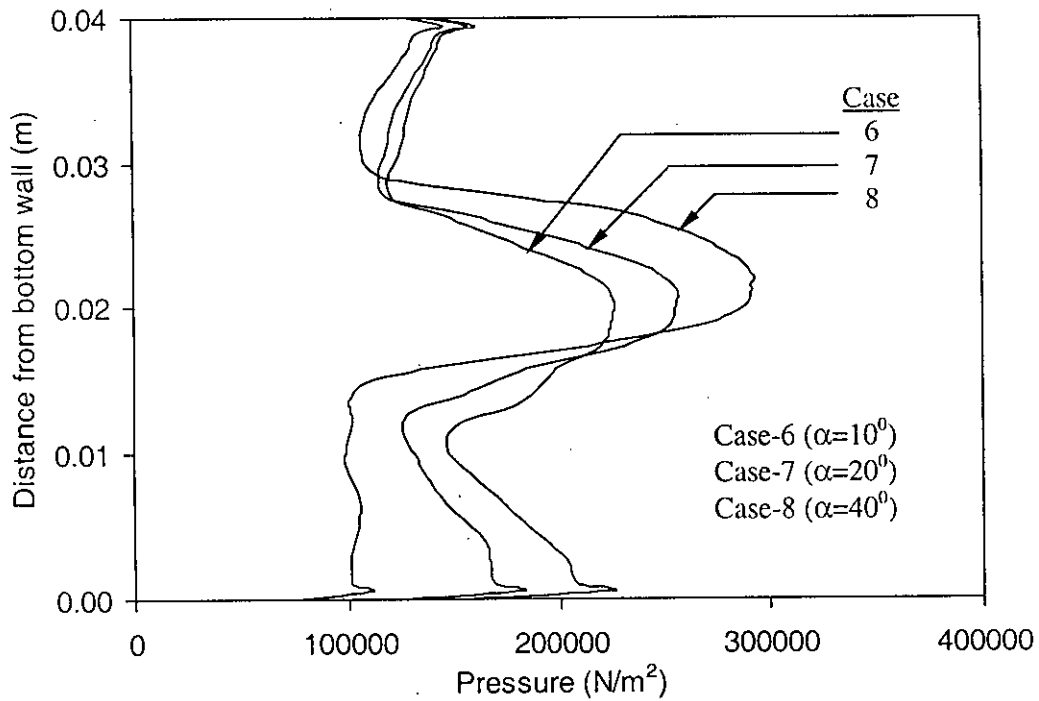


Fig. 3.17 (b) Pressure distribution at 0.019 m from left wall; Cases (6~8).

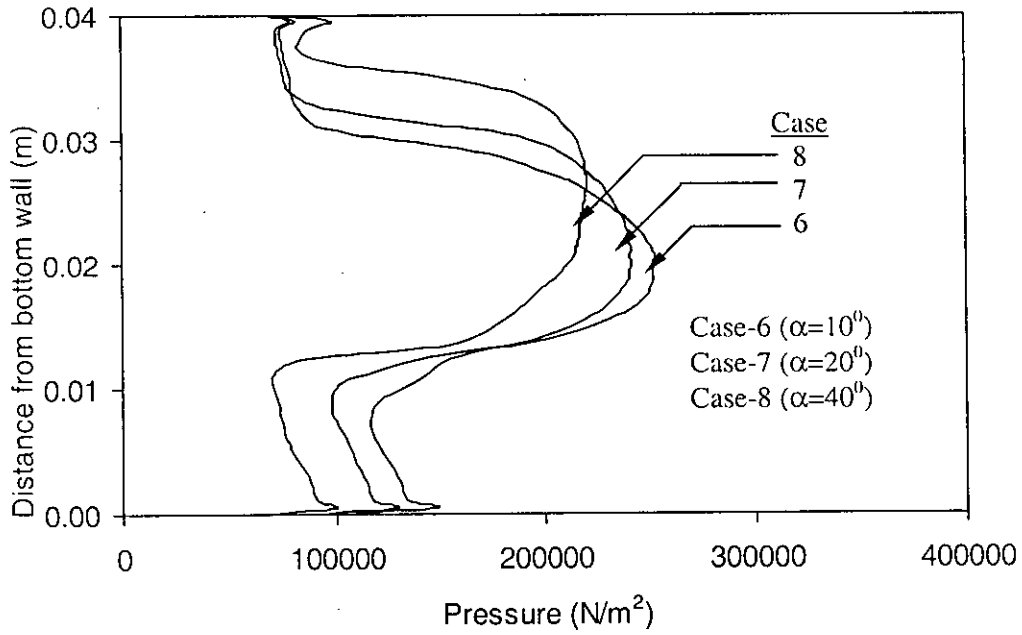


Fig. 3.17 (c) Pressure distribution at 0.03 m from left wall; Cases (6~8).

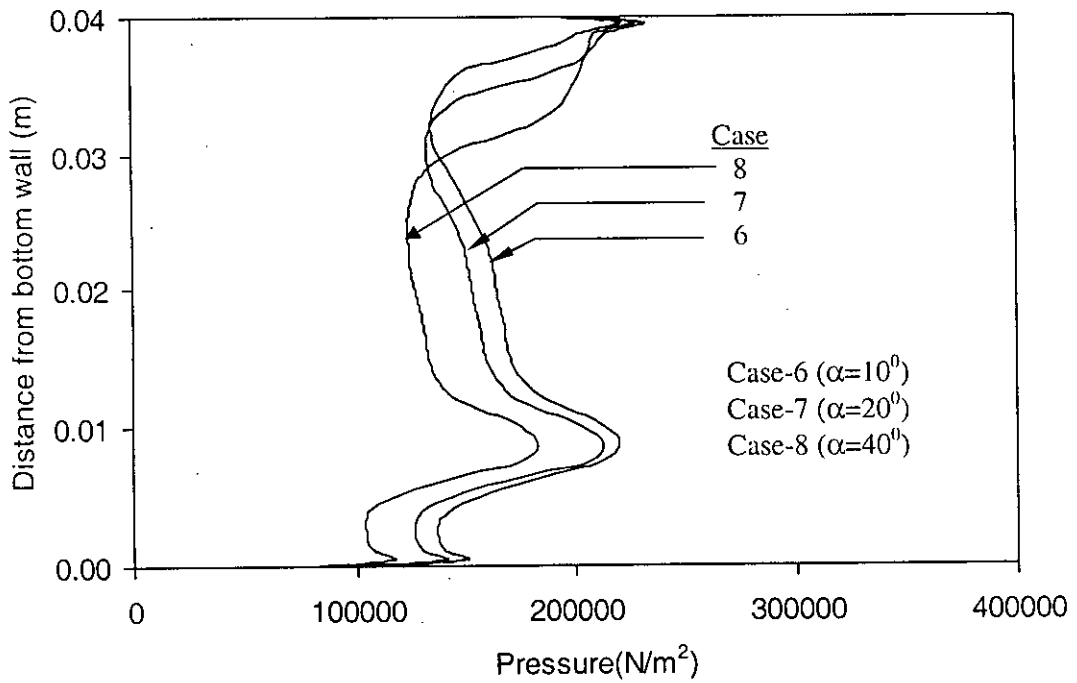


Fig. 3.17 (d) Pressure distribution at 0.05 m from left wall; Cases (6~8).

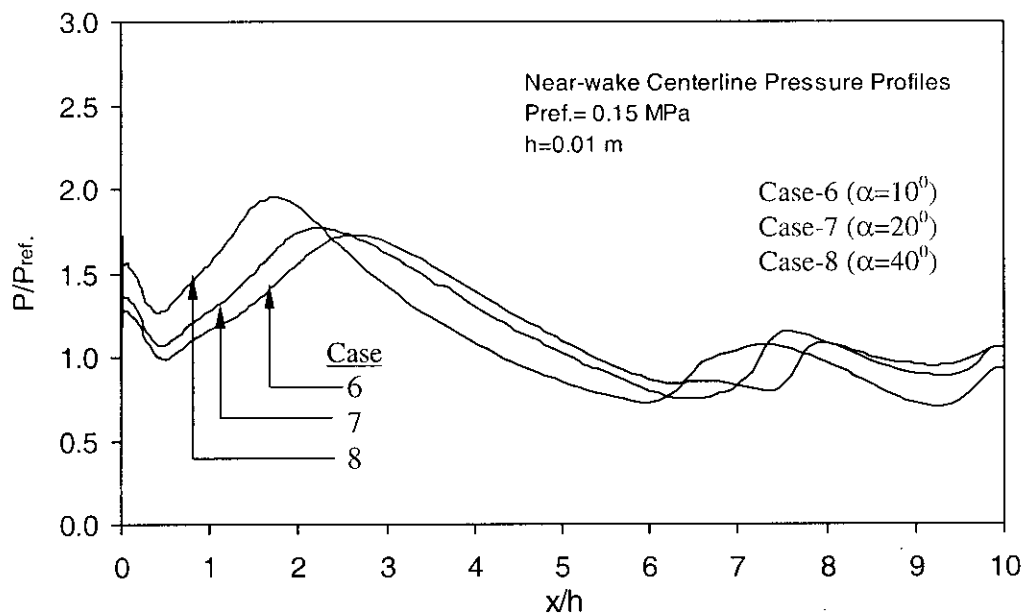


Fig.3.18 Centerline pressure profiles of the flow field; Cases (6-8).

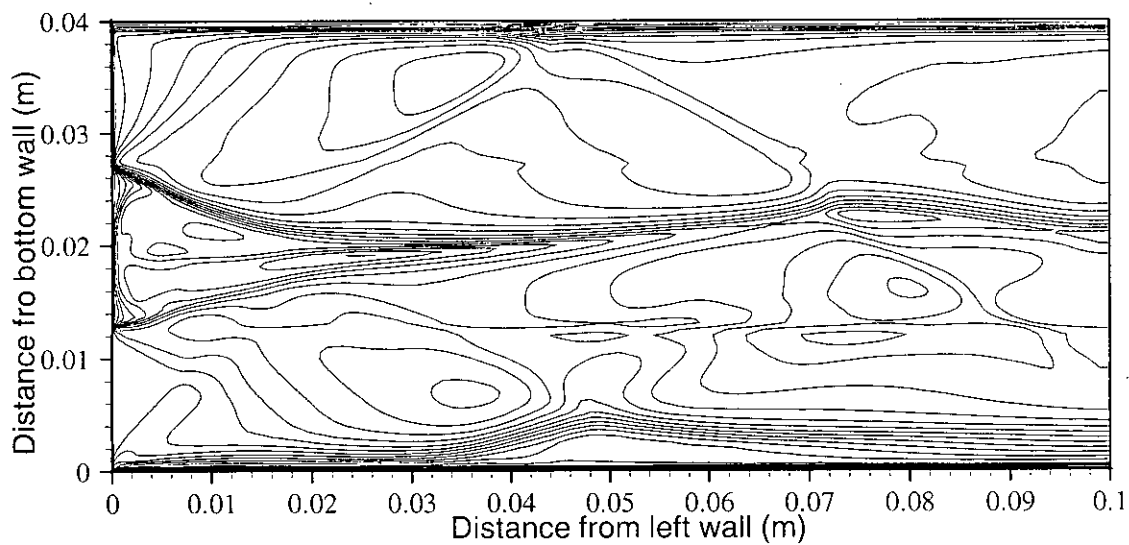


Fig. 3.19 (a) Temperature (K) contour, ϕ (500, 1220, 40); Case-6 ($\alpha = 10^\circ$).

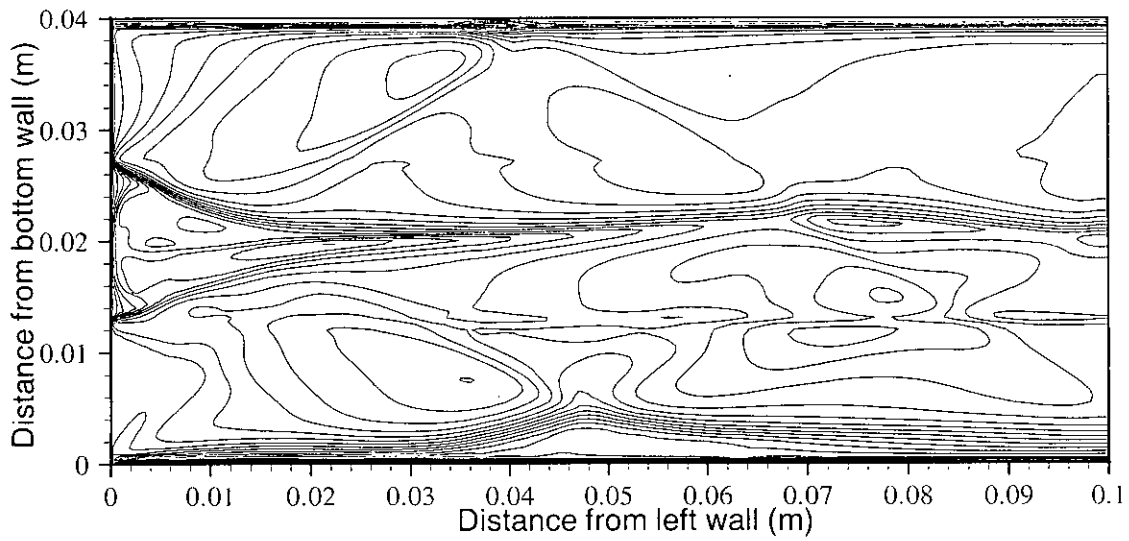


Fig. 3.19 (b) Temperature (K) contour, ϕ (500, 1220, 40); Case-7 ($\alpha = 20^\circ$).

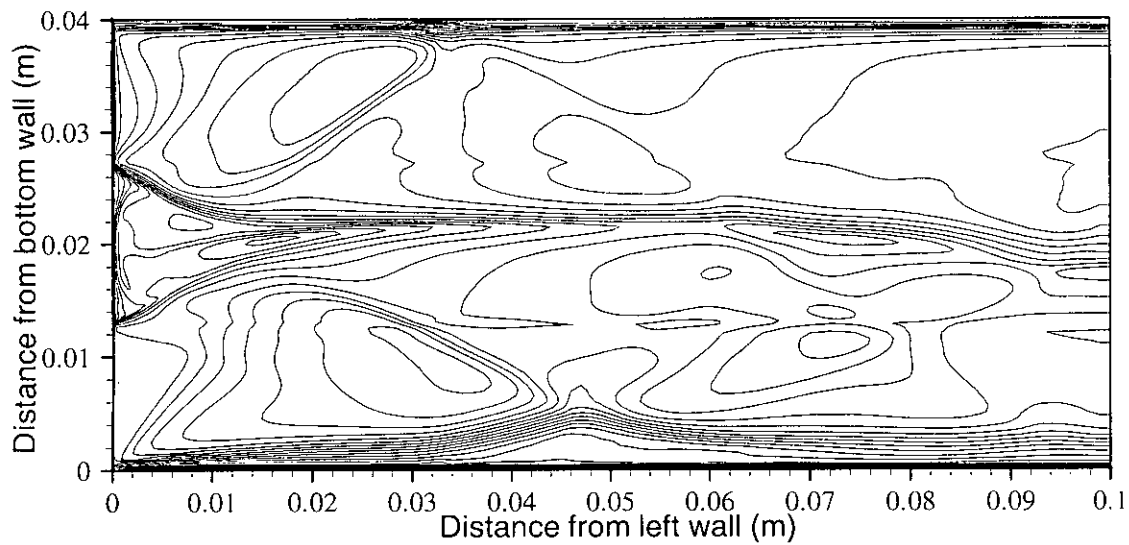


Fig. 3.19 (c) Temperature (K) contour, ϕ (500, 1220, 40); Case-8 ($\alpha = 40^\circ$).

Table 2.1 Coefficients of Thermodynamic Polynomials

Temperature range from 0~1000 K

Coefficients	H ₂	O ₂	N ₂
a ₁	0.33553514E+01	0.37837135E+01	0.37044177E+01
a ₂	0.50136144E-03	-0.30233634E-02	-0.14218753E-02
a ₃	-0.23006908E-60	0.99492751E-05	0.28670392E-05
a ₄	-0.47905324E-09	-0.98189101E-08	-0.12028885E-08
a ₅	0.48522585E-12	0.33031825E-11	-0.3954677E-13
a ₆	-0.10191626E+04	-0.10638107E+04	-0.10640795E+04
a ₇	-0.35477228E+04	0.36416345E+01	0.22336285E+01

Temperature range from 1000 ~5000K

Coefficients	H ₂	O ₂	N ₂
a ₁	0.30667095E-01	0.361221360+01	0.28532899E+01
a ₂	0.57473755E-03	0.74853166E-03	0.16022128E-02
a ₃	0.13938319E-07	-0.19820647E-6	-0.62936893E-06
a ₄	-0.25483518E-10	-0.33749008E-01	0.11441022E-09
a ₅	0.29098574E-14	-0.23907374E-14	-0.78057465E-14
a ₆	-0.86547412E+03	-0.11978151E+04	-0.89008093E+04
a ₇	-0.17798424E+01	0.367033075+01	0.63964897E+01

Table 2.2 Constants used in Transport Equations

Species	T ₁₀ (K)	Viscosity		Thermal Conductivity		Molecular Diffusion		
		U ₁₀ X 10 ⁶ kg/(m.s)	S _i (K)	K ₁₀ W/(m.k)	S _i (K)	W gm/mol	σ _i (A)	T _{el} (K)
H ₂	273	8.41	69.67	0.16273	166.67	2.0159	2.827	59.7
Air	273	17.16	110.06	0.02415	194.44	28.996	3.711	78.6
O ₂	273	19.19	138.89	0.0246	222.22	31.999	3.407	106.7
N ₂	273	16.63	106.63	0.0242	166.67	28.013	3.798	78.6

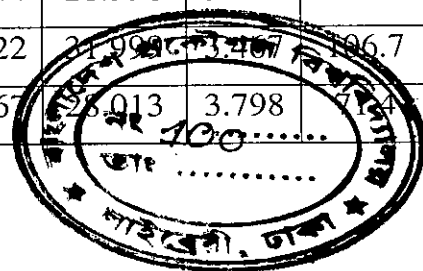


Table 3.1 Calculation Summaries

Base thickness (m)	Inlet width (m)	Merging angle (degree)	Identification of Computed results
0.01	0.015	10	Case-1
		20	Case-2
		30	Case-3
		40	Case-4
		50	Case-5
0.015	0.0125	10	Case-6
		20	Case-7
		40	Case-8

